

COMPARATIVE STUDY OF TRANSIENT AND QUASI-STEADY  
AEROELASTIC ANALYSIS OF COMPOSITE WIND TURBINE BLADE  
IN STEADY WIND CONDITIONS

A THESIS SUBMITTED TO  
THE GRADUATE SCHOOL OF NATURAL AND APPLIED SCIENCES  
OF  
MIDDLE EAST TECHNICAL UNIVERSITY

BY

HAKAN SARGIN

IN PARTIAL FULFILLMENT OF THE REQUIREMENTS  
FOR  
THE DEGREE OF MASTER OF SCIENCE  
IN  
AEROSPACE ENGINEERING

FEBRUARY 2014



Approval of the thesis:

**COMPARATIVE STUDY OF TRANSIENT AND QUASI-STEADY  
AEROELASTIC ANALYSIS OF COMPOSITE WIND TURBINE BLADE  
IN STEADY WIND CONDITIONS**

submitted by **HAKAN SARGIN** in partial fulfillment of the requirements for the degree of **Master of Science in Aerospace Engineering Department, Middle East Technical University** by,

Prof. Dr. Canan Özgen  
Dean, Graduate School of **Natural and Applied Sciences**

\_\_\_\_\_

Prof. Dr. Ozan Tekinalp  
Head of Department, **Aerospace Engineering**

\_\_\_\_\_

Prof. Dr. Altan Kayran  
Supervisor, **Aerospace Engineering Dept., METU**

\_\_\_\_\_

**Examining Committee Members:**

Prof. Dr. Yavuz Yaman  
Aerospace Engineering Dept., METU

\_\_\_\_\_

Prof. Dr. Altan Kayran  
Aerospace Engineering Dept., METU

\_\_\_\_\_

Assoc. Prof. Dr. Melin Şahin  
Aerospace Engineering Dept., METU

\_\_\_\_\_

Assoc. Prof. Dr. Nilay Sezer Uzol  
Aerospace Engineering Dept., METU

\_\_\_\_\_

Murat Günel, M.Sc.  
Turkish Aviation Industry, TAI

\_\_\_\_\_

**Date:** 07.02.2014

**I hereby declare that all information in this document has been obtained and presented in accordance with academic rules and ethical conduct. I also declare that, as required by these rules and conduct, I have fully cited and referenced all material and results that are not original to this work.**

Name, Last name: Hakan Sargin

Signature :

## **ABSTRACT**

### **COMPARATIVE STUDY OF TRANSIENT AND QUASI-STEADY AEROELASTIC ANALYSIS OF COMPOSITE WIND TURBINE BLADE IN STEADY WIND CONDITIONS**

**SARGIN, Hakan**

**M.S., Department of Aerospace Engineering**

**Supervisor: Prof. Dr. ALTAN KAYRAN**

**February 2014, 143 Pages**

The objective of this study is to conduct a comparative study of the transient and quasi-steady aeroelastic analysis of a composite wind turbine blade in steady wind conditions. Transient analysis of the wind turbine blade is performed by the multi-body dynamic code Samcef Wind Turbine which uses blade element momentum theory for aerodynamic load calculation. For this purpose, a multi-body wind turbine model is generated with rigid components except for the turbine blades. For the purposes of the study, a reference three dimensional blade is designed using inverse design methodology. Dynamic superelement of the turbine blades are created and introduced into multi-body model of the wind turbine system, and transient aeroelastic analysis of the multi-body wind turbine system is performed in steady wind conditions. As a follow-up study, quasi-steady aeroelastic analysis of the same composite wind turbine blade is performed by coupling a structural finite element solver with an aerodynamic tool based on blade element momentum theory. Quasi-

steady aeroelastic analysis of the blade is performed at different azimuthal positions of the blade and transient effects due to the rotation of the blade are ignored. The article aims at investigating the applicability of quasi-steady aeroelastic modeling of the turbine blade in steady wind conditions by comparing the deformations obtained by quasi-steady aeroelastic analysis and transient aeroelastic analysis of the complete turbine system at the same azimuthal positions of the blade. The presented results conclude that the quasi-steady aeroelastic analysis and transient aeroelastic analysis have a close match and the coupling between the finite element solver with a blade element momentum based aerodynamic tool can be used for static aeroelastic analysis at preliminary design state of a composite wind turbine blade.

Keywords: Aeroelasticity, Composite Wind Turbine Blade, Finite Element Analysis, Blade Element Momentum Theory, FEM-BEM Coupling.

## ÖZ

### KOMPOZİT RÜZGÂR TÜRBİN KANADININ SABİT RÜZGÂR KOŞULLARINDA ZAMANA BAĞLI VE NEREDEYSE STATİK AEROELASTİK ANALİZLERİNİN KARŞILAŞTIRMALI ÇALIŞMASI

SARGIN, Hakan

Yüksek Lisans Havacılık ve Uzay Mühendisliği Bölümü

Tez Yöneticisi: Prof. Dr. ALTAN KAYRAN

Şubat 2014, 143 Sayfa

Bu tezin konusu, kompozit rüzgâr türbin kanadının sabit rüzgâr koşullarında zamana bağlı ve neredeyse statik aeroelastik analizlerinin karşılaştırılmalı çalışılmasıdır. Rüzgâr kanadının zamana bağlı analizleri, aerodinamik analizler için pal elemanı momentum teorisini kullanan çok parçalı dinamik kodlu Samcef Wind Turbine kullanılarak yapılmıştır. Bu amaçla, türbin kanatları haricindeki bileşenler esnemez olacak şekilde çok parçalı rüzgâr türbin modeli yaratılmıştır. Rotor kanadı içinse, üç boyutlu referans kanat tersine tasarım metodu uygulanarak tasarlanmıştır. Dinamik supereleman türbin kanatları yaratılmış ve çok parçalı rüzgâr türbini modeline tanıtılmış ve sabit rüzgâr koşullarında çok parçalı rüzgâr türbininin zamana bağlı aeroelastik analizleri yapılmıştır. Bu çalışmanın devamı olarak, aynı kompozit rüzgâr türbini kanadının neredeyse statik analizleri, bir yapısal sonlu eleman çözücüsü ile pal elemanı momentum teorisi temelli aerodinamik bir araç eşleştirilerek yapılmıştır.

Neredeyse statik aeroelastik analizler, kanadın farklı ufuk açılarında ve dönüşten kaynaklanan etkiler yok sayılarak yapılmıştır. Çalışma, kanadın aynı ufuk açılarında neredeyse statik aeroelastik rüzgâr kanadı modelinin analizleri sonucunda elde edilen deformasyonlar ile bütün türbin sisteminin zamana bağlı aeroelastik analizleri sonucunda elde edilen deformasyonları karşılaştırarak uygulanabilirliğini araştırmayı amaçlamaktadır. Sunulan sonuçlar, neredeyse statik aeroelastik analizler ile zamana bağlı aeroelastik analizlerin yakın olarak eşleştiğini göstermektedir ve tasarım aşamasındaki kompozit rüzgâr türbinin statik aeroelastik analizleri için yapısal sonlu eleman çözücüsünün pal elemanı momentum teorisi temelli aerodinamik bir araç ile eşleşmesi kullanılabilir.

Anahtar Kelimeler: Aeroelastiklik, Kompozit Rüzgâr Türbin Kanadı, Sonlu Eleman Analizleri, Pal Elemanı Momentum Teorisi, SEA-PEM Eşleştirmesi.



*To My Family*

## **ACKNOWLEDGMENTS**

I would like to thank my supervisor Prof. Dr. Altan Kayran for his guidance, support, encouragement and patience throughout the study. The comments of the examining committee members are also greatly acknowledged.

I want to thank my colleagues Erdoğan Tolga İnsuyu, Levent Ünlüsoy and Evren Sakarya for their assistance and collaboration in the study.

I would also gratefully appreciate the support and assistance of all my cherished friends but especially Mehmet Ozan Gözcü for his assistance.

I would like to thank my parents for their guidance and insight and wife for their care and support.

## TABLE OF CONTENTS

ABSTRACT .....	v
ÖZ .....	vii
ACKNOWLEDGMENTS .....	x
TABLE OF CONTENTS .....	xi
LIST OF TABLES .....	xiii
LIST OF FIGURES .....	xv
LIST OF SYMBOLS .....	xix
LIST OF ABBREVIATIONS .....	xxi
CHAPTERS	
1.INTRODUCTION .....	1
1.1 Historical Review and Wind Energy .....	4
1.1.1 Windmills.....	5
1.1.2 European Horizontal Axis Windmills.....	7
1.1.3 Wind Turbines .....	9
1.2 General Description and Layout of a Wind Turbine .....	12
1.2.1 Vertical Axis Wind Turbines .....	13
1.2.2 Horizontal Axis Wind Turbines.....	15
1.2.3 Layout of a Horizontal Axis Wind Turbine.....	15
1.3 Literature Review.....	20
1.4 Scope of the Thesis .....	23
2.ROTOR AERODYNAMICS .....	25
2.1 The Actuator Disc Model (One-Dimensional Linear Momentum Theory). 25	
2.2 Rotor Disc Theory (Angular Momentum Theory).....	28
2.3 The Blade Element Momentum (BEM) Theory .....	31

3.INVERSE DESIGN OF THE REFERENCE BLADE AND QUASI-STEADY AEROELASTIC ANALYSIS OF THE WIND TURBINE BLADE .....	41
3.1 Selection of Composite Materials for the Blade .....	43
3.2 Variational Asymptotic Beam Section Analysis; PreVABS and VABS .....	46
3.3 VABS Modeling of the Wind Turbine Blade .....	53
3.4 Finite Element Modeling of the Wind Turbine Blade .....	56
3.4.1 Geometric Modeling .....	56
3.4.2 Mesh Generation and Property Assignment .....	58
3.4.3 Application of the Boundary Conditions and Modal Analysis .....	61
3.5 Quasi-steady Aeroelastic Analysis.....	64
3.5.1 Results of Quasi-steady Aeroelastic Analysis for Concentrated Load Cases .....	68
3.5.2 Results of Quasi-steady Aeroelastic Analysis for Distributed Load Cases .....	76
4.MULTI-BODY MODELING of the REFERENCE TURBINE AND TRANSIENT AEROELASTIC ANALYSIS OF THE BLADE.....	81
4.1 Generation of Superelement Blade .....	82
4.2 Wind Turbine Modeling in Samcef Wind Turbine .....	89
4.3 Results of the Transient Aeroelastic Analysis .....	95
5.CONCLUSION .....	103
REFERENCES.....	107
A.PREVABS INPUT FILES.....	115
B.WT_PERF INPUT FILE .....	127
C.AERODYNAMIC COEFFICIENTS of NREL BLADE .....	135
D.SAMCEF AERODYNAMIC VALIDATION .....	139

## LIST OF TABLES

### TABLES

Table 3.1 Chord and Twist Distributions of NREL Phase VI Blade [41].....	42
Table 3.2 Physical and Mechanical Properties of Prepreg Hybrid Carbon/Fiberglass Composite Triax, 70% 0° Unidirectional Type [27].....	45
Table 3.3 Physical and Mechanical Properties of E-Glass Harness Satin Weave Fabric 7781/EA93 [27] .....	46
Table 3.4 Sectional Beam Properties of UAE Phase VI Blades [41].....	53
Table 3.5 Sectional Beam Properties of the Inverse Designed Reference Blade.....	54
Table 3.6 Sectional Ply Numbers and Thickness Variation.....	56
Table 3.7 Number of Elements and Nodes Used in the Detailed Finite Element Model of the Inverse Design Blade.....	59
Table 3.8 Summary of Center of Gravity, Principal Inertias, Radii of Gyration, Mass and Volume of the Inverse Design Blade .....	60
Table 3.9 Global Mode Shapes and Natural Frequency Results of the Inverse Design Blade .....	64
Table 3.10 Results of Quasi-steady Aeroelastic Analysis for Concentrated Loads...	76
Table 3.11 Incremental Changes in Angle of Attack Values with the Iteration Numbers (Azimuthal Position - 90 Degree) .....	79
Table 3.12 Results of Quasi-steady Aeroelastic Analysis for Distributed Loads .....	79
Table 4.1 Comparison of the Natural Frequencies.....	87
Table 4.2 Tower Properties Used in the Multi-body Simulation of the Wind Turbine System.....	91
Table 4.3 Blade Properties Used in the Multi-body Simulation of the Wind Turbine System.....	92

Table 4.4 Samtech Controller & Fast Drive Train Properties in the Multi-body Simulation of the Wind Turbine System.....	92
Table 4.5 Constant Function Table defined in Multi-body Dynamic Model of the Wind Turbine System.....	94
Table 4.6 Rated Load Case defined in Multi-body Dynamic Model of the Wind Turbine System .....	95
Table 4.7 Axial and Tangential Tip Displacement Variations at Different Azimuthal Positions .....	100
Table 4.8 Comparison of the Tip Deflection Results.....	100
Table 4.9 Flapwise Bending Moments at $r=0.66$ m Calculated for the Constant Wind Speed (15 m/s).....	101

## LIST OF FIGURES

### FIGURES

Figure 1.1 The Worldwide Wind Capacity by the end of 2013 [4] .....	2
Figure 1.2 Total Installed Capacity for Market Leaders by the end of June 2013 [4].	2
Figure 1.3 Growth in Size of Commercial Wind Turbine Designs [7].....	3
Figure 1.4 The Earliest Evidence from Iconography of Around 2450 B.C. Shows Wind Powered Ship [24].....	4
Figure 1.5 A Diagram of Heron’s Organ, 1 <sup>st</sup> Century [11].....	5
Figure 1.6 Ancient Persian Vertical Axis Windmills [51].....	6
Figure 1.7 The Vertical-axis Chinese Windmill, With Eight Junk Sails [14].....	7
Figure 1.8 A Picture of Windmill from an English Prayer-book “ <i>Windmill Psalter</i> ” of 1270 [2] .....	8
Figure 1.9 Cog and Gear Design and Post Windmill [3] .....	8
Figure 1.10 In 1888 Charles F. Brush Invented the First Automatically Operated Horizontal Axis Wind Turbine [49].....	10
Figure 1.11 La Cour’s First Electricity Producing Wind Turbine in 1891, Askov, Denmark [1] .....	11
Figure 1.12 Modern Offshore Wind Turbine [32] .....	12
Figure 1.13 Wind Turbine Types [20] .....	13
Figure 1.14 Several Types of VAWTs [10].....	14
Figure 1.15 Typical Horizontal Axis Wind Turbine Blade [18].....	16
Figure 1.16 Rotating Pitch Mechanism Attached to the Hub [19].....	17
Figure 1.17 Hub Types [6] .....	18
Figure 1.18 Schematic View of HAWT Drive Train [12] .....	18
Figure 1.19 Yaw Drive Mechanism [19] .....	19
Figure 1.20 Complete Wind Turbine System with Tower and Foundation [6] .....	20

Figure 2.1 Discontinuous Pressure Drop across the Rotor [23].....	26
Figure 2.2 Airflow Rotates in the Opposite Direction behind the Downwind Turbine Rotor [24].....	28
Figure 2.3 Extended Momentum Theory, Taking into Consideration the Rotating Rotor Wake [19].....	29
Figure 2.4 Schematic of the Rotor Disk Theory [23].....	30
Figure 2.5 Local Blade Element Velocities and Aerodynamic forces [26] .....	32
Figure 2.6 Normal and Tangential Force Distribution over the Blade [19].....	34
Figure 2.7 Tip Loss Flow Diagram and Azithimuthal Variation at Various Radial Positions of the Blade [23, 30] .....	37
Figure 3.1 Geometric Presentation of the Wing Studied [15].....	42
Figure 3.2 Chord and Twist Distribution of the NREL Blade .....	43
Figure 3.3 Structure, Spar Location and Materials used in the Different Parts of the Blade [27].....	45
Figure 3.4 Schematic Representation of an Airfoil Profile in PreVABS [15] .....	47
Figure 3.5 Segmented Blade Cross-Section Definitions for PreVABS [15].....	48
Figure 3.6 PreVABS Modeling of NREL Blade Section. (a) Dimensionalized Cross-section Profile of the NREL Inverse Design Blade (b) High Resolution Finite Element Mesh on the Cross-section of the Blade (c) Zoomed View of the Spar-Skin Connection (d) Zoomed View High Resolution Finite Element Mesh at the Trailing Edge.....	49
Figure 3.7 VABS - PreVABS Coupling Flow Chart and Decomposition of a Three-Dimensional Blade into Two-Dimensional Cross-section and a One-Dimensional Beam [25].....	50
Figure 3.8 Comparison of the Variation of the Flapwise Bending Stiffness of the NREL Blade and the Inverse Design Blade .....	55
Figure 3.9 Isometric View of the Skin Surfaces at the Root and the Transition Part of the Blade.....	57
Figure 3.10 Cross-Sectional View of the Finite Element Mesh of the Front and Rear Part of the Skin of the Blade .....	57
Figure 3.11 Isometric View of the Spar Location of the Blade .....	58



Figure 3.12 Finite Element Mesh of the NREL Blade.....	59
Figure 3.13 Fiber Orientation and Material Assignment .....	60
Figure 3.14 Zoomed View of Fixed Root Nodes in MSC®/PATRAN .....	61
Figure 3.15 1 <sup>st</sup> Flapwise Bending Mode Shape of the Inverse Design Blade.....	62
Figure 3.16 1 <sup>st</sup> Edgewise Bending Mode Shape of Inverse Design Blade.....	62
Figure 3.17 2 <sup>nd</sup> Flapwise Bending Mode Shape of the Inverse Design Blade.....	63
Figure 3.18 Torsional Mode Shape of the Inverse Design Blade [24.52 Hz].....	63
Figure 3.19 Flow Chart of the Coupling Procedure [43] .....	65
Figure 3.20 Lift Force Coefficient Data of the NREL S809 Airfoil [41] .....	66
Figure 3.21 Drag Force Coefficient Data of NREL S809 Airfoil [41] .....	67
Figure 3.22 NREL S809 Airfoil – Extrapolated Aerodynamic Force Coefficients...	68
Figure 3.23 Azimuth Positions of the NREL Blade.....	69
Figure 3.24 Axial and Tangential Induction Factor Variations of NREL S809 .....	70
Figure 3.25 In-flow Angle and Angle of Attack Variations of the NREL S809 Blade - Azimuth 0.....	71
Figure 3.26 Normal and Tangential Force Variations of NREL S809 Airfoil – Azimuth 0.....	71
Figure 3.27 Location of Aerodynamic Force Application Nodes and Loads Applied to the Inverse Design Blade for Flapwise Deflection Calculation.....	72
Figure 3.28 Blade Deflection at 72 rpm and 15m/s Wind Speed – After the 1 <sup>st</sup> Iteration .....	73
Figure 3.29 Deformed Blade and Shifted Node Locations .....	74
Figure 3.30 Blade Deflection at 72 rpm and 15m/s Wind Speed – After the 2 <sup>nd</sup> Iteration .....	74
Figure 3.31 Blade Deflection at 72 rpm and 15m/s Wind Speed – After the 3 <sup>rd</sup> Iteration .....	75
Figure 3.32 RBE3 Elements and Distribution of the Aerodynamic Loads Applied at the Aerodynamic Center to Upper Section Nodes .....	77
Figure 3.33 Flapwise Deflection at 72 rpm and 15m/s Wind Speed – After the 1 <sup>st</sup> Iteration .....	78
Figure 4.1 Isometric View of the Blade Geometry in Samcef Field.....	84

Figure 4.2 Generation of the Retained Nodes and Mean Elements .....	85
Figure 4.3 Isometric View of the Meshed Blade .....	86
Figure 4.4 1st Flapwise Bending Mode Shape of the Superelement Blade Model [4.13 Hz].....	88
Figure 4.5 1st Edgewise Bending Mode Shape of the Superelement Blade Model...	88
Figure 4.6 2nd Flapwise Bending Mode Shape of the Superelement Blade Model [17.52 Hz].....	89
Figure 4.7 Torsional Mode Shape of the Superelement Blade Model [28.40 Hz].....	89
Figure 4.8 Multi-body Model of the Wind Turbine Parts [55] .....	90
Figure 4.9 Multi-body Dynamic Model of the Wind Turbine System.....	93
Figure 4.10 Assignment of the Aerodynamic Coefficients to Multi-body Dynamic Model of the Wind Turbine System.....	93
Figure 4.11 Assignment of the Constant Function to Control Node.....	94
Figure 4.12 Advanced Aero Options for Transient Analysis.....	95
Figure 4.13 Normal Force Variation across the Blade for Different Azimuthal Positions .....	96
Figure 4.14 Tangential Force Variation across the Blade for Different Azimuthal Positions .....	97
Figure 4.15 Moment Variation across the Blade for Different Azimuthal Positions.	97
Figure 4.16 Axial Tip Displacement of the Blade towards Downwind .....	98
Figure 4.17 Tangential Tip Displacement of the Blade towards Next Blade .....	98
Figure A.1 Schematic of VABS Coordinates System.....	115
Figure B.1 WT_Perf Output File.....	130
Figure D.1 Aerodynamic Input File Sample for SWT.....	139
Figure D.2 Assignment of the Aerodynamic Coefficients to Multi-body Dynamic Model.....	141
Figure D.3 Imposition of Rotor Speed Boundary Condition in SWT .....	141
Figure D.4 Imposition of Pitch Angle Boundary Condition in SWT .....	142
Figure D.5 Initial Static Computation Option.....	143

## LIST OF SYMBOLS

$\alpha$	Angle of Attack
$\varphi$	Angle of Relative Wind
$a'$	Angular Induction Factor
$\Omega$	Angular Velocity of the Rotor
$a$	Axial Induction Factor
$c$	Chord Length
$F$	Combined tip-loss and hub-loss coefficient
$\rho$	Density of Air
$dT$	Differential Thrust
$dQ$	Differential Torque
$C_D$	Drag Coefficient
$D$	Drag Force
$C_L$	Lift Coefficient
$L$	Lift Force
$\omega$	Local Angular Velocity of the Flow
$\lambda_r$	Local Tip Speed Ratio
$\mu_{m2\&3}$	Mass Center of the Cross-section
$\dot{M}$	Mass Flow Rate
$i_{22}, i_{23}, i_{33}$	Mass Moment of Inertia
$\mu$	Mass per Unit Span
$C_M$	Moment Coefficient
$F_N$	Normal Force
$N$	Number of Blades
$Cent_x$	Pitch Axis Location of the Section in X Coordinate Frame
$Cent_y$	Pitch Axis Location of the Section in Y Coordinate Frame

$M$	Pitching Moment
$\nu$	Poisson's Ratio
$X_{web}$	Position for Web Centers in X Coordinate Frame
$Y_{web}$	Position for Web Centers in Y Coordinate Frame
$P$	Power
$C_P$	Power Coefficient
$F_{Tip}$	Prandtl's Tip-loss Correction
$F_{Root}$	Prandtl's Hub-loss Correction
$R$	Radius
$U_{rel}$	Relative Wind Velocity
$Re$	Reynolds Number
$A$	Rotor Area
$Q$	Rotor Torque
$G_{xy}$	Shear Modulus of Elasticity
$S$	Stiffness Matrix
$\sigma'$	Solidity
$\theta_P$	Section Pitch Angle
$\theta_T$	Section Twist Angle
$F_T$	Tangential Force
$C_T$	Thrust Coefficient
$T$	Thrust Force
$U$	Wind Velocity
$E_{X,Y,Z}$	Young's Modulus
$\Gamma$	3-D strain field

## LIST OF ABBREVIATIONS

0-D	Dimensionless
1-D	One Dimensional
2-D	Two Dimensional
3-D	Three Dimensional
BEM	Blade Element Momentum
CAD	Computer Aided Design
CFD	Computational Fluid Dynamics
DOFs	Degree of Freedoms
DTU	Delft University of Technology
EGWF	E-Glass Woven Fabric
FE	Finite Element
FEM	Finite Element Method
GRFP	Glass-Fiber Reinforced Plastic
HAWT	Horizontal Axis Wind Turbine
HPS	High Pressure Surface
LE	Leading Edge
LPS	Low Pressure Surface
MBD	Multi-body Dynamics
MPC	Multi-point Constraints
NREL	National Renewable Energy Laboratory
OSU	Ohio State University
RBE	Rigid Body Element
SWT	Samcef for Wind Turbine
TE	Trailing Edge
UDCF	Uni-directional Carbon Fiber

VAM Variational Asymptotic Methods

VAWT Vertical Axis Wind Turbine

## **CHAPTER 1**

### **INTRODUCTION**

The industrial revolution and the increase of the population of the World have triggered the energy need. The energy consumption in the World has been increasing rapidly and consecutively energy demand has increased significantly. Generally, fossil fuels have been used to provide the required energy demand. However, the depletion of the non-renewable resources and the increasing energy demand of the world together forced engineers to search for alternative energy resources such as wind energy. Unlike the stored energy resources such as fossil fuels, coal and natural gas, renewable energy sources are not depletable. Moreover, renewable energy sources such as radiation, wind, hydro, solar and thermal offer many benefits. Unlike the fossil fuel that emits gases that are harmful to environment, renewable energy resources are clean and do not generate atmospheric contaminants. Renewable sources might also cost effective depending on the application. When many considerations are taken account, renewable energy sources became more and more popular as the alternative energy resource.

Among the renewable energy sources, wind energy is one of the prime resource and possible candidate to replace the non-renewable energy resources in the future. It should be noted that power that exists in the wind can be converted into a useful energy by the wind turbine technology. Cost effective electrical energy, without the greenhouse effect, can be generated with the wind energy unlike the conventional energy resources of today which are primarily fossil fuel origin. Furthermore, wind turbine installation and electricity production costs are lower than or at the worst

case, close to the other non-renewable sources [20]. All the positive factors of the wind energy caused rapid development of wind energy technology, and the amount of wind energy produced has increased exponentially as can be seen in Figure 1.1 and Figure 1.2. Currently, wind energy shares a significant percentage among the other clean resources.

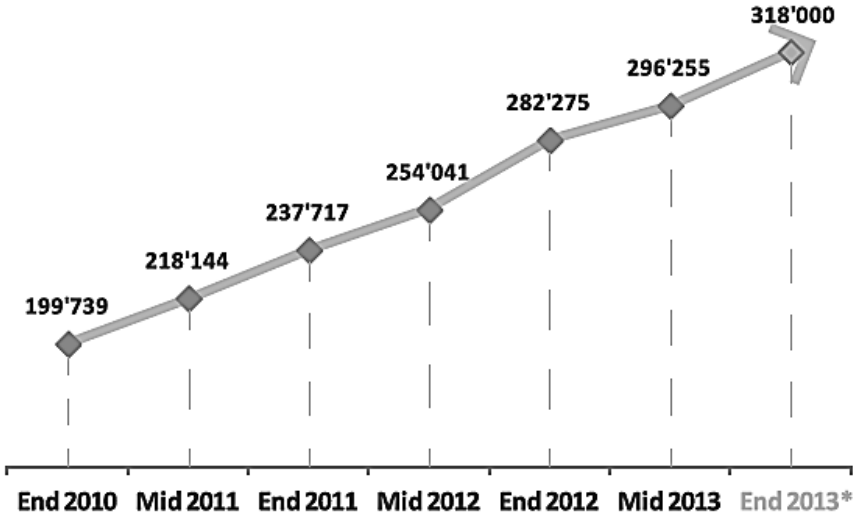


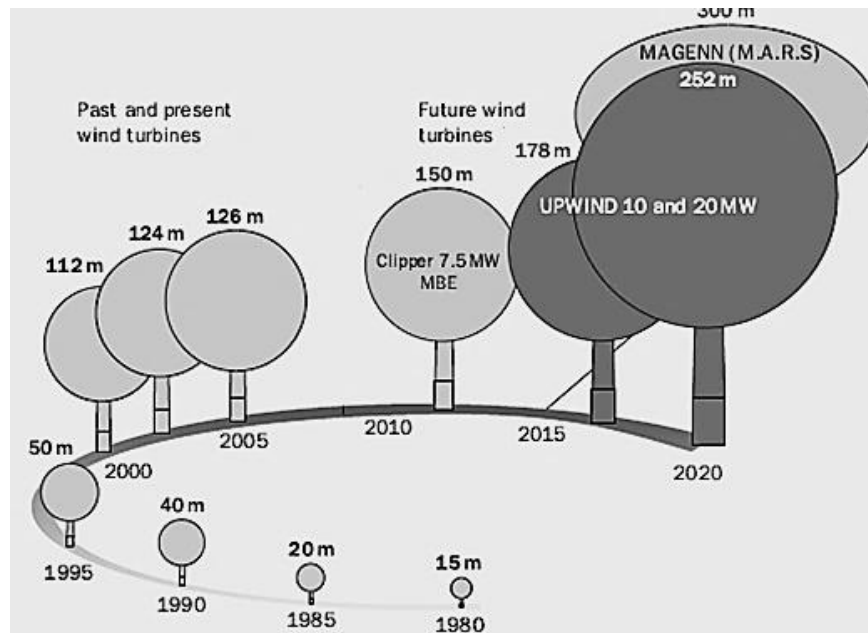
Figure 1.1 The Worldwide Wind Capacity by the end of 2013 [4]

Position	Country	Total Capacity by June 2013 [MW]	Added Capacity first half 2013 [MW]	Total Capacity end 2012 [MW]	Added Capacity first half 2012 [MW]	Total Capacity end 2011 [MW]	Added Capacity first half 2011 [MW]	Total Capacity end 2010 [MW]
1	China	80'824	5'500	75'324	5'410	62'364	8'000	44'733
2	USA	60'009	1,6	60'007	2'883	46'919	2'252	40'180
3	Germany	32'422	1'143	31'308	941	29'075	766	27'215
4	Spain	22'907	122	22'785	414	21'673	480	20'676
5	India	19'564	1'243	18'321	1'471	15'880	1'480	13'065
6	United Kingdom	9'610	1'331	8'228	822	6'018	504	5'203
7	Italy	8'415	273	8'152	320	6'877	460	5'797
8	France	7'821	198	7'623	650	6'640	400	5'660
9	Canada	6'578	377	6'201	246	5'265	603	4'008
10	Denmark	4'578	416	4'162	56	3'927	-	3'734
11	Portugal	4'564	22	4'542	19	4'379	260	3'702
12	Sweden	4'066	526	3'743	-	2'798	-	2'052
13	Australia	3'059	475	2'584	-	2'226	-	1'880
14	Brazil	2'788	281	2'507	118	1'429	-	930
15	Japan	2'655	41	2'614	-	2'501	-	2'304
	Rest of the World	26'204	2'030	24'174	3'026*	18'778	3'200*	15'805
	Total	296'255	13'980	282'275	16'376	237'717	18'405	199'739

Figure 1.2 Total Installed Capacity for Market Leaders by the end of June 2013 [4]



As mentioned earlier, wind turbine technology is rapidly evolving technological area and although significant developments have taken place over the last 30 years, wind turbine technology still has to be improved further to meet the challenges of the next generation wind turbine systems. To enhance the energy capture and reduce the cost of the generated electricity, wind turbines have been getting larger and larger [21]. In the 1980s, an average wind turbine had approximately 10-15 m diameter and produced almost 50 kW while the current wind turbines have 150 m rotor diameter and have an energy extraction capacity of almost 7-8 MW [22]. Figure 1.3 shows the growth in size of commercial wind turbine designs.



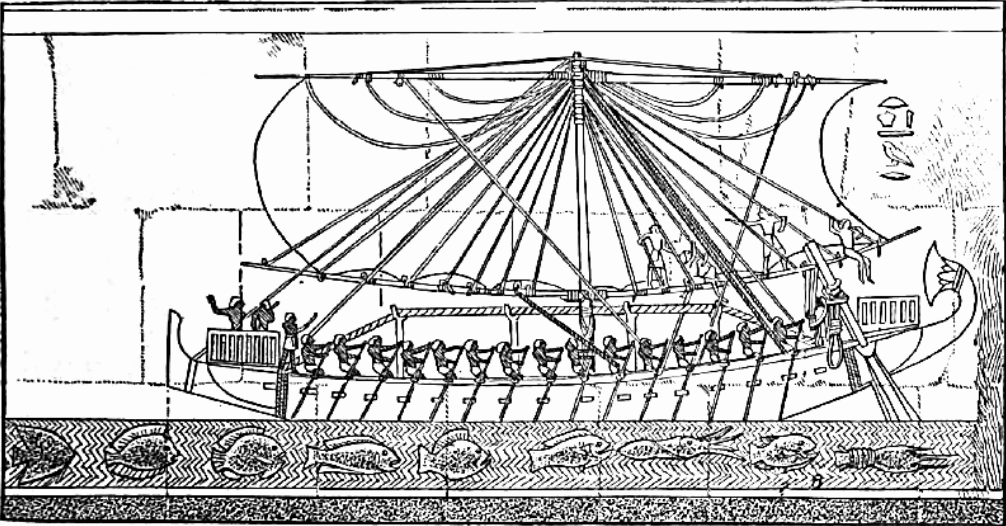
**Figure 1.3** Growth in Size of Commercial Wind Turbine Designs [7]

However, building very large machines introduce new problems in the practical design and cause stability issues which should be overcome to obtain reliable designs. For this purpose, geometric nonlinearities and aeroelastic instability issues need to be accurately accounted for in the design process of the wind turbine system. Aeroelastic effects can significantly change the aerodynamic load distribution especially in long turbine blades which are more flexible compared to small turbine

blades. For accurate estimation of the loads acting on the turbine blade, flexibility of the blade has to be taken into consideration in the design process. Today, aeroelasticity has become a key issue in the development process of long-lasting, flexible, large wind turbines. To achieve this goal, it is important to investigate aeroelastic effects in wind turbines and use reliable aeroelastic tools in the design process to avoid the failure, and estimate the loads accurately.

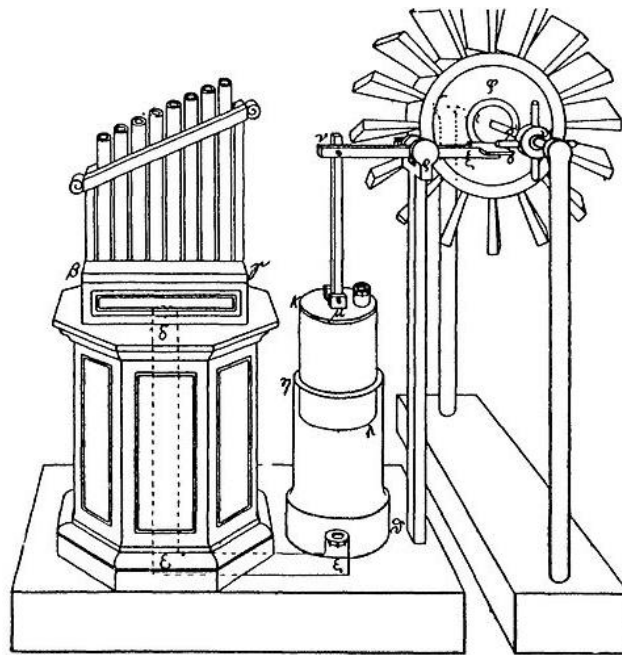
### 1.1 Historical Review and Wind Energy

Harnessing the energy from the wind power is not a new concept. Through the ages, wind energy has been used for different purposes and the first example of wind power usage in history was started with the sail boats. Approximately at 4000 B.C., the ancient Chinese and Egyptians were recorded as the first who had learned to use the wind power at their primitive rafts. They attached cotton-made sails to the long narrow boards to use the power of wind for powered transportation [5]. Figure 1.4 shows an example of the wind powered ship from the earliest evidence of iconography of around 2450 B.C. [24].



**Figure 1.4** The Earliest Evidence from Iconography of Around 2450 B.C. Shows Wind Powered Ship [24]

The first written evidence for converting the wind energy into useful mechanical power was found in ancient Greece. Heron of Alexandria (Heron Alexandrinus (10-85 A.D.)) is one of the greatest mathematician and engineer of the ancient world and best known as the first person who used wind power in his inventions [45]. He invented the Heron's organ which was creating sounds "like the sound of flute". This machine had a wind wheel which was connected to a piston. As the wind wheel turned in the wind, the piston started to raise and descend. With this movement, the compressed air in the pistons went out from cylindrical tubes and this was creating the sound as illustrated in Figure 1.5. This device is believed to be the first example of wind powering machine.



**Figure 1.5** A Diagram of Heron's Organ, 1<sup>st</sup> Century [11]

### 1.1.1 Windmills

Another ancient use for wind energy was in the form of windmills. According to verbal records which are not reliable as written sources, wind power for mechanical

use started with Babylonian emperor Hammurabi who used windmills for irrigation in 1700 B.C. [9]. However, for most of the historians, the earliest vertical axis windmill was designed for agricultural activities, such as water pumping and grain grinding, around 500-900 A.D. in Sistan at ancient Persia [12]. Figure 1.6 shows the ancient Persian vertical axis windmill used for grain grinding.

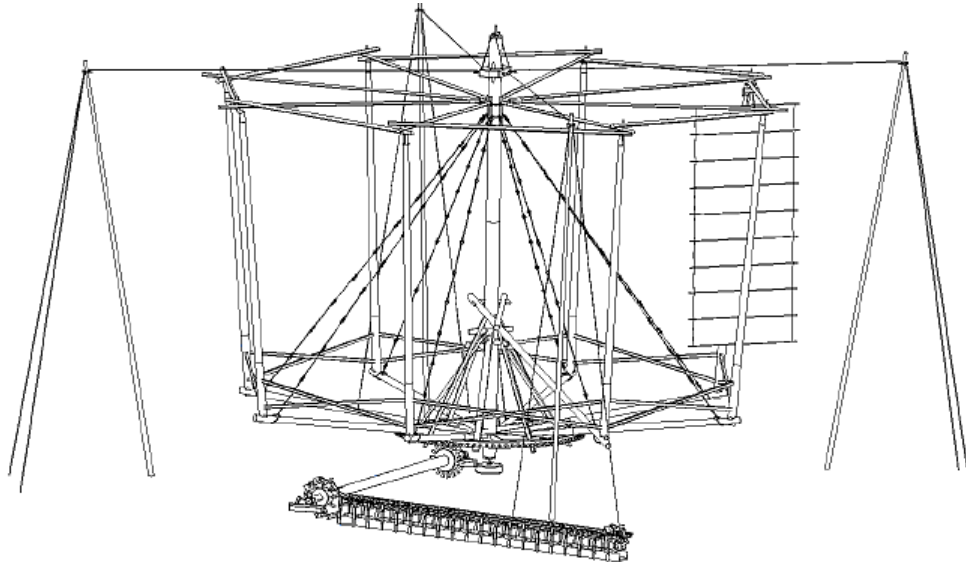


**Figure 1.6** Ancient Persian Vertical Axis Windmills [51]

The first Persian windmills were composed of two main parts. First component was vertical shaft fitted with sails or rectangle shape blades in order to catch the wind. Second one was the grinding stone which was directly driven by the wind-wheel. The windmills were structurally built to increase the wind velocity entering the windmill field. The apertures at the front face were placed narrower than the rear side and the directions of the apertures were oriented by the north-south direction of the 120 day winds [33]. As a consequence, these windmills were wind direction dependent devices.

Like in Persia, China is one of the pioneers for windmill usage. The mural paintings at “*Sandaohao*” [23] have shown the images that evidencing the use of vertical axis

windmills in China for at least approximately 1800 years. Unlike the Persian mills, Chinese wind driven devices were wind direction independent like modern vertical axis wind turbines. An example of the vertical-axis Chinese Windmill with eight junk sails is given in Figure 1.7.



**Figure 1.7** The Vertical-axis Chinese Windmill, With Eight Junk Sails [14]

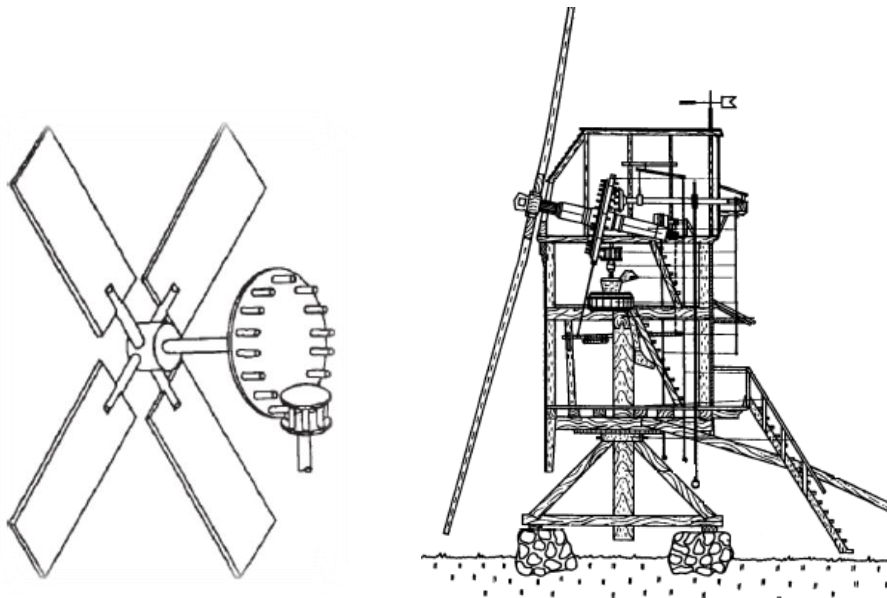
### **1.1.2 European Horizontal Axis Windmills**

Europeans started to use windmills later than Persians and Chinese. However, apart from the Eastern civilizations, they tried to convert the power of wind to mechanical energy by horizontal axis windmills. There are lots of speculations about the invention of horizontal axis windmills, but according to historians, at the end of 12<sup>th</sup> century, the horizontal axis windmills were invented and started to be used in Northwestern Europe [10]. In Figure 1.8, a picture of windmill from 13<sup>th</sup> century is shown.



**Figure 1.8** A Picture of Windmill from an English Prayer-book “*Windmill Psalter*” of 1270 [2]

Early designs were adopted from water wheel and were named as “*Post Windmills*”. These wind devices had four blades which were set at an angle and were mounted directly on a horizontal shaft. When the blades started to run, cog and ring gears provided the power transmission from horizontal shaft to vertical shaft to turn a grindstone. An early structural and mechanical design of a Post Windmill is illustrated in Figure 1.9.

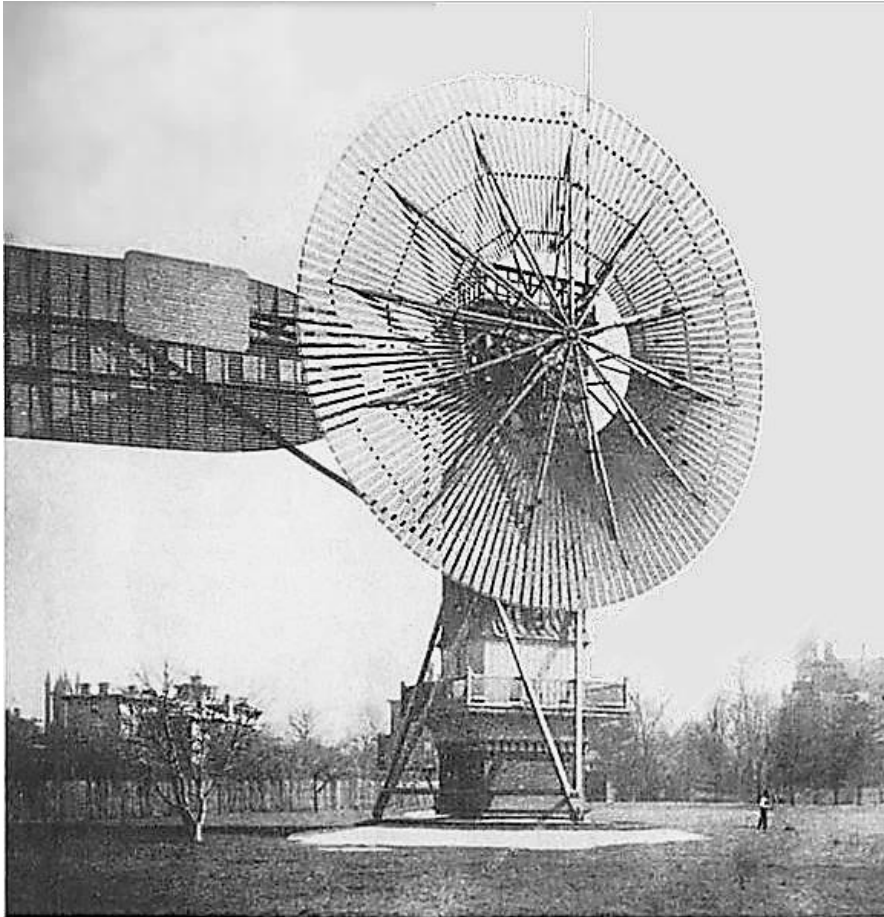


**Figure 1.9** Cog and Gear Design and Post Windmill [3]

Since the invention of Post Windmill, the design techniques are improved and many types of windmills had been developed and have been used all over the Europe. Smock mill, Dutch mill (Tower mill), and Fan mill are some examples that are still being used.

### **1.1.3 Wind Turbines**

With the changing demands and improvements on the technology, windmills were evolved to wind turbines in time. In contrast to a windmill, which is a machine that converts the wind power into mechanical power for water pumping and grain grinding, a wind turbine converts the wind energy to electrical energy [6]. The first wind turbine was invented by Professor James Blyth of Anderson's College, Glasgow in 1887. Blyth had constructed a 10-meter-high; cloth-sailed wind turbine to light his home, and this was accepted as the first successful attempt in electricity generation through wind power. In the winter of 1888, another pioneer Charles Brush built his own design. The horizontal axis wind turbine of Brush had a rotor diameter of 17 m and 144 wooden blades. This first model had capability to generate 12kW power despite the huge size. It was used to charge the batteries to supply the electric motors. It was not just the one of the first wind turbine but it also had a completely automatic control requiring no human operator. High step-up ratio windmill transmission (50:1) was also first used in Brush's windmill [8]. Figure 1.10 shows the first automatically operated horizontal axis wind turbine built by Brush.



**Figure 1.10** In 1888 Charles F. Brush Invented the First Automatically Operated Horizontal Axis Wind Turbine [49]

With the electricity generation from wind power, a completely new era has begun for the application of wind energy extraction, and the research work on the wind turbine technology has increased significantly. Dane Poul La Cour, professor at the Askov School in Denmark, came up with some empirical relations, and he discovered that wind turbine, with high solidity and low tip speed ratio, was not suitable for electricity generation [12]. According to the results from his research, Poul La Cour built four bladed, fast running wind turbine “*Kratostaten*” with DC generator in 1891. Poul La Cour used the generated electricity directly from wind turbine to produce hydrogen and oxygen for electrolysis. La Cour’s *Kratostaten* turbine is shown in Figure 1.11.





**Figure 1.11** La Cour's First Electricity Producing Wind Turbine in 1891, Askov, Denmark [1]

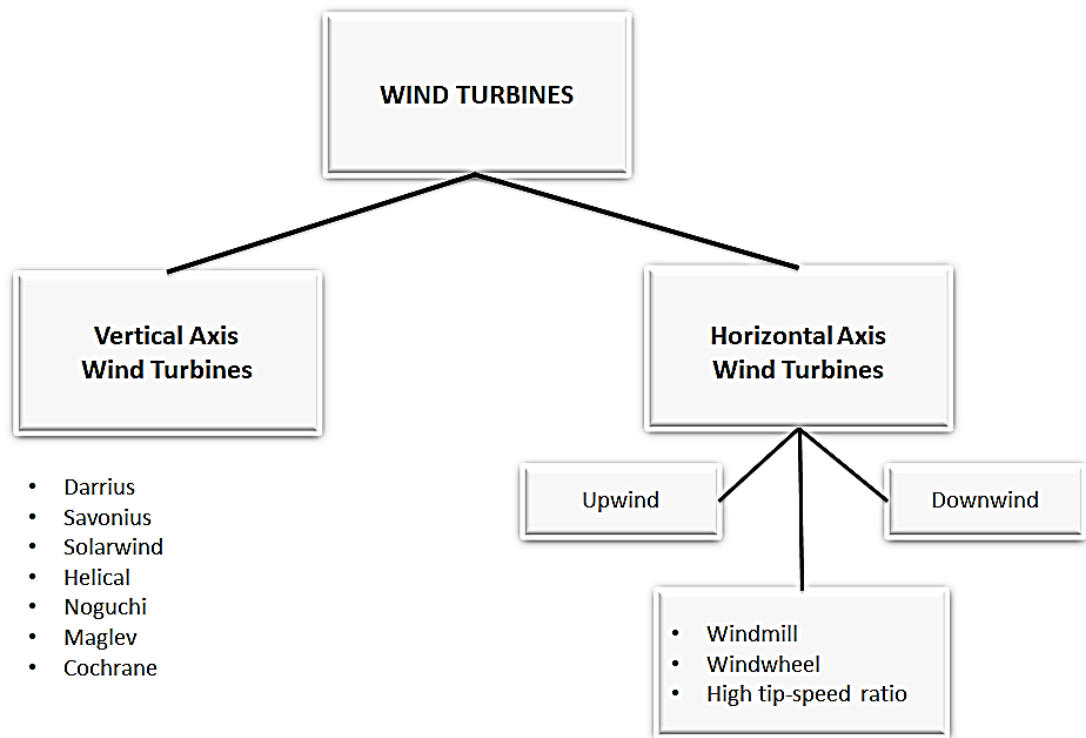
La Cour's low solidity and fast tip ratio concept was accepted and hundreds of wind turbine systems were built based on his concept. His idea led to modern horizontal axis wind turbines. With the beginning of the 20<sup>th</sup> century, researches have been accelerated and lots of progress has been made on the wind turbine aerodynamics and airfoil designs. Wind turbine designs made a great leap forward, and they are started to be used all over the world. Figure 1.12 shows a modern offshore wind turbine farm which is a typical system used for efficient electricity generation [32]. With the advent in the wind turbine technology, the number of efficient wind farms increased.



**Figure 1.12** Modern Offshore Wind Turbine [32]

## **1.2 General Description and Layout of a Wind Turbine**

Simplified working principle of a wind turbine is based on the fact that the blowing wind applies aerodynamic forces on the turbine blades and this provides the blade rotation. The rotation axis could be either horizontal or vertical with respect to ground, and rotation axis mainly categorizes the wind turbines as “*Horizontal Axis Wind Turbines (HAWTs)*” and “*Vertical Axis Wind Turbines (VAWTs)*”. Figure 1.13 investigates the wind turbine types by means of rotation axis [20].



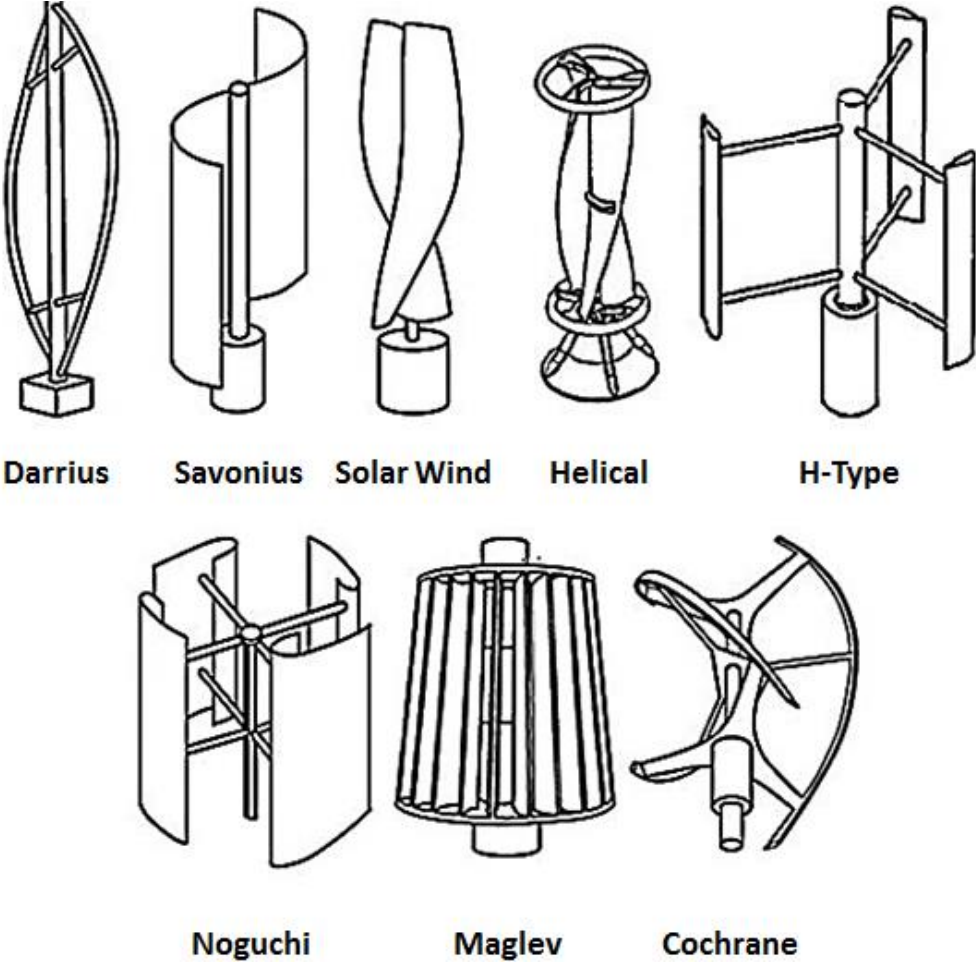
**Figure 1.13** Wind Turbine Types [20]

### 1.2.1 Vertical Axis Wind Turbines

Vertical axis wind turbines are the oldest known wind power converters which are settled vertically on the ground. There are various types of VAWTs in the market and these have been categorized as drag-driven or lift-driven rotors, and the most widely known ones are “*Darrius*”, “*Savonius*” and “*Giromill*”. Savonius type rotors principally use aerodynamic drag to capture the energy and this is why it is called as drag driven. In contrast to Savonius, Darrius and Giromill types of VAWTs are the lift driven devices and they use aerodynamic lift to extract the energy from wind.

VAWTs offer many advantages, such as they are omni-directional machines therefore accept wind from any direction and they do not need any yawing mechanism to turn into the wind. Moreover, vertical axis wind turbines can operate at high rotational speeds which offer reduction in gear ratios. Another advantage is that, VAWTs do not require tower since they can be mounted on the ground. Ground

mounting also provides an easier access for maintenance. In Figure 1.14, different types of VAWTs are illustrated.



**Figure 1.14** Several Types of VAWTs [10]

Despite all these advantages, horizontal axis wind turbines (HAWTs) are more popular than the Vertical Axis Wind Turbines due to better efficiency ratios. In the vertical axis machines, the blade facing the wind works well, but other blades effectively pull in the reverse direction causing a decrease in efficiency. Another disadvantage of the VAWTs is dynamic stability problems which lead to high stress on blades and blades become prone to fatigue. Furthermore, low starting torque issue has to be considered for the VAWTs. Most of the VAWTs need starters for the initial

movement. Because of the reasons explained, vertical axis turbines are less preferred compared to the horizontal axis wind turbines.

### **1.2.2 Horizontal Axis Wind Turbines**

All HAWTs generate the electricity from aerodynamic lift and therefore, they are described as “*Lift-driven*” or “*Propeller-type*” wind turbines. Based on the configuration of rotor with respect to the wind, HAWTs can be categorized as “*Upwind*” and “*Downwind*”. Briefly, the main difference between these two is the position of the blades with respect to the nacelle. For the upwind turbine, blades are positioned in front of the nacelle similar to propellers and this is the most widely used type of turbine. On the other hand, the downwind turbine rotor is on the back side of the nacelle and they work at higher wind speeds.

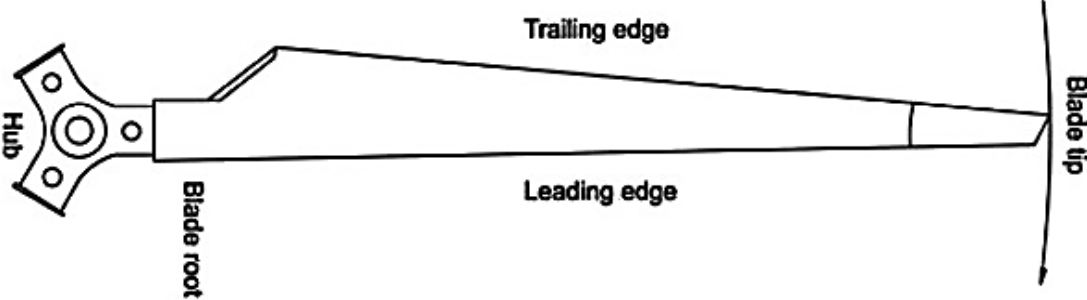
Upwind and downwind turbines have distinctive advantages and disadvantages. For instance, in downwind turbines more flexible rotors can be used because blade-tower strike is not an issue. Moreover, with this configuration centrifugal moments are balanced by moments due to thrust and causes a reduction at blade root bending moments [10]. However, tower and nacelle creates distorted unstable wakes and these wakes result in ripples in the generated power. Additionally, wakes may result in aerodynamic losses and introduce more fatigue load on the blades causing structural failures. For the upwind type of wind machines, the main advantage is that the unstable wake effect is less than the downwind type and dynamic load distribution is more balanced.

### **1.2.3 Layout of a Horizontal Axis Wind Turbine**

A typical horizontal axis wind turbine has the following major components;

- Rotor Blades, Pitch Mechanism and Supporting Hub.
- Nacelle, Drive Train and Yaw Drive.
- Tower and Foundation.

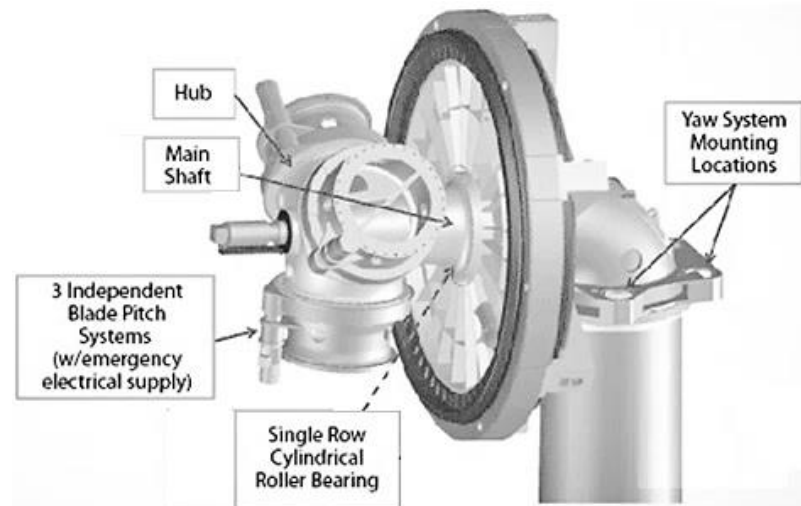
**Blades:** Most of the modern rotor systems of the wind turbines consist of 3 high-technology blades which are made of composite materials such as reinforced polyester or epoxy. Typical fiber reinforcement is fiberglass, and for very long blades, carbon fibers are also used in the blade structure to provide additional stiffness with much less weight penalty compared to fiberglass. Principally, wind turbine blades are similar to the aircraft wings in terms of aerodynamic lift generation. Figure 1.15 shows a typical horizontal axis wind turbine blade. When the air moves over the wing profile, low pressure is created on the suction side and this creates the lift perpendicular to the wind direction [18]. Compared to the aircraft wings, turbine blades are optimized for extracting the energy from wind with high efficiency; therefore they are thinner, longer and generally twisted along the longitudinal axis in order to achieve the constant angle of attack which produces the maximum lift coefficient.



**Figure 1.15** Typical Horizontal Axis Wind Turbine Blade [18]

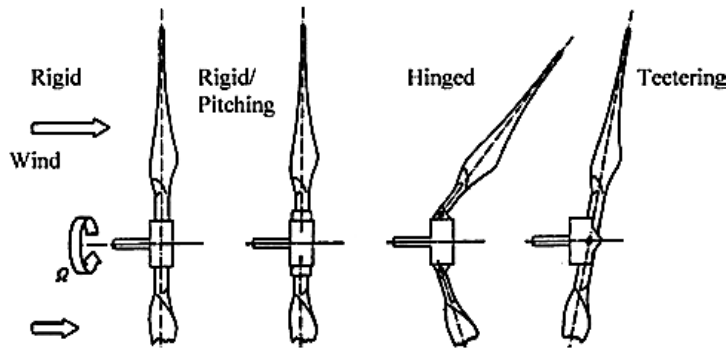
**Pitch Mechanism:** For the modern mid and large scale wind turbines, aerodynamic power production and speed are generally controlled by aerodynamic control units. One of the most popular control methods is changing the “*Pitch Angle*” of the blades. The variable pitch wind turbines have pitch mechanisms that change the pitch angle of each blade with respect to the plane of rotation to provide the control during the starting and stopping of the wind turbine, and for maximizing the energy capture

as much as possible at varying wind speeds. The pitch mechanism works as aerodynamic brake by pitching to stall and adjusts the power output at wind speeds higher than the rated wind speed. Figure 1.16 shows a rotating pitch mechanism attached to the hub of a horizontal axis wind turbine.



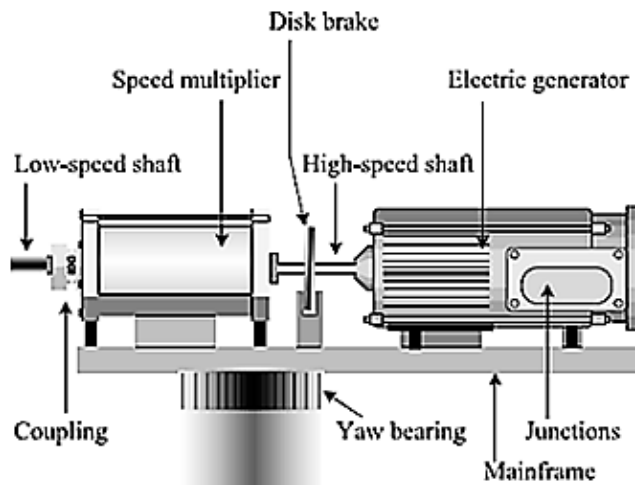
**Figure 1.16** Rotating Pitch Mechanism Attached to the Hub [19]

**Hub:** The blades and the pitch mechanism are connected with the hub structurally. The rotor hub is the connection part of the rotor to the drive train and all loads are concentrated on the hub. Therefore, hub is the most highly stressed component of a wind turbine and generally made of steel to be stiff enough to withstand the loads, rotor weight and absorb the vibrations [12]. The hub component can be categorized as; rigid, teetering, or hinged. Generally, rigid hubs are employed by the upwind turbines, and teetering hubs are used in two bladed downwind turbines. For the rigid hub, flapping (flapwise) and lead–lag (in-plane) moments are directly transmitted to the hub. In a teetered rotor, no flapping moments are transmitted to the hub and teetering motion balances the asymmetrical aerodynamic loads so does reduce the bending stresses in the blades [38]. Figure 1.17 shows the common hub types used.



**Figure 1.17** Hub Types [6]

**Nacelle:** Nacelle which is mounted on the top of the tower contains all drive train components such as low-speed shaft, gear box, high-speed shaft, generator, brake system and yaw system. Nacelle is composed of two main parts; “*Nacelle Housing*” and “*Bedplate*”. Nacelle housing works as a protective coverage for internal equipment and generally made of GRFP. Nacelle bedplate provides a stiff floor for the power systems and directly mounted to the tower structure. The main purpose of the bedplate is transferring the rotor bending moments into the tower structure.



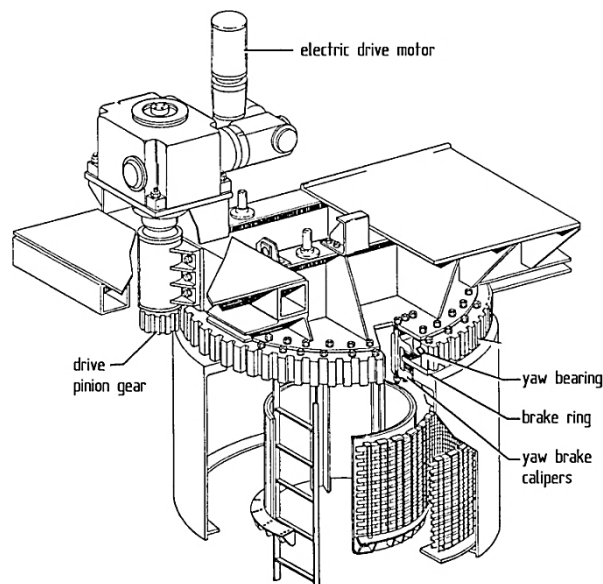
**Figure 1.18** Schematic View of HAWT Drive Train [12]

**Drive Train:** The heart of the wind turbine is its drive train and power conversion systems. First part of the drive train system is low-speed shaft which is directly



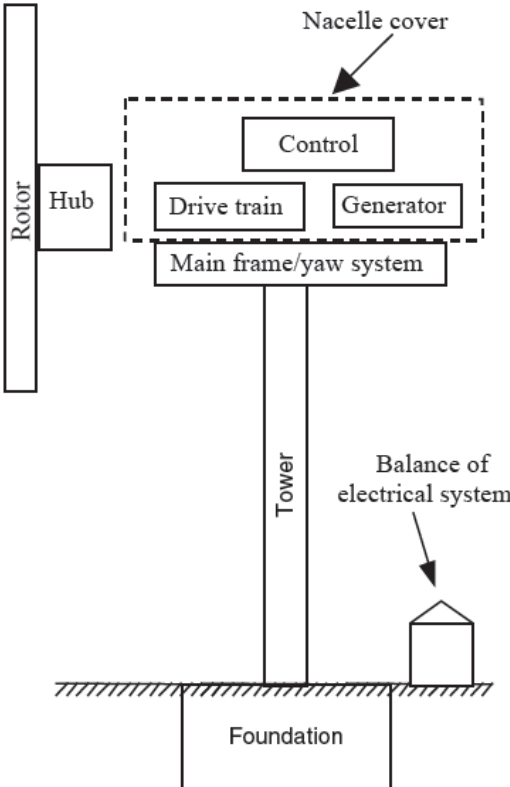
driven by rotor system. The low-speed shaft transmits the rotational motion directly to the gearbox or to the variable speed generator in direct rotor driven wind turbines. For the traditional designs, gearbox steps up the speed of revolutions to a desired high value and this increased value is transmitted to the generator via the high-speed shaft. And finally, this rotational kinetic energy is converted into electrical energy via generator. Figure 1.18 shows the schematic view of a typical HAWT drive train [12].

**Yaw Drive:** Another important drive train component is yaw mechanism. There are two types of yaw mechanism used in modern wind turbines; active and passive yaw. Active yaw consists of an electric or hydraulic motor in order to keep the rotor system aligned with the wind to capture the maximum energy from wind. In addition to power maximizing, active yaw mechanism protects the wind turbine to subject to fatigue loads. The other one is passive yaw mechanism which is generally used in downwind and smaller scale upwind wind turbines. In the passive yaw mechanism, there is a tail wing or rotor system that functions as a tail wing and no power is needed for the yaw control. However, passive yaw is instable and less efficient than active one [10]. Figure 1.19 shows a typical yaw drive mechanism.



**Figure 1.19** Yaw Drive Mechanism [19]

**Tower:** The main goal of the tower is to carry the wind turbine components and to increase the power output by means of elevating the rotor to a higher altitude for to meet higher wind speeds. The stiffness of the turbine has a significant importance in wind turbine dynamics for this reason, tower should be designed to meet the safety requirements and endure all the forces and bending moments caused by varying wind conditions. Figure 1.20 shows the complete wind turbine system with tower and foundation.



**Figure 1.20** Complete Wind Turbine System with Tower and Foundation [6]

**1.3 Literature Review**

Due to the nature of the wind, wind turbine blades are subjected to highly variable loads and stresses. When varying loads are combined with the large elastic

structures, an interaction is formed between the structure deformations and the aerodynamic forces and this causes unwanted flapwise-edgewise vibrations and devastating structural failures. Therefore; it is important to investigate the aeroelastic instabilities of the rotor blades and optimize the interplay between the aerodynamic loads and blade structure. For this purpose, numerous studies on the aeroelastic analysis of the wind turbine rotor blades have been made in wind turbine industry and this section outlines the studies and design codes about the aeroelasticity of the wind turbine blades.

One of the first researches on aeroelastic analysis of the wind turbines was conducted by Friedmann in 1976 [58]. Friedmann derived flap-torsion coupled equations of motion to determine the aeroelastic responses of the wind turbine blade. Two years later, Ottens conducted a review about the stability and dynamic response calculations of the horizontal axis wind turbine and this work was offering a method for whole wind turbine model [59].

In 1983, Garrad published a review of dynamic problems encountered in wind turbine systems, and discussed the dynamics of wind turbine behavior in three principal aspects which were stability, forced response to deterministic loads and forced response to stochastic loads [60].

In these early studies, external loads on wind turbine were evaluated by utilizing quasi-static aerodynamic calculations, with ignoring the effects of structural dynamics or including an estimated dynamic magnification factors for each component of the wind turbine [61]. However, it was realized that the models based on the quasi-static aerodynamic computations give comparative results only for wind turbines those have rigid blades or small wind turbines. Therefore, new aeroelastic tools with computer codes have been developed for dynamic analysis of the large and flexible wind turbines.

One of the first aeroelastic design tool, STALLVIB was developed under the European Non-Nuclear Energy program JOULE III [61]. This tool was developed for prediction of the dynamic loads and investigating the edgewise vibration problems in the fundamental blade natural mode shape caused by negative aerodynamic damping with quasi-steady and unsteady aerodynamics for stall regulated wind turbines.

After the first attempts, a significant number of codes and tools were developed at the universities and research laboratories. Following design codes are the most well-known codes in the market to predict the aeroelastic behavior and carry out the wind turbine designs;

- ADAMS/WT (Automatic Dynamic Analysis of Mechanical Systems – Wind Turbine) is an add-on wind turbine module for multi-body dynamic code ADAMS and it is designed for modelling and analyzing the dynamic behaviors of horizontal-axis wind turbines of different configurations [63].
- BLADED for Windows is an integrated software package which utilizes a completely self-consistent and rigorous formulation of the structural dynamics [64]. The design tool offers accurate results for wind turbine performance prediction and external loading calculations required for the design and certification of the wind turbines.
- DUWECS (Delft University Wind Energy Converter Simulation) is the design code of DELFT University and it is developed to optimize flexible horizontal-axis wind turbines [65].
- FAST (Fatigue, Aerodynamics, Structures, and Turbulence) code is developed by the corporation of National Renewable Energy Laboratory (NREL) and Oregon State University (OSU) to model the wind turbine as a combination of rigid and flexible bodies [66].

- HAWC (Horizontal Axis Wind Turbine Code) is an aero-elastic code which is developed at Risø National Laboratory, Denmark [67]. It offers improved aeroelastic modeling for intermediate horizontal-axis wind turbine designs.

#### **1.4 Scope of the Thesis**

This thesis was devoted to conduct a comparative study of transient and quasi-steady aeroelastic analysis of a NREL Phase VI composite wind turbine blade in steady wind conditions. Moreover, the applicability of quasi-steady aeroelastic modeling of the wind turbine blade in steady wind conditions is investigated by comparing the obtained deformation results and root bending moment results of transient and quasi-steady analysis at the same azimuthal position.

In Chapter 2, basic aerodynamic models of horizontal axis wind turbines are defined and necessary equations have been derived. At the end of the chapter, Blade Element Momentum theory based iterative algorithm is developed for the calculation of aerodynamic loads distributed over the reference NREL blade.

In Chapter 3, the inverse design methodology of the reference blade is conducted. Initially, composite materials used at skin, spar and root are selected and then the ply orientation of the materials are decided by using the Variational Asymptotic Method (VAM) based tools PreVABS and VABS. After obtaining the sectional ply numbers and ply orientations, three dimensional finite element model of representative sections are generated by using MSC®/PATRAN to conduct the structural analysis. For verification of the 3-D FE model, modal analyses are performed for the first four global mode shapes. Then for initial case of quasi-steady aeroelastic analysis, BEM based algorithm which is developed at Chapter 2 is followed and obtained aerodynamic results are coupled with the FE model in MSC®/NASTRAN. Results of the quasi-steady aeroelastic analysis of the reference blade are presented and detailed. For the second case of the quasi-steady aeroelastic analysis, almost same procedure is followed for computing the aero loads but the only difference is that the

blade is divided in 10 discrete parts while performing the BEM solution. The calculated loads are distributed over the blades by using MSC®/PATRAN feature RBE3 elements. Furthermore, centrifugal effects are contributed in the analysis and deflection results are shown at the end of the chapter.

In Chapter 4, superelement model of the reference blade is completed at Samcef Field to conduct the transient analysis. The modal analysis results of the 3-D finite element model and superelement model is compared for verification. Then, created superelement model is implemented into multi-dynamic system and transient aeroelastic analysis are performed for 15 m/s steady wind conditions by using Samcef for Wind Turbine. Finally, the comparisons between quasi-steady and transient aeroelastic cases are presented.

In Chapter 5, general conclusions, recommendations and future works are given.

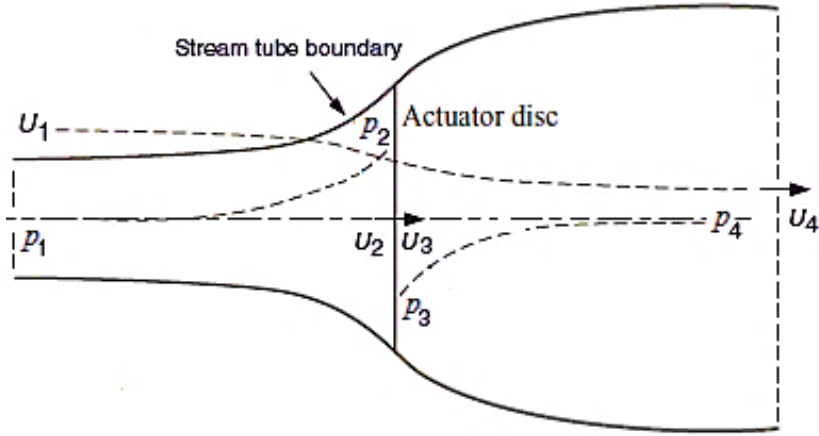
## CHAPTER 2

### ROTOR AERODYNAMICS

Accurate and effective models are essential to successfully analyze the interaction between the flow-field and the rotor surface. To build up the models and to compute the aerodynamic performance characteristics, various types of methods are used. In time, simple methods are developed besides the advanced numerical methods to solve the rotor aerodynamics of wind turbine systems with increasing level of complexity. In this chapter, a brief introduction of the most common models, starting from the actuator disk model is given, and the necessary equations are derived.

#### 2.1 The Actuator Disc Model (One-Dimensional Linear Momentum Theory)

The actuator disc model is the simplest aerodynamic model for a HAWT which is based on capturing the energy by decelerating the incoming wind flow with a homogenous disc [50]. In the actuator disc model, the homogenous-permeable rotor disc acts as a drag device in the control volume. This uniform disc creates a discontinuity in wind flow by decelerating the wind speed from the far upstream velocity ( $U_1$ ) to the rotor plane ( $U_2$ ) and to the far wake ( $U_4$ ). While the wind speed slows down, small increment is observed in the pressure from  $p_1$  to  $p_2$ , before the discontinuous pressure drop ( $p_2$  to  $p_3$ ) across the rotor as shown in Figure 2.1.



**Figure 2.1** Discontinuous Pressure Drop across the Rotor [23]

Under the assumptions of ideal rotor with steady conditions, total energy remains constant in the control volume. Thus, by applying Bernoulli's equation, thrust can be derived as;

$$T = \frac{1}{2} \rho A (U_1^2 - U_4^2) \quad (2.1)$$

We now consider the momentum equation and if it is assumed that there is no net change of momentum in the by-pass flow, thrust can also be found as the rate of change of the linear momentum from upstream to downstream. Rate of change of the linear momentum is the overall change of velocity times the mass flow rate. Considering the mass flow rate ( $\dot{M}_a = \rho AU$ ) is same at each point of the control volume, thrust equation becomes

$$T = \rho_\infty AU (U_1 - U_4) \quad (2.2)$$

Equations (2.1) and (2.2) are equal and mass flow rate at the upstream of the disc is  $\dot{M}_2 = \rho A_2 U_2$ . Therefore one can express  $U_2$  in terms of  $U_1$  and  $U_4$  as



$$U_2 = \frac{1}{2}(U_1 + U_4) \quad (2.3)$$

The wind velocity at the front face of the disc is the arithmetic mean of the upstream and downstream velocities. For convenience, axial induction factor “ $\alpha$ ” is introduced which is the influence of the disc on the wind speed, and it is formulated as;

$$U_2 = U_1(1 - \alpha) \quad \text{and} \quad U_4 = U_1(1 - 2\alpha) \quad (2.4)$$

“ $U_1\alpha$ ” can be introduced as the induced velocity across the rotor plane. By the increasing the axial induction factor, the wind speed behind the rotor slows down. Thus, “ $\alpha$ ” should be placed in the power equations as

$$P = \frac{1}{2}\rho AU^3 4\alpha(1 - \alpha)^3 \quad (2.5)$$

Wind turbine rotor performances are usually characterized by its non-dimensional power and thrust coefficients, they are established as;

$$C_T = T / \frac{1}{2}\rho U^2 A = 4\alpha(1 - \alpha) \quad \text{and} \quad C_P = P / \frac{1}{2}\rho U^3 A = 4\alpha(1 - \alpha)^2 \quad (2.6)$$

The maximum conversion value of energy can be achieved by taking the derivative of the power coefficient with respect to “ $\alpha$ ” and known as the Betz limit [23].

$$C_{P_{max}} = 16/27 = 0.5926 \quad (2.7)$$

Because of the rotational wake, non-zero aerodynamic drag and finite numbers of blade, the maximum theoretically achievable rotor power coefficient is limited by Betz factor given by Eqn. (2.7). In practice, this limit decreases to almost 45% when

the mechanical efficiency of turbine parts and other losses are taken into account. In summary, actuator disc model does not describe the complex physics behind the wind turbine aerodynamics. However, actuator disc model helps in understanding the basic operation principle of the wind turbine system.

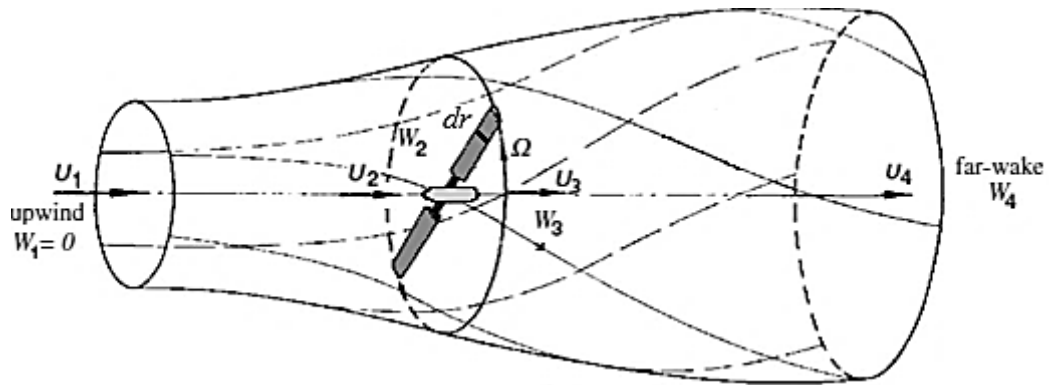
### 2.2 Rotor Disc Theory (Angular Momentum Theory)

For the ideal rotor, it was postulated that there is no rotational movement behind the rotor plane. However, this assumption is no longer applicable for the rotor disc theory. In the rotor disc theory, the airflow behind the rotor plane gains some rotation just because rotating turbine rotor generates angular momentum. The increase in angular momentum creates a torque and according to Newton’s Third Law, there should exist an equal and opposite direction torque to be imposed upon the flow behind rotor. As a consequence of the imposed torque, the air behind the rotor rotates in the opposite direction to the rotor [6]. Figure 2.2 shows the rotation of the airflow in the opposite direction of the rotation of the rotor behind the rotor.



**Figure 2.2** Airflow Rotates in the Opposite Direction behind the Downwind Turbine Rotor [24]

The increase in the rotational velocity of airflow results a decrease in energy extraction and this is taken into account in power calculations. In order to obtain the maximum power output, it is necessary to minimize the rotational kinetic energy at the wake and this can be achieved by a higher angular velocity and lower torque. Figure 2.3 gives a picture depicting the angular velocities induced.



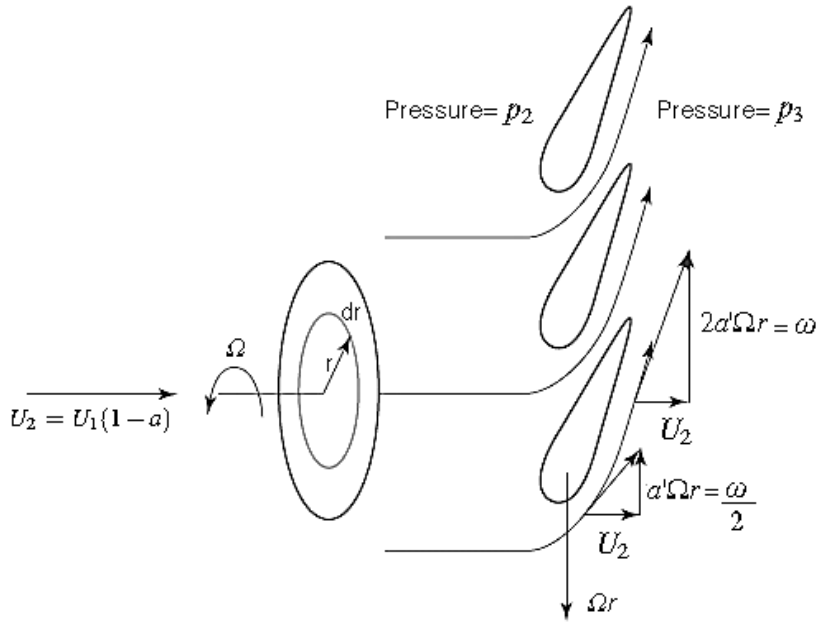
**Figure 2.3** Extended Momentum Theory, Taking into Consideration the Rotating Rotor Wake [19]

If no swirl is assumed at the upstream, the difference at in the rotational speed across the rotor can be defined as:

$$\omega_{average} = \frac{\omega_2 + \omega_3}{2} = \omega/2 = a'\Omega \quad (2.8)$$

Here  $\omega$ , is the local angular velocity of the flow and  $\Omega$  is the angular speed of the rotor.

As mentioned in the actuator disc model, total energy remains constant in control volume. The only difference is the increase in the angular velocity of the air relative to rotor from  $\Omega$  to  $\Omega + \omega$ , while the axial velocity across the disc remains same. Figure 2.4 shows the schematic of the rotor disk theory [23].



**Figure 2.4** Schematic of the Rotor Disk Theory [23]

By applying Bernoulli's equation between the stations 2 and 3, pressure difference and differential thrust  $dT$  can be formulated as in terms of the induction factor  $a'$ ;

$$dT = 4a'(1 + a') \frac{1}{2} \rho \Omega^2 r^2 \pi r dr \quad (2.9)$$

And equating the two thrust expressions Eqn. (2.6) with Eqn. (2.9), gives;

$$\frac{a(1-a)}{a'(1+a')} = \frac{\Omega^2 r^2}{U^2} \quad (2.10)$$

$$\text{Tip Speed Ratio} = \lambda_r = \frac{\Omega R}{U} \quad (2.11)$$

After obtaining the thrust and tip speed ratio equations, torque and power equations can be derived by applying the conservation of angular momentum. As mentioned in

the beginning of this section, exerted torque should be equal to the increase in the angular momentum of the flow behind the rotor, therefore torque and power equations can be expressed as:

$$dQ = 4\pi\rho U(1 - a)a'\Omega r^3 dr \quad (2.12)$$

$$dP = 4\pi\rho U^3(a'(1 - a))\lambda_r^2 r dr \quad (2.13)$$

### 2.3 The Blade Element Momentum (BEM) Theory

Blade Element Momentum Theory [BEM] also known as “*Strip Theory*” is the most commonly used method to compute the aerodynamic loads and performance of the wind turbine rotor blades. Its methodology presents a reliable, robust aerodynamic model and its robustness is provided by a balanced combination of Rankine-Froude actuator disk theory and blade element theory. However, this combination causes some limitations as explained by Moriarty and Hansen [26]. In spite of the limitations, BEM calculations are fast and provide quite accurate results hence, the method is decided to be used as the primary method to compute the aerodynamic forces in this study.

In the blade element method, turbine blades are divided into small concentric annular elements along the spanwise direction, with each element having a particular angle of attack. These discrete elements are assumed to operate aerodynamically independent from adjacent ones which means no aerodynamic interaction and radial flow between the elements. To obtain the local forces and moments acting on related blade sections, general lift, drag and pitching moment equations are applied, as given by Eqn. ((2.14)-(2.16)).

$$L = C_L \frac{1}{2} \rho A U_{Rel}^2 c \quad (2.14)$$

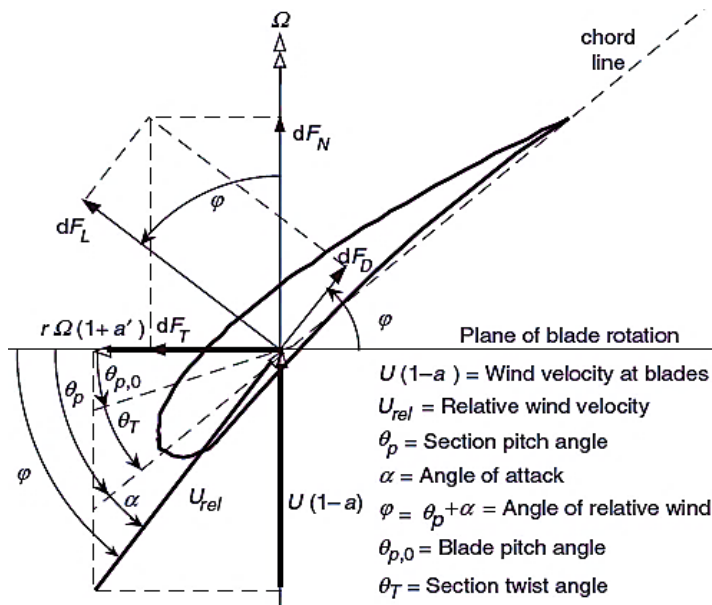
$$D = C_D \frac{1}{2} \rho A U_{Rel}^2 c \quad (2.15)$$

$$M = C_M \frac{1}{2} \rho A U_{Rel}^2 c^2 \quad (2.16)$$

where, L is the lift force per meter span, D is the drag force per meter span, M is the moment per meter span, c is the chord of the blade, and  $U_{Rel}$  is the relative incoming flow velocity to the blade elements.

As discussed in Section 2.1, induced velocities are calculated from the momentum lost in the axial and tangential flow fields. Induced velocities affect both the inflow and the loads calculated by blade element theory. The combination of these theories sets up an iterative process to obtain the lift and drag forces on each element, and afterwards forces acting on each element are summed over the total blade span.

Figure 2.5 shows the main parameters used for the blade element momentum calculations for each annular element.



**Figure 2.5** Local Blade Element Velocities and Aerodynamic Forces [26]

In blade element theory, each element is modeled as a two-dimensional airfoil; therefore all surface loads are functions of angle of attack. More precisely, to obtain the local forces exerted on the blade, angle of attack should be determined by the difference between the angle of inflow  $\varphi$  and the pitch angle of the blade  $\theta$ .

$$\alpha = \varphi - \theta \quad (2.17)$$

From Figure 2.5, inflow angle can be expressed as:

$$\tan \varphi = \frac{U(1 - a)}{r\Omega(1 + a')} \quad (2.18)$$

The incoming relative flow to the blade elements " $U_{Rel}$ " is the vector sum of the induced wind velocity at the rotor plane and the tangential velocity caused by the rotation of the blade. Thus, relative velocity can be found as:

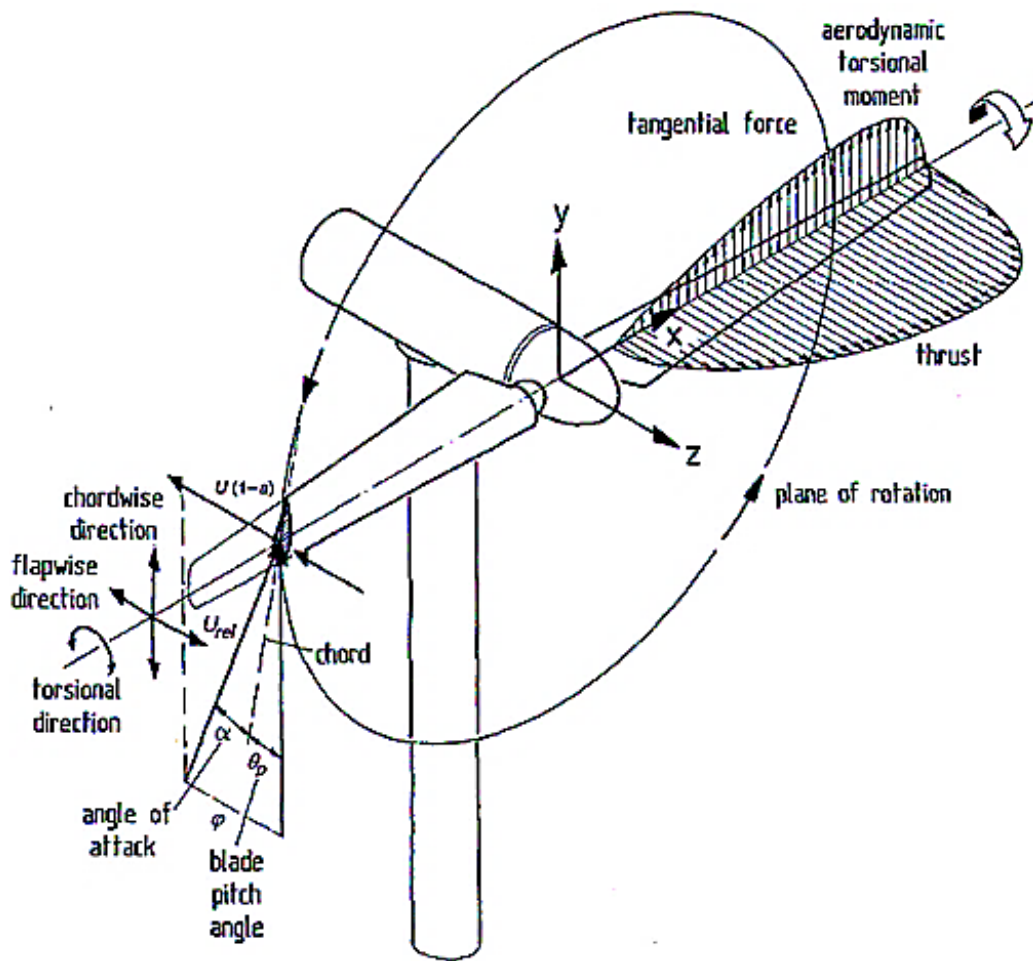
$$U_{Rel} = \sqrt{U_{Rotational}^2 + U_{Wind}^2} \quad (2.19)$$

$$U_{Rel} = [U(1 - a)]/\sin \varphi \quad \text{or} \quad U_{Rel} = [(\Omega r(1 + a'))]/\cos \varphi \quad (2.20)$$

From Figure 2.6, it is clearly seen how the lift and drag forces can be resolved in the perpendicular and parallel directions of the relative velocity. As an alternative way, the differential aerodynamic forces can be shown as normal force ( $F_N$  total force acting normal to the chord line, same force as the thrust) and tangential force ( $F_T$  total force acting parallel to the chord line).

$$dF_{Normal} = dF_{Lift} \cos \varphi + dF_{Drag} \sin \varphi \quad (2.21)$$

$$dF_{Tangential} = dF_{Lift} \sin \varphi - dF_{Drag} \cos \varphi \quad (2.22)$$



**Figure 2.6** Normal and Tangential Force Distribution over the Blade [19]

If the rotor consists of  $N$  identical blades, the total differential normal force on the section at a distance  $r$  from the rotational center is

$$dF_N = N(dF_{Lift} \cos \varphi + dF_{Drag} \sin \varphi) \quad (2.23)$$

By combining Eqn. (2.14), Eqn. (2.15) and Eqn. (2.23), differential normal force acting on the sectional blade element can be re-written as;



$$dF_N = N \frac{1}{2} \rho U_{Rel}^2 c dr (C_l \cos \varphi + C_d \sin \varphi) \quad (2.24)$$

Moreover, the differential torque produced by the element is equal to the torque created by the tangential force at distance  $r$

$$dQ = N \frac{1}{2} \rho U_{Rel}^2 c r dr (C_l \sin \varphi - C_d \cos \varphi) \quad (2.25)$$

By placing the relative wind velocity equation and introducing the chord solidity “ $\sigma'$ ” which is the total chord length at a given radius divided by the circumferential length, differential normal force and torque can be expressed by Eqs. (2.27) and (2.28), respectively.

$$\sigma' = \frac{Nc(r)}{2\pi r} \quad (2.26)$$

$$dF_N = \sigma' \pi \rho \frac{U^2 (1-a)^2}{\sin^2 \varphi} (C_l \cos \varphi + C_d \sin \varphi) r dr \quad (2.27)$$

$$dQ = \sigma' \pi \rho \frac{U^2 (1-a)^2}{\sin^2 \varphi} (C_l \sin \varphi - C_d \cos \varphi) r^2 dr \quad (2.28)$$

In the calculation of BEM theory, Wilson and Lissaman [48] decided to set the drag coefficient “ $C_d$ ” value to zero because the decrease at velocity caused by the drag is just observed at the narrow wake and have no effects on the pressure drop. This induced formula is used to calculate the induction factor by equating the torque equations Eqn. (2.12) with Eqn. (2.28) respectively;

$$\frac{a'}{(1-a)} = \frac{\sigma' C_l}{4\lambda_r \sin \varphi} \quad (2.29)$$

And by equating the force equations Eqn. (2.9) with Eqn. (2.27) it is possible to obtain the axial induction factor;

$$\frac{a}{(1-a)} = \frac{\sigma' C_l \cos \varphi}{4 \sin^2 \varphi} \quad (2.30)$$

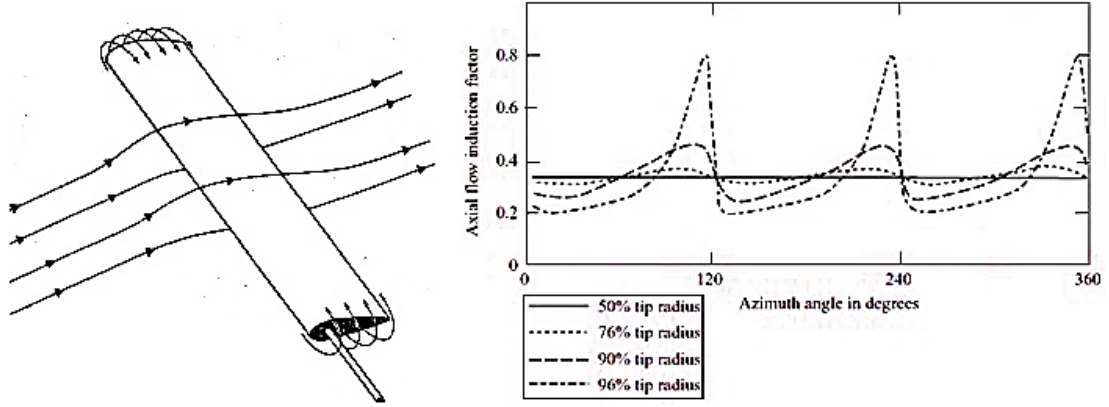
Induction factor equations Eq. (2.29) and Eq. (2.31) can be simplified to;

$$a = \frac{1}{\left[1 + \frac{4 \sin^2 \varphi}{\sigma' C_l \cos \varphi}\right]} \quad (2.31)$$

$$a' = \frac{1}{\left[\frac{4 \cos \varphi}{\sigma' C_l} - 1\right]} \quad (2.32)$$

## 2.4 Loss Corrections

It was previously mentioned that BEM has some limitations and one of the major one is that there is no influence of tip and hub vortices in the induced velocity distributions. Because of the airfoil characteristics, air tends to flow around the tip from the high pressure surface to low pressure surface by creating tip vortices. These vortices are being shed and create multiple helical structures in the wake and this cause non-uniform circulations and high axial induction factors [34]. High induction factor means a decrease at inflow velocity and inflow angle which cause a reduction in the aerodynamic lift and affects the power output produced by the turbine. Figure 2.7 shows the tip loss flow diagram and azimuthal variation at various radial positions of the blade.



**Figure 2.7** Tip Loss Flow Diagram and Azithimuthal Variation at Various Radial Positions of the Blade [23, 30]

To compensate for this deficiency, some adjustments or corrections is needed, and the most common tip loss correction model is developed by Prandtl. [23]. According to Prandtl's tip loss model, a correction factor “ $F$ ” is used to modify the force and torque formulas derived from the momentum equations. For optimum operation, uniform circulation should be provided by the uniform axial flow induction factor across the disc. Prandtl's tip loss correction factor, given by Eqn. (2.33) is used to account for the non-uniformity of the axial induction factor [31].

$$F = \frac{2}{\pi} \arccos \left[ e^{-\frac{(N/2)(1-(r/R))}{(r/R)\sin\phi}} \right] \quad (2.33)$$

A similar loss model takes place at the root of the blade to correct the induced velocity resulting from a vortex being shed near the hub of the rotor [33]. The hub-loss model uses a nearly identical implementation of the Prandtl's tip-loss model. Hub loss factor is defined by:

$$F = \frac{2}{\pi} \arccos \left[ e^{-\frac{(N/2)(1-(r/R_{Hub}))}{(r/R_{Hub})\sin\phi}} \right] \quad (2.34)$$

So, total effective loss factor at any blade section can be found by the product of the two loss factors.

$$F_{Total} = F_{Tip} \cdot F_{Root} \quad (2.35)$$

Effective loss correction factor is applied to the normal force, torque, axial and tangential induction factor equations to correct for the losses associated with the tip and hub wake losses in Eqn. (2.36) and Eqn. (2.37)

$$dT = 4F\rho U^2 \alpha (1 - \alpha) \pi r dr \quad (2.36)$$

$$dQ = 4F\pi\rho U (1 - \alpha) \alpha' \Omega r^3 dr \quad (2.37)$$

$$\alpha = 1/[1 + 4F \sin^2 \varphi / \sigma' C_l \cos \varphi] \quad (2.38)$$

$$\alpha' = 1/[(4F \cos \varphi / (\sigma' C_l)) - 1] \quad (2.39)$$

## 2.5 Calculation of the Blade Element Forces and Power Output

The conventional algorithm for the calculation of the aerodynamic loads is described below. The listed process should be repeated until the newly calculated axial and angular induction factors are within the tolerance of the previous ones [10] and after achieving a convergent result, aerodynamic loads and power coefficient can be computed.

1. Initialize  $\alpha$  and  $\alpha'$ .
2. Compute the flow angle “ $\varphi$ ” by using Eqn. (2.18) and local angle of attack “ $\alpha$ ” by using the section pitch angle Eqn. (2.17).
3. Read lift ( $C_L$ ) and drag coefficient ( $C_D$ ) values of the chosen airfoil for the given Reynolds Number from look-up table.

4. Calculate total loss factor " $F$ " using Eqs. (2.33, 2.34 and 2.35).
5. Compute  $dT$  and  $dQ_T$  using Eqs. (2.27 and 2.28).
6. Calculate new values of  $a$  and  $a'$  again by using Eqs. (2.38 and 2.39). If  $a$  and  $a'$  have changed more than a certain tolerance (for ex: tolerance  $> 0.01$ ), go to "2" or else finish.
7. After having determined the induction factors, compute the local loads on the blade segments.

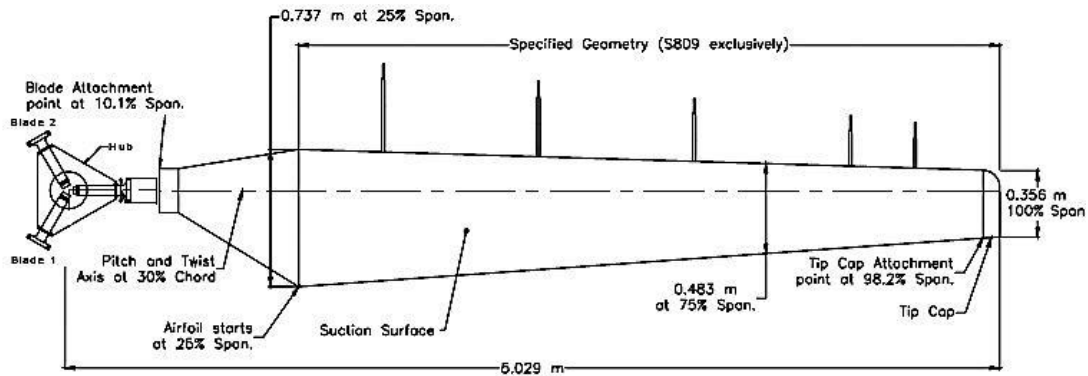


## CHAPTER 3

### INVERSE DESIGN OF THE REFERENCE BLADE AND QUASI-STEADY AEROELASTIC ANALYSIS OF THE WIND TURBINE BLADE

Rotor blades are the most critical composite based structures of the wind turbine system and their design process is probably the most challenging and problematic part. Blades are exposed to various types of external loadings originated from wind, gravity and dynamic interactions; hence, the selection of composite materials and airfoil type is very crucial at the preliminary design step to provide the optimal aerodynamic performance and long-lasting fatigue life. Therefore, realistic composite blade modeling is an indispensable part in the process of wind turbine design [17]. In the present study, unsteady aerodynamics experiment (UAE) research wind turbine NREL Phase VI is chosen as the reference turbine model [15] to perform the inverse design and conduct quasi-steady aeroelastic analysis to compare against the transient aeroelastic analysis of the wind turbine system. The particular rotor of wind turbine is composed of three blades and each blade length is measured as 5.029 m from hub centerline to the blade tip. The rotor is mounted on a Grumman wind stream 33 horizontal axis wind turbine, which is a stall-regulated and full-span pitch control capable machine having a rated power of approximately 20 kW and operating at a nominal speed of 72 rpm. System cut-in wind speed is 6 m/s and the hub height is decided as 12.192 m above ground level. As illustrated in Figure 3.1, the root of the blade starts at the hub connection, at a radius of 508 mm from the center of the hub. Between the 0.508 m and 0.660 m stations, the second part of the blade root is designed as cylindrical and then transition part lies between the 0.660 m and 1.257 m stations. The third and the final part of the three-bladed system has NREL S809

airfoil shape from end of the transition part to tip with linear taper and a nonlinear twist distribution.



**Figure 3.1** Geometric Presentation of the Wing Studied [15]

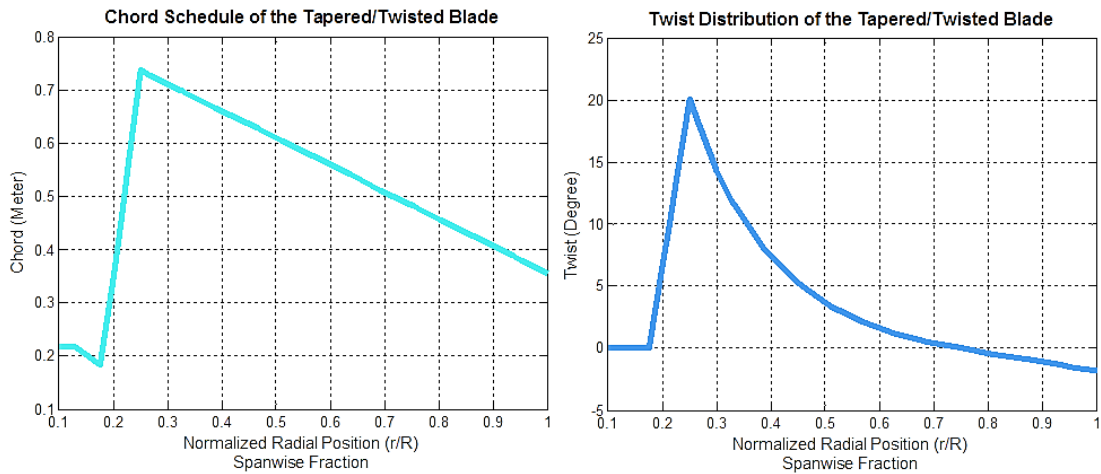
**Table 3.1** Chord and Twist Distributions of NREL Phase VI Blade [41]

Radial Sections	Distance from Rotor Center (m)	Spanwise Fraction (.../5.029)	Local Chord Length (m)	Local Twist (degree)	Local Thickness (m)
1	0	0	hub	hub	hub
2	0,508	0,101	0,218	0	0,218
3	0,660	0,131	0,218	0	0,218
4	0,883	0,176	0,183	0	0,183
5	1,008	0,200	0,349	6,700	0,163
6	1,067	0,212	0,441	9,900	0,154
7	1,133	0,225	0,544	13,400	0,154
8	1,257	0,250	0,737	20,040	0,154
9	1,343	0,267	0,728	18,074	0,153
10	1,510	0,300	0,711	14,292	0,149
11	1,648	0,328	0,697	11,909	0,146
12	1,952	0,388	0,666	7,979	0,140
13	2,257	0,449	0,636	5,308	0,133
14	2,343	0,466	0,627	4,715	0,131
15	2,562	0,509	0,605	3,425	0,127
16	2,867	0,570	0,574	2,083	0,120
17	3,172	0,631	0,543	1,150	0,114
18	3,185	0,633	0,542	1,115	0,114
19	3,476	0,691	0,512	0,494	0,107
20	3,781	0,752	0,482	-0,015	0,101
21	4,023	0,800	0,457	-0,381	0,096
22	4,086	0,812	0,451	-0,475	0,094
23	4,391	0,873	0,420	-0,920	0,088
24	4,696	0,934	0,389	-1,352	0,081
25	4,780	0,950	0,381	-1,469	0,080
26	5,000	0,994	0,358	-1,775	0,075
27	5,029	1,000	0,355	-1,815	0,074



NREL S809 airfoil is a 21-percent-thick, laminar-flow airfoil which was designed for HAWT applications, analyzed theoretically and verified experimentally in wind tunnels at the Delft University of Technology [36] and The Ohio State University [35] for the different Reynolds Number values. Hence, it has a well-documented wind tunnel data base which includes pressure distributions, flow-visualization data and two dimensional aerodynamic data that are used in aerodynamic calculations.

Table 3.1 and Figure 3.2 give the blade chord and twist distributions of the NREL Phase VI blade [41]. From Table 3.1, it can be seen that blade is separated into 27 radial sections. All local twist angles are adjusted according to the point of zero twist which is placed at the 75% span (3.772 m) and convention of the twist distribution is positive toward feather. Additionally, pitch and twist axes are established at 30% chord. According to given geometric data, the outer mold line design of the blade is performed, and the design is completed in an inverse fashion as explained in the following sections.



**Figure 3.2** Chord and Twist Distribution of the NREL Blade

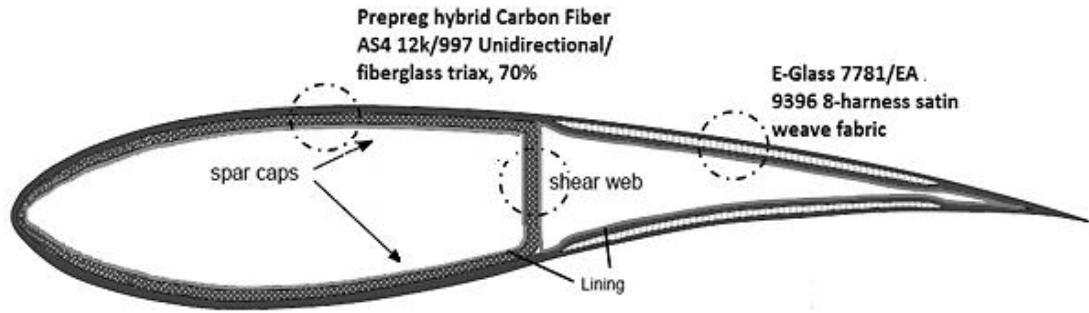
### 3.1 Selection of Composite Materials for the Blade

In order to build the three dimensional finite element model of the composite blade, all the material properties and the ply zone/sequence data should be known.

However, except for the sectional properties, material and ply zone/sequence data cannot be found in the literature [15]. To build up the finite element model of the blade, material property selection is a key issue. While making the selection of the materials, reducing the excessive weight to minimize the gyroscopic and inertial loads to avoid the blade fatigue is also crucial. Because of these limitations, most commonly, composite materials such as fiberglass-epoxy and carbon-epoxy are preferred in the wind turbine industry instead of aluminum and steel to be used in the thin walled structures like the skin of the rotor blades. However, for the particular blade, detailed description and the lay-out of the materials used are not available in the literature [15]. To conduct the comparative study of quasi-steady aeroelastic and transient aeroelastic analysis, a reference blade is needed which has realistic stiffness and mass properties. Therefore, in the current study a baseline material selection is made for the composite materials to be used in the design of the blade, and inverse designs are performed section by section first by modeling the blade sections in PreVABS, and then calculating the sectional beam properties by VABS. Design iterations are performed and number of composite layers is modified to obtain closer sectional beam properties as the known sectional beam properties of the reference blade of the unsteady aerodynamics experiment (UAE) research wind turbine [15]. After a long survey, the ideal composite materials, that have high strength to weight ratio, are decided as:

- Prepreg hybrid Carbon Fiber AS4 12k/997 Unidirectional / fiberglass Triax, 70% 0° for the D-Spar cap [52].
- E-Glass 7781/EA 9396 8-harness satin weave fabric for rear part of the wing [52].

Figure 3.3 shows the composite materials used in the leading edge and the trailing edge section of the blade, and Table 3.2 and Table 3.3 give the mechanical properties of the composite materials used in the blade structure.



**Figure 3.3** Structure, Spar Location and Materials used in the Different Parts of the Blade [27]

Structurally speaking, unidirectional prepreg hybrid carbon-fiber is in the load carrying D-Spar which has a tapered thickness from root to tip. The non-load carrying rear part of the wing is completely made up of E-glass harness satin weave fabric.

**Table 3.2** Physical and Mechanical Properties of Prepreg Hybrid Carbon/Fiberglass Composite Triax, 70% 0° Unidirectional Type [27]

<b>Density</b>	1621 [ kg/m <sup>3</sup> ]
<b>Young's Modulus, <math>E_x</math></b>	74.305 [ GPa ]
<b>Young's Modulus, <math>E_y</math></b>	9.376 [ GPa ]
<b>Young's Modulus, <math>E_z</math></b>	9.376 [ GPa ]
<b>Shear Modulus, <math>G_{xy}</math></b>	4.863 [ GPa ]
<b>Poison's Ratio, <math>\nu</math></b>	0.35
<b>Tensile Strength</b>	2254 [MPa]
<b>Compression Strength</b>	1578 [MPa]
<b>Ply Thickness</b>	0.00014224 [m]

**Table 3.3** Physical and Mechanical Properties of E-Glass Harness Satin Weave  
Fabric 7781/EA93 [27]

<b>Density</b>	1859 [ kg/m <sup>3</sup> ]
<b>Young's Modulus, <math>E_x</math></b>	23.786 [ GPa ]
<b>Young's Modulus, <math>E_y</math></b>	23.235 [ GPa ]
<b>Young's Modulus, <math>E_z</math></b>	23.235 [ GPa ]
<b>Shear Modulus, <math>G_{xy}</math></b>	5.225 [ GPa ]
<b>Poison's Ratio, <math>\nu</math></b>	0.21
<b>Tensile Strength</b>	333 [MPa]
<b>Compression Strength</b>	319 [MPa]
<b>Ply Thickness</b>	0.0002159 [m]

### 3.2 Variational Asymptotic Beam Section Analysis; PreVABS and VABS

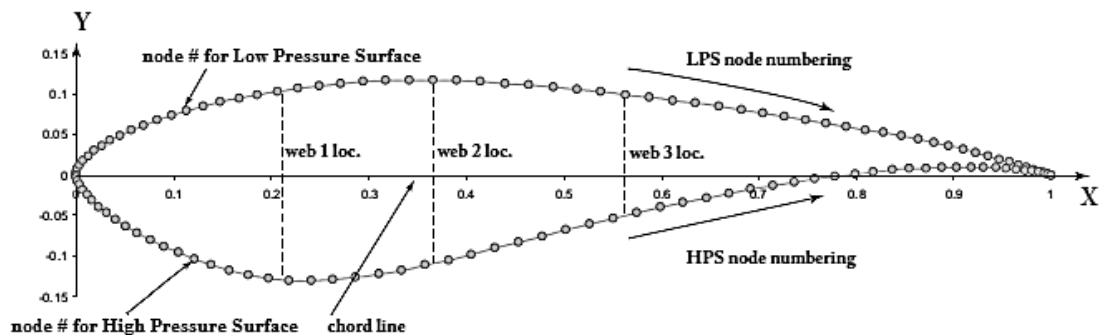
To evaluate the strength and to predict the static/dynamic/aeroelastic behaviors of the blade, it is necessary to model the cross-sectional beam properties of the blade at several sections along the span of the blade so that 3-D finite element model of the blade can be generated. Accurate sectional properties can be obtained by utilizing ply orientation and ply thickness information for each section of the 3-D blade structure. With regard to the selection of composite materials, due to the complexity of structural model, PreVABS [29] and VABS (Variational Asymptotic Beam Sectional) [28] analysis programs are used to design the blade sections such that sectional beam properties of the blade approximately match the sectional blade properties which are given by Hand et.al. [15].

PreVABS and VABS are computer based cross-sectional analysis programs which are capable of realistic modeling of initially twisted and tapered blades with arbitrary

sectional topology and material constructions. These two programs are coupled to each other, such that PreVABS works as the input provider for VABS. PreVABS has the capability of generating the complex structural cross-sectional configurations for helicopter and wind turbine rotor blades with high resolution finite element mesh by manipulating the geometry of blade section, mesh parameters, nodal coordinates, material properties and material lay-up configurations.

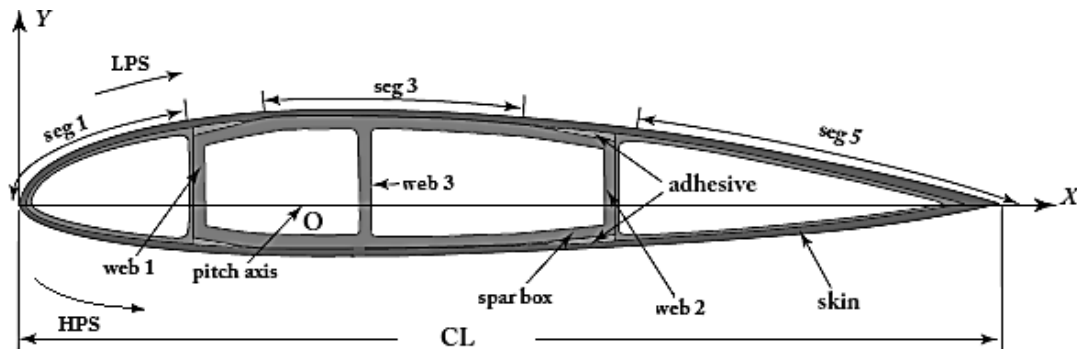
Basically, PreVABS program uses three input files that are shown in APPENDIX A to generate the necessary files for cross-sectional analysis:

1. **The airfoil geometric data file;** which includes the specification of blade airfoil configuration and it consists of three main sections;
  - a. **Blade Section Profile:** This portion includes the chord length of blade section ( $CL$ ), twist of the blade section ( $\theta_{Twist}$ ) and pitch axis location of the section ( $Cent_x$  and  $Cent_y$  in airfoil coordinate system, where rotor blade span axis is defined along the z axis while the chord length is the x axis).
  - b. **Webs:** Arbitrary number of webs, non-dimensional position for web centers ( $X_{web}$  and  $Y_{web}$ ) and web orientations with respect to the chord line (tilting angle in degree) are defined.
  - c. **Airfoil Profile:** This section describes the non-dimensional outer profile data of the airfoil for low pressure surface (LPS) and high pressure surface (HPS).



**Figure 3.4** Schematic Representation of an Airfoil Profile in PreVABS [15]

2. **The cross-sectional laminate lay-up data file;** defines the composite laminate lay-up for the blade sections which may vary in the chordwise and the spanwise directions. As shown in Figure 3.4, this file identifies the sections in two parts that are the “*Low Pressure Surface (LPS)*” and the “*High Pressure Surface (HPS)*”. Both LPS and HPS lie between the initial node of the leading edge and final node of the trailing edge. Then, these surfaces can be separated into several segments and depending on the variation of the total number of lamina, fiber orientations, material type and number of shear webs that exist. These segments are numbered in sequence according to varying structural properties as illustrated in Figure 3.5.

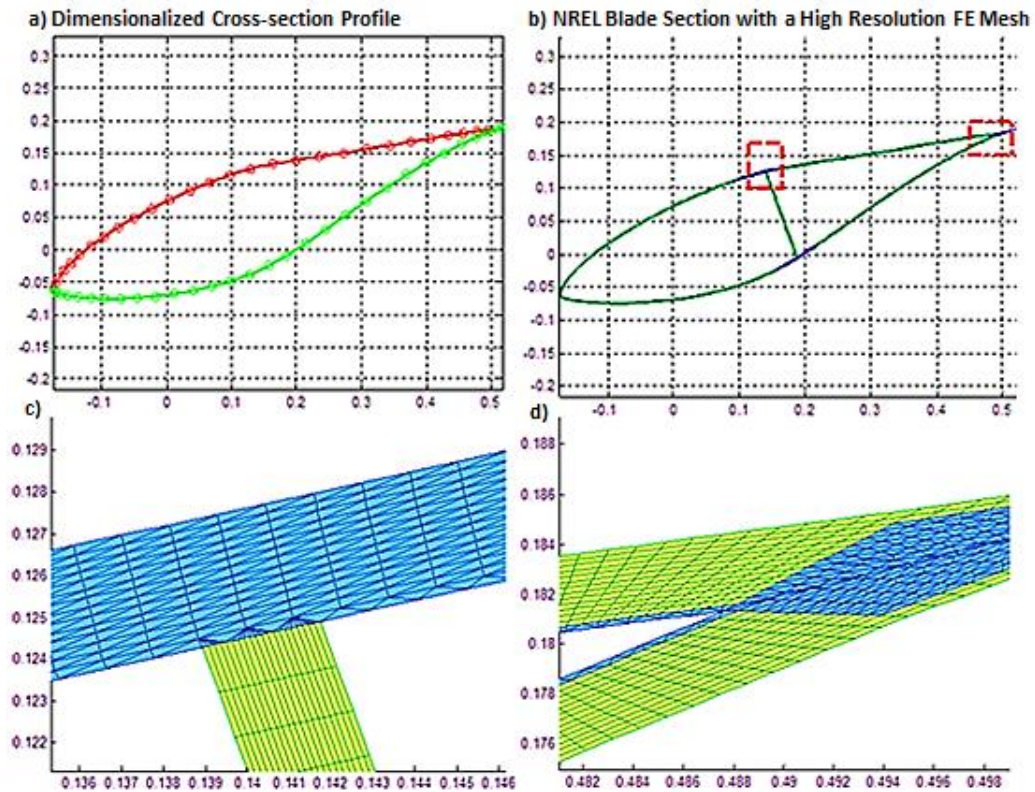


**Figure 3.5** Segmented Blade Cross-Section Definitions for PreVABS [15]

3. **The material property data file;** starts with the specification of the structural analysis models. Generalized Timoshenko model, linear - nonlinear beam models or the Vlasov model can be chosen for characterizing the 3-D displacement analysis and building the stiffness matrices. Besides, the physical and mechanical properties of the materials that are used to build up the segments of the blade sections are also defined in this file.

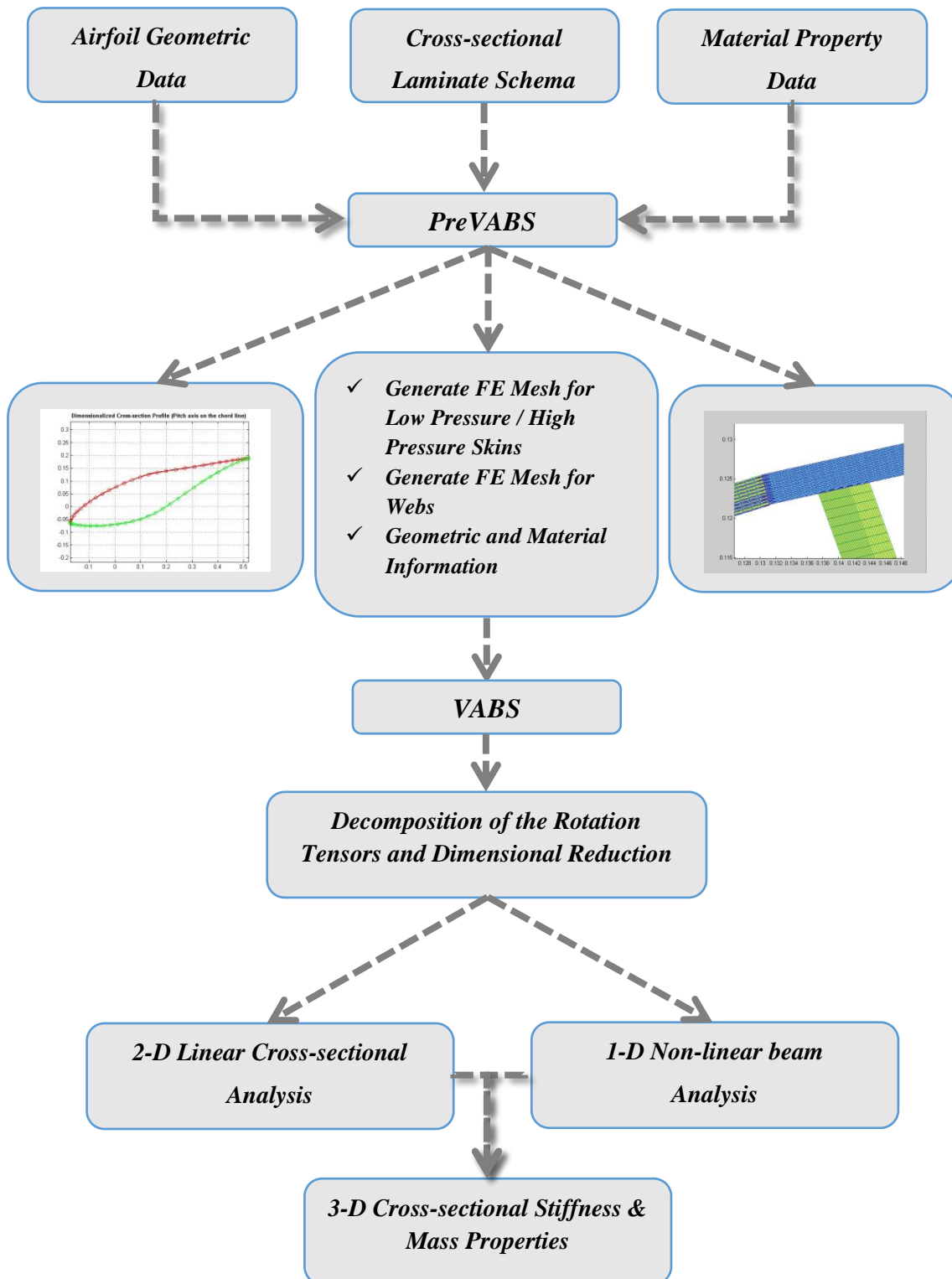
After defining the key files, PreVABS automatically generates high resolution finite element mesh on the cross-section of the blade in accordance with the input desired by the VABS solver system. Moreover, as it can be seen from Figure 3.6, PreVABS

also provides visualization of the finite element mesh of the blade section to check the quality of the mesh for further refinement, if necessary.



**Figure 3.6** PreVABS Modeling of NREL Blade Section. (a) Dimensionalized Cross-section Profile of the NREL Inverse Design Blade (b) High Resolution Finite Element Mesh on the Cross-section of the Blade (c) Zoomed View of the Spar-Skin Connection (d) Zoomed View High Resolution Finite Element Mesh at the Trailing Edge

After generating the output from PreVABS, VABS program takes the high-resolution finite element meshed complex structural model as input and analyses the sectional stiffness, inertial properties and mass properties as described in flow chart given in Figure 3.7. While performing the structural analysis, VABS uses the Variational Asymptotic Method (VAM) to resolve or decompose a nonlinear 3-D anisotropic elasticity problem into a 2-D, linear cross-sectional analysis and a 1-D non-linear beam analysis [37].



**Figure 3.7** VABS - PreVABS Coupling Flow Chart and Decomposition of a Three-Dimensional Blade into Two-Dimensional Cross-section and a One-Dimensional Beam

[25]



The output files of the constitutive VAM analysis include;

- 1) 6x6 sophisticated blade cross-section mass matrix given by Eqn.(3.1). According to given mass matrix information VABS calculates the mass per unit span ( $\mu$ ), mass center of the cross-section ( $\mu x_{m2}, \mu x_{m3}$ ), 6x6 mass matrix given at the mass center and the mass properties with respect to the principal inertial axes like mass moment of inertia ( $i_{22}, i_{23}, i_{33}$ ) and mass-weighted radius of gyration which is the square of the sum of the two in-plane cross-sectional mass moments of inertia divided by the mass per unit span.

$$\begin{bmatrix} \mu & 0 & 0 & 0 & \mu x_{m3} & -\mu x_{m2} \\ 0 & \mu & 0 & \mu x_{m3} & 0 & 0 \\ 0 & 0 & \mu & \mu x_{m2} & 0 & 0 \\ 0 & -\mu x_{m3} & \mu x_{m2} & i_{22} + i_{23} & 0 & 0 \\ \mu x_{m3} & 0 & 0 & 0 & i_{22} & i_{23} \\ -\mu x_{m2} & 0 & 0 & 0 & i_{23} & i_{33} \end{bmatrix} \quad (3.1)$$

- 2) VABS can also construct the Euler-Bernoulli beam type 4x4 stiffness matrix, given by Eq.(3.2) for the beam model.

$$\begin{bmatrix} EA & 0 & 0 & 0 \\ 0 & GJ & 0 & 0 \\ 0 & 0 & EI_2 & 0 \\ 0 & 0 & 0 & EI_3 \end{bmatrix} \quad (3.2)$$

VABS performs cross-sectional analyses by combining the energy method and Variational Asymptotic Method. The strain energy of the cross-section, or the strain energy per unit length of a beam, can be written as,

$$U = \frac{1}{2} \int_A \Gamma^T D \Gamma \sqrt{g} \, dydz \quad (3.3)$$

where,  $\Gamma$  is the 3-D strain field,  $D$  is the 6x6 symmetric elastic coefficient matrix in the local Cartesian system of the undeformed beam, and  $g$  is the determinant of the metric tensor for the undeformed geometry [44]. By using the VAM, the 3-D strain energy formula can be written as a series of asymptotically correct energy terms.

$$U = U_0 + U_1 + U_2 + \dots \quad (3.4)$$

where,  $U_0, U_1$  and  $U_2$ , are zeroth-order, first-order, and second-order approximations of the strain energy, respectively. By differentiating the strain energy with respect to the generalized Timoshenko 1D strain measures, 1-D constitutive law and generalized Timoshenko model for initially curved and twisted beams, which is given by the 6x6 stiffness matrix Eqn.(3.5) for the six fundamental global deformations can be obtained. Six fundamental deformations include transverse shear and bending in two directions, extension, and twist.

$$\begin{pmatrix} F_1 \\ F_2 \\ F_3 \\ M_1 \\ M_2 \\ M_3 \end{pmatrix} = \begin{bmatrix} S_{11} & S_{12} & S_{13} & S_{14} & S_{15} & S_{16} \\ S_{12} & S_{22} & S_{23} & S_{24} & S_{25} & S_{26} \\ S_{13} & S_{23} & S_{33} & S_{34} & S_{35} & S_{36} \\ S_{14} & S_{24} & S_{34} & S_{44} & S_{45} & S_{46} \\ S_{15} & S_{25} & S_{35} & S_{45} & S_{55} & S_{56} \\ S_{16} & S_{26} & S_{36} & S_{46} & S_{56} & S_{66} \end{bmatrix} \begin{pmatrix} \gamma_{11} \\ 2\gamma_{12} \\ 2\gamma_{13} \\ \kappa_1 \\ \kappa_2 \\ \kappa_3 \end{pmatrix} = S \begin{pmatrix} \gamma_{11} \\ 2\gamma_{12} \\ 2\gamma_{13} \\ \kappa_1 \\ \kappa_2 \\ \kappa_3 \end{pmatrix} \quad (3.5)$$

where, the elements of the stiffness matrix  $S$  are such that  $S_{11}$  represents the extension,  $S_{22}$  and  $S_{33}$  represent the shear,  $S_{44}$  represents the twist,  $S_{55}$  and  $S_{66}$  represent the bending stiffness coefficients.  $2\gamma_{12}$  and  $2\gamma_{13}$  are the generalized strain measures. After obtaining the 6x6 stiffness matrix, finding the exact location of sectional beam shear center is essential as detailed in Reference [39]. Additionally, VABS can also capture the trapeze and 5x5 Vlasov stiffness matrix which is important especially for the open-section thin-walled beams [40]. A detailed example of a VABS output data is given in APPENDIX A.

### 3.3 VABS Modeling of the Wind Turbine Blade

While performing the inverse design of the reference blade, blade is divided into 10 discrete sections in accordance with the sectional beam properties of the UAE Phase VI blades given in Table 3.4 [41]. Spanwise and chordwise ply numbers are changed in an iterative fashion, and each blade section is evaluated in VABS tool until the desired sectional beam properties approximately match with the known sectional beam properties of the UAE Phase VI blades.

**Table 3.4** Sectional Beam Properties of UAE Phase VI Blades [41]

<b>Distance from Center (m)</b>	<b>Blade Density (<math>\mu</math>)(kg/m)</b>	<b>Element Length (m)</b>	<b>Element Mass (kg)</b>	<b>Local Flap-wise Rigidity [EI](Nm<sup>2</sup>)</b>	<b>Local Edge-wise Rigidity [EI](Nm<sup>2</sup>)</b>	<b>Local Structural Twist (Degree)</b>
0.432	-	-	-	5.113 E+05	3.930 E+05	0
0.508	8.29	0.121	1.000	2.506 E+06	1.927 E+06	0
1.257	28.75	0.252	19.97	1.144 E+06	1.103 E+06	20.040
1.509	15.34	0.378	5.794	5.350 E+05	9.342 E+05	14.315
2.012	12.11	0.503	6.094	3.077 E+05	6.744 E+05	7.454
2.515	11.51	0.503	5.791	2.240 E+05	5.817 E+05	3.702
3.018	10.61	0.503	5.332	1.656 E+05	5.090 E+05	1.621
3.520	9.74	0.503	4.896	1.119 E+05	4.362 E+05	0.421
4.023	8.80	0.503	4.430	7.125 E+04	3.622 E+05	-0.381
4.526	7.88	0.503	3.967	3.920 E+04	3.134 E+05	-1.111
5.029	7.86	0.252	1.977	2.770 E+04	2.874 E+05	-1.815

However, without the actual knowledge of the complete material layout used in the blade, it would not be possible to match exactly the stiffness and the mass properties of the designed blade with the stiffness and mass properties of the reference NREL blade. Therefore, matching of the blade mass density is accomplished by assigning appropriate mass densities to the material in each blade section so that sectional blade mass densities approximately match the sectional blade mass densities of the

NREL blade. Although the assigned mass densities in each section do not reflect the actual density of the material used in the inverse design, the mass property of the designed blade approximately matches the mass property of the NREL blade. Table 3.5 presents the obtained local flapwise, edgewise properties and torsional stiffness values after performing PreVABS-VABS iterative analysis.

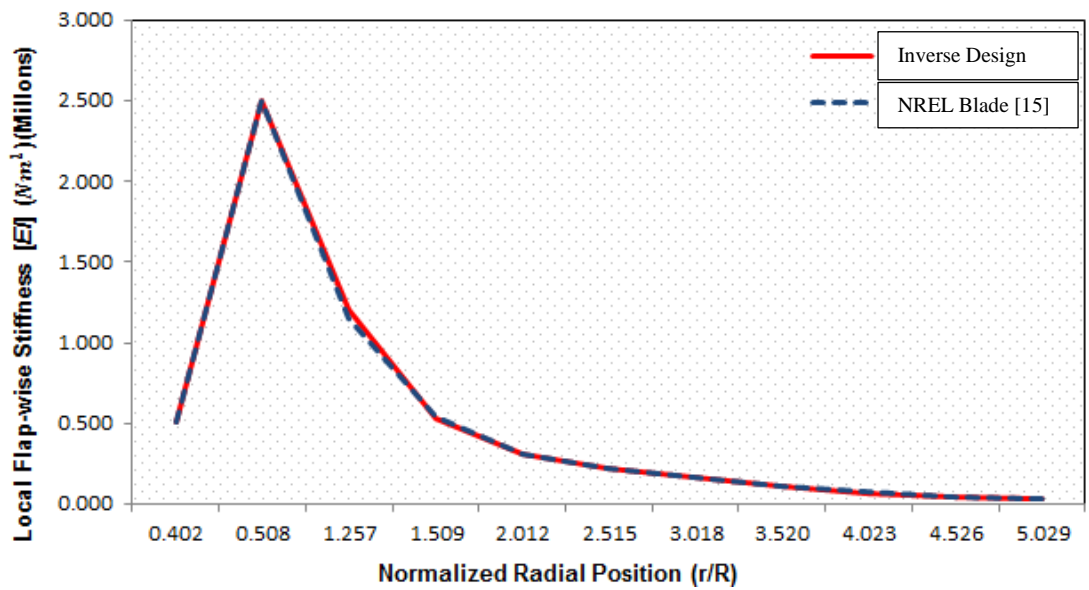
**Table 3.5** Sectional Beam Properties of the Inverse Designed Reference Blade

<b>Distance from Center (m)</b>	<b>Local Flapwise Rigidity [EI] (Nm<sup>2</sup>)</b>	<b>Local Edgewise Rigidity [EI] (Nm<sup>2</sup>)</b>	<b>Local Torsional Rigidity [GJ] (Nm<sup>2</sup>)</b>	<b>Element Mass (kg)</b>
1.257	1.208 E+06	6.934 E+06	2.991 E+05	14.164
1.509	5.336 E+05	5.524 E+06	2.417 E+05	6.413
2.012	3.048 E+05	4.494 E+06	2.178 E+05	8.282
2.515	2.226 E+05	3.636 E+06	1.107 E+05	7.347
3.018	1.634 E+05	2.672 E+06	8.015 E+04	6.521
3.520	1.091 E+05	1.745 E+06	5.942 E+04	6.106
4.023	6.783 E+04	1.348 E+06	4.682 E+04	5.079
4.526	3.872 E+04	6.601 E+05	2.465 E+04	3.36
5.029	2.647 E+04	4.406 E+05	1.742 E+04	2.93

Figure 3.8 shows the varying flapwise bending stiffness values at different radial positions of inverse designed blade and the reference NREL blade and good match has been achieved. For the edgewise bending stiffness values close match could not be obtained. It should be noted that the inverse design methodology is based on matching required structural properties and to obtain ply orientation as close as possible. For this reason, exact match of the edgewise bending stiffness values are not mandatory. In addition, flapwise bending stiffness values are much more important to capture the bending deflection values accurately.

It should also be noted that for the reference NREL blade torsional stiffness values are not available. Therefore, in the present study the main aim was to match the flapwise bending stiffness to come with a blade which has more or less similar

flapwise bending stiffness as the NREL blade. With the inverse design approach, it is aimed to come up a 3-D blade design which has reasonable sectional blade properties which are not unrealistically high or low compared to the sectional beam properties of the NREL blade. 3-D blade design is then used to construct the finite element model of the blade to be used for the quasi-steady aeroelastic analysis of the blade only and the transient aeroelastic analysis of the complete wind turbine system in Samcef Wind Turbine (SWT) multi-body code.



**Figure 3.8** Comparison of the Variation of the Flapwise Bending Stiffness of the NREL Blade and the Inverse Design Blade

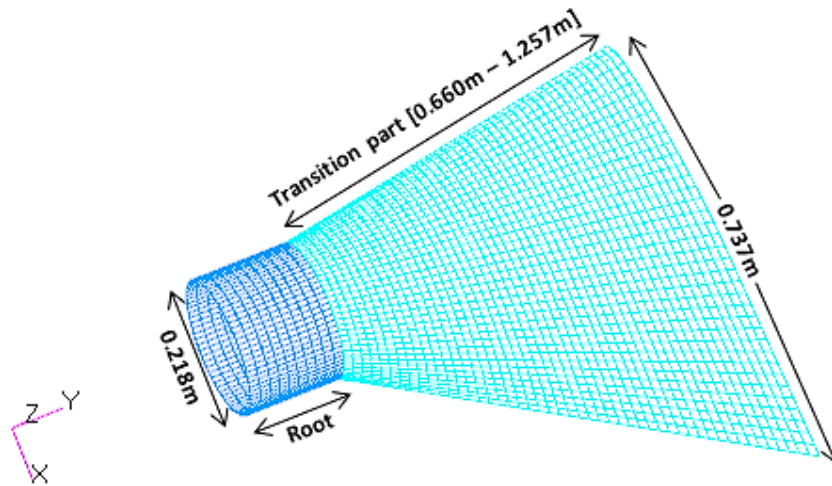
**Table 3.6** Sectional Ply Numbers and Thickness Variation

<b>Distance from Center (<i>m</i>)</b>	<b>Number of Plies D-Spar Cap</b>	<b>Thickness D-Spar Cap (mm)</b>	<b>Number of Plies Rear Part</b>	<b>Thickness Rear Part (mm)</b>
Root	24-UDCF	3.41376	-	-
1.257	20-UDCF	2.84480	-	-
1.509	18-UDCF	2.56032	12-EGWF	2.5908
2.012	16-UDCF	2.27584	10-EGWF	2.1590
2.515	15-UDCF	2.13360	10-EGWF	2.1590
3.018	14-UDCF	1.99136	9-EGWF	1.9431
3.520	14-UDCF	1.99136	8-EGWF	1.7272
4.023	12-UDCF	1.70688	8-EGWF	1.7272
4.526	10-UDCF	1.42240	6-EGWF	1.2954
5.029	10-UDCF	1.42240	6-EGWF	1.2954

### 3.4 Finite Element Modeling of the Wind Turbine Blade

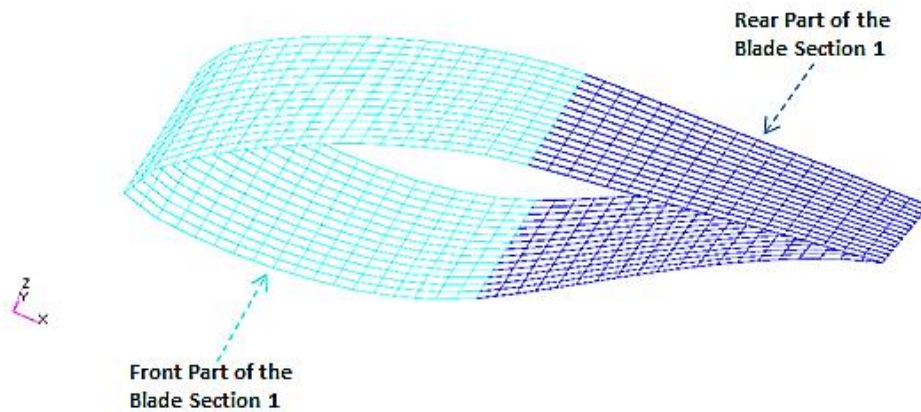
#### 3.4.1 Geometric Modeling

Based on the lay-up obtained in the inverse design phase utilizing VABS, main structural parts like skin and spars of the blade are modeled by using quadrilateral shell elements (QUAD4) in MSC®/PATRAN. Since the thicknesses of the blade skin and the spars are considerably small they are considered as thin walled structures and modeled by using 2-D elements. Initially, blade is separated into 10 discrete sections for finite element modeling. Root of the blade is modeled from the radial station at 508 mm to the radial station at 660 mm with a diameter of 218 mm, and then the transition part of the airfoil is completed from the end of the root part to the radial station at 1257 mm with a varying shape and diameter as illustrated in Figure 3.9.



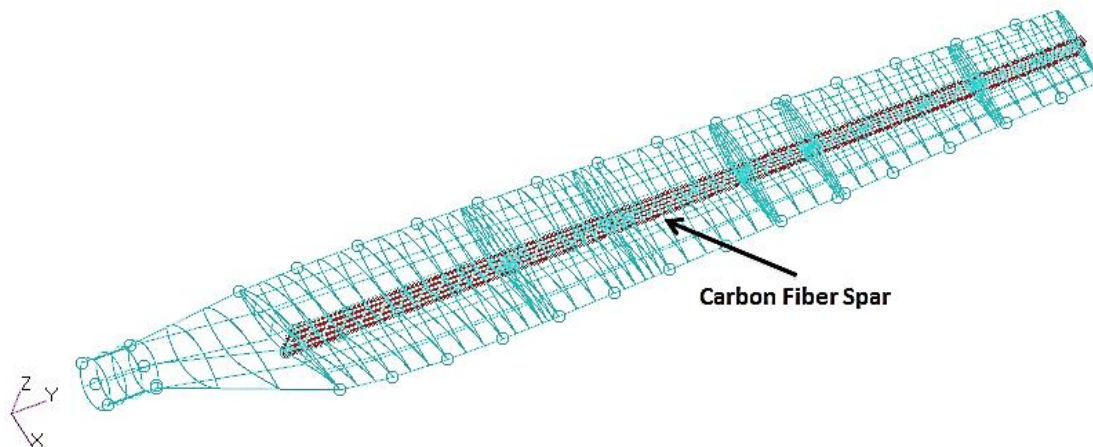
**Figure 3.9** Isometric View of the Skin Surfaces at the Root and the Transition Part of the Blade

The remaining 8 sections are detailed by generating the front and the rear parts of the blade sections, as shown in Figure 3.10. It should be noted that to facilitate the assignment process of the material properties to the related blade sections, blade sections are separated into 2 discrete parts.



**Figure 3.10** Cross-Sectional View of the Finite Element Mesh of the Front and Rear Part of the Skin of the Blade

Mostly, larger wind turbine blades have two spars, the front spar and the rear spar. However, in the present study, original NREL blade design is followed. NREL blade has only one spar to withstand the torsional and bending forces and it is located at 50% of the chord with no twist like the airfoil sections. Spar of the blade is modeled by using the 2-D elements from the end of the transition part to tip of the blade with a tapered thickness. Figure 3.11 shows the isometric view of the spar location of the blade.

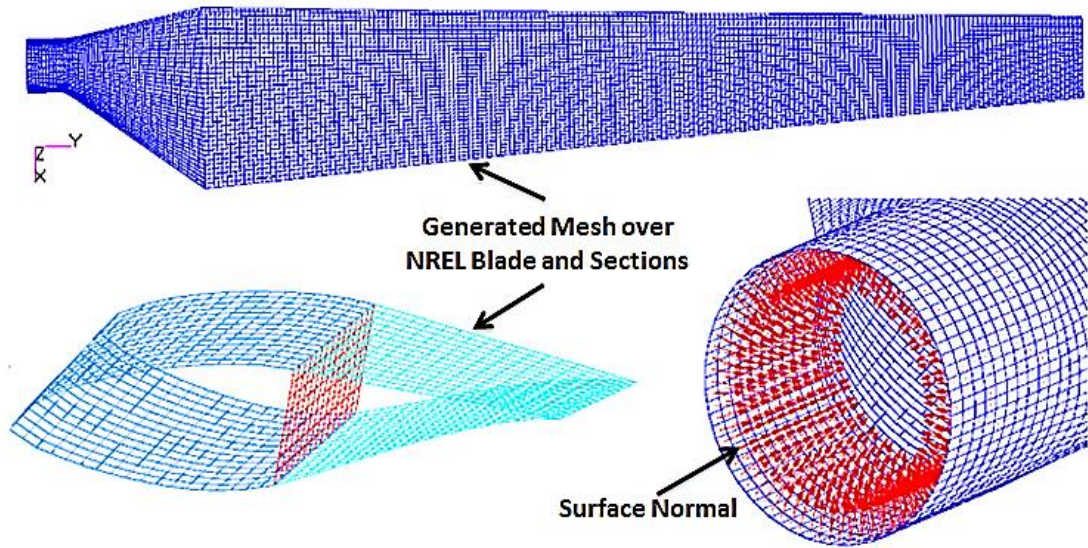


**Figure 3.11** Isometric View of the Spar Location of the Blade

### 3.4.2 Mesh Generation and Property Assignment

After completing the geometrical model, each part of the blade section is finely meshed by using Quad4 topology with the same global edge length in MSC®/PATRAN. Then, all nodes are equivalenced with a tolerance of “0.005” to eliminate duplicate nodes and create smooth links between the spar and the skin. In the next step, surface normals of the pressure and suction side skins of the blade are checked so as to verify that surface normals of the pressure and suction sides of the blade skin all point inward assuming that female skin molds would be used in the manufacturing of the skins of the blade. Figure 3.12 shows the finite element mesh of different parts of the blade.





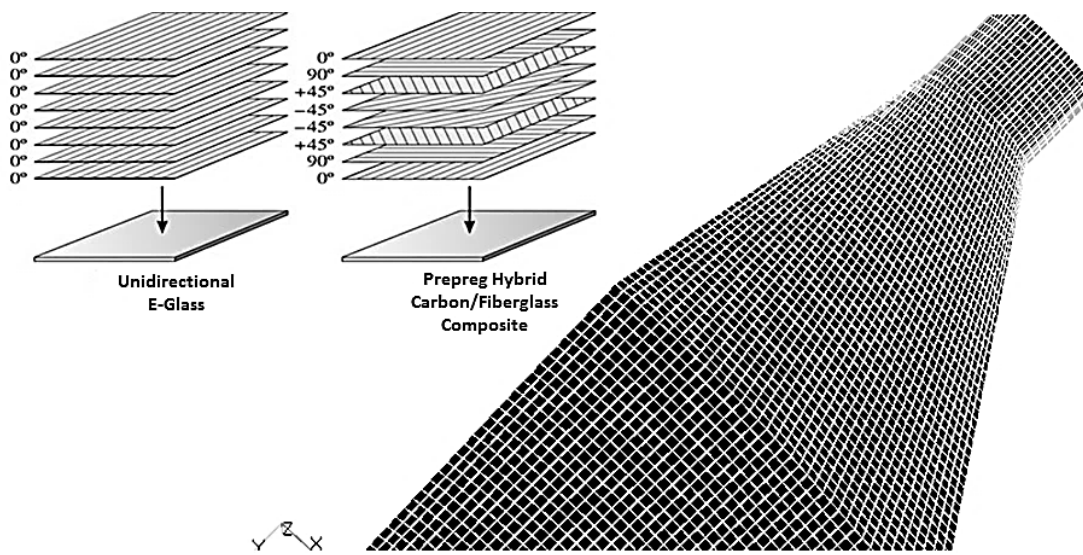
**Figure 3.12** Finite Element Mesh of the NREL Blade

Totally, 20536 elements and 20427 nodes are used to generate the finite element model. Element types and number of elements used in the geometric model are detailed in Table 3.7.

**Table 3.7** Number of Elements and Nodes Used in the Detailed Finite Element Model of the Inverse Design Blade

<b>Element Type: QUAD4 Shell</b>	<b>Number of Elements</b>	<b>Number of Nodes</b>
<b>Root</b>	760	836
<b>Transition</b>	3640	3724
<b>Skin</b>	14591	14067
<b>Spar</b>	1535	1800
<b>Total:</b>	20536	20427

Before the property assignment, 2-D orthotropic materials E-Glass and Hybrid Carbon/Fiberglass are defined. As shown in Figure 3.13, composite laminates that are assigned to blade sections are created with an exact match of the orientation angle of each ply as defined in the PreVABS input file.



**Figure 3.13** Fiber Orientation and Material Assignment

As it was mentioned before, because of the lack of information about the complete material layout used in the reference NREL blade, appropriate mass densities to the materials in each blade section are assigned such that sectional mass densities of the inverse design blade match the sectional blade mass densities of the NREL blade. After subjective tuning and matching the desired sectional properties of the inverse design blade with the NREL blade, total mass of the blade is calculated as 60.19 kg where the original blade weighs 60.25 kg [15].

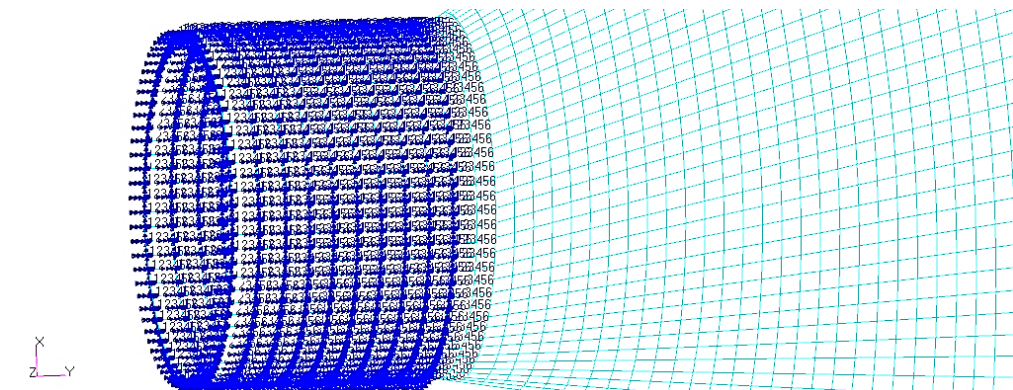
**Table 3.8** Summary of Center of Gravity, Principal Inertias, Radii of Gyration, Mass and Volume of the Inverse Design Blade

<b>C.G (mm)</b> <b>[x, y, z]</b>	<b>I-Principal</b> <b>(gr. mm<sup>2</sup>)</b>	<b>Radii of Gyr.</b> <b>(mm)</b>	<b>Mass</b> <b>(kg)</b>	<b>Volume</b> <b>(mm<sup>3</sup>)</b>
1.116E+002	8.279E+007	1.173E+003		
2.390E+003	8.127E+007	1.162E+003	6.019E+001	1.140E+007
1.730E+001	1.830E+006	1.744E+002		

Table 3.8 gives the summary of the center of gravity (CG), the principal inertias at the CG, the radii of gyration corresponding to the principal inertias at the CG, mass and volume of the inverse designed blade. To calculate the mass properties tabulated above, shell thicknesses, cross-sectional areas concentrated mass values and densities are used and the units are consistent with element properties, and material properties.

### 3.4.3 Application of the Boundary Conditions and Modal Analysis

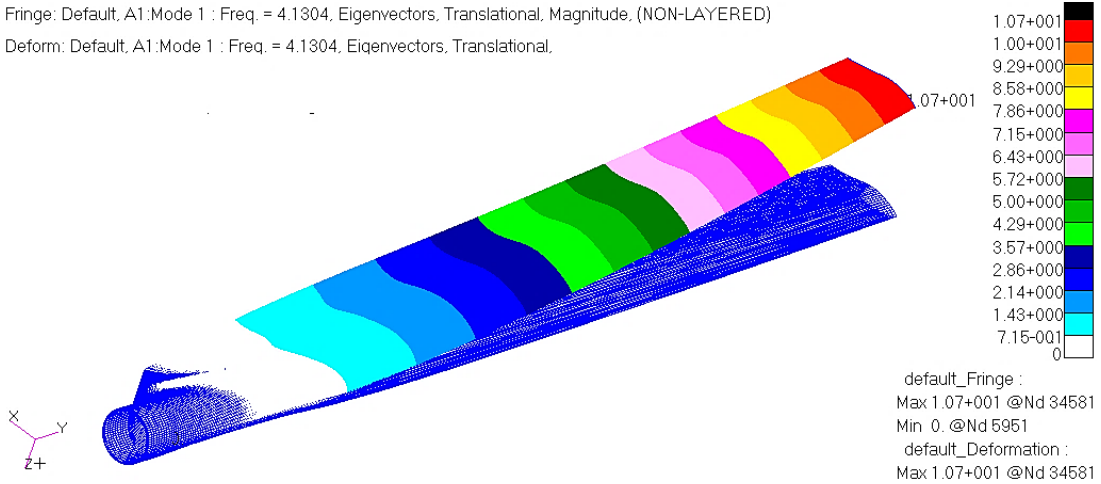
The modal analysis of the inverse designed blade is performed by using solution type, Normal Mode Analysis (Solution 103) in MSC®/NASTRAN. Before conducting the analysis, all six degrees of freedom of the root nodes are fixed to satisfy the required conditions as illustrated in detail in Figure 3.14. Before running the modal analysis, weight conversion unit is set to 0.001 because geometric blade modeling unit is done in millimeters.



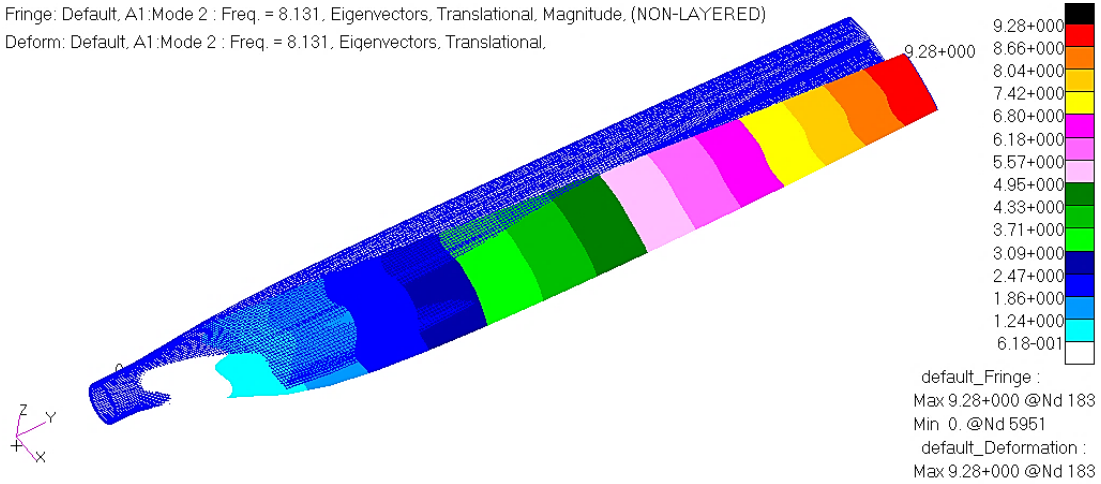
**Figure 3.14** Zoomed View of Fixed Root Nodes in MSC®/PATRAN

First and second flapwise bending mode shapes, first edgewise bending mode shape and torsional mode shape are presented in Figure 3.15 - Figure 3.18. Global mode shape results are also tabulated in Table 3.9. In order to make reliable comparison of the quasi-steady aeroelastic analysis results that are obtained in MSC®/NASTRAN with the results of the transient aeroelastic analysis of the wind turbine system that

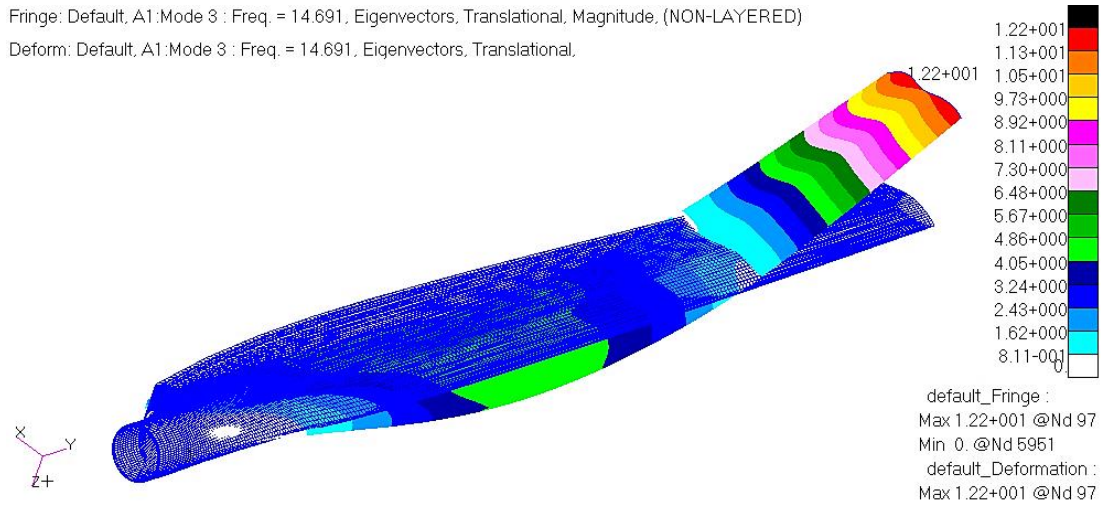
are obtained in SWT, first few global mode shapes of the blade that is used in the quasi-steady aeroelastic analysis should be matched with the first few global mode shapes of the blade that is used in the transient multi-body dynamic analysis. It should be noted that the multi-body dynamic model of the wind turbine which is used in the transient aeroelastic analysis of the blade is presented in the next chapter.



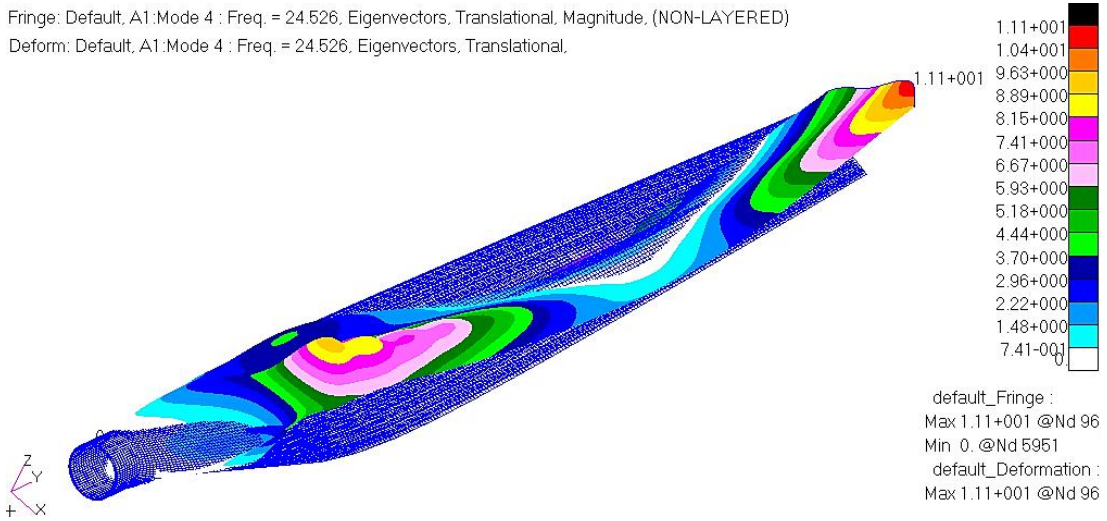
**Figure 3.15** 1<sup>st</sup> Flapwise Bending Mode Shape of the Inverse Design Blade  
 [4.13 Hz]



**Figure 3.16** 1<sup>st</sup> Edgewise Bending Mode Shape of Inverse Design Blade  
 [8.13 Hz]



**Figure 3.17** 2<sup>nd</sup> Flapwise Bending Mode Shape of the Inverse Design Blade  
 [14.69 Hz]



**Figure 3.18** Torsional Mode Shape of the Inverse Design Blade  
 [24.52 Hz]

**Table 3.9** Global Mode Shapes and Natural Frequency Results of the Inverse Design Blade

<b>Global Mode Shapes</b>	<b>Natural Frequency Value [Hz]</b>
1 <sup>st</sup> Flapwise Bending	4.13 Hz
1 <sup>st</sup> Edgewise Bending	8.13 Hz
2 <sup>nd</sup> Flapwise Bending	14.69 Hz
Torsional	24.52 Hz

### 3.5 Quasi-steady Aeroelastic Analysis

Quasi-steady aeroelastic analysis methodology is based on the coupling of an aerodynamic model and structural finite element model. During the coupling procedure, BEM based aerodynamic model provides the distributed loads over the blade and structural model takes the distributed loads obtained from the aerodynamic model as input and gravitational forces are superimposed on top of the aerodynamic loads in order to analyze the blade deformation. The coupling of the aerodynamic model and the structural finite element model progresses such that spanwisely distributed loads create structural deformation which in turn causes an incremental change in the aerodynamic loads. In the quasi-steady aeroelastic analysis, this iterative process is repeated in a loosely coupled fashion until the blade deformation converges to some value within a prescribed tolerance. The detailed algorithm of the coupling procedure is introduced in Figure 3.19. In the loosely coupled approach, BEM code is utilized to perform the aerodynamic analysis. In the BEM processing, induction factors are estimated and according to known geometry, the inflow angles and corresponding lift, drag, and thrust are calculated for each section.

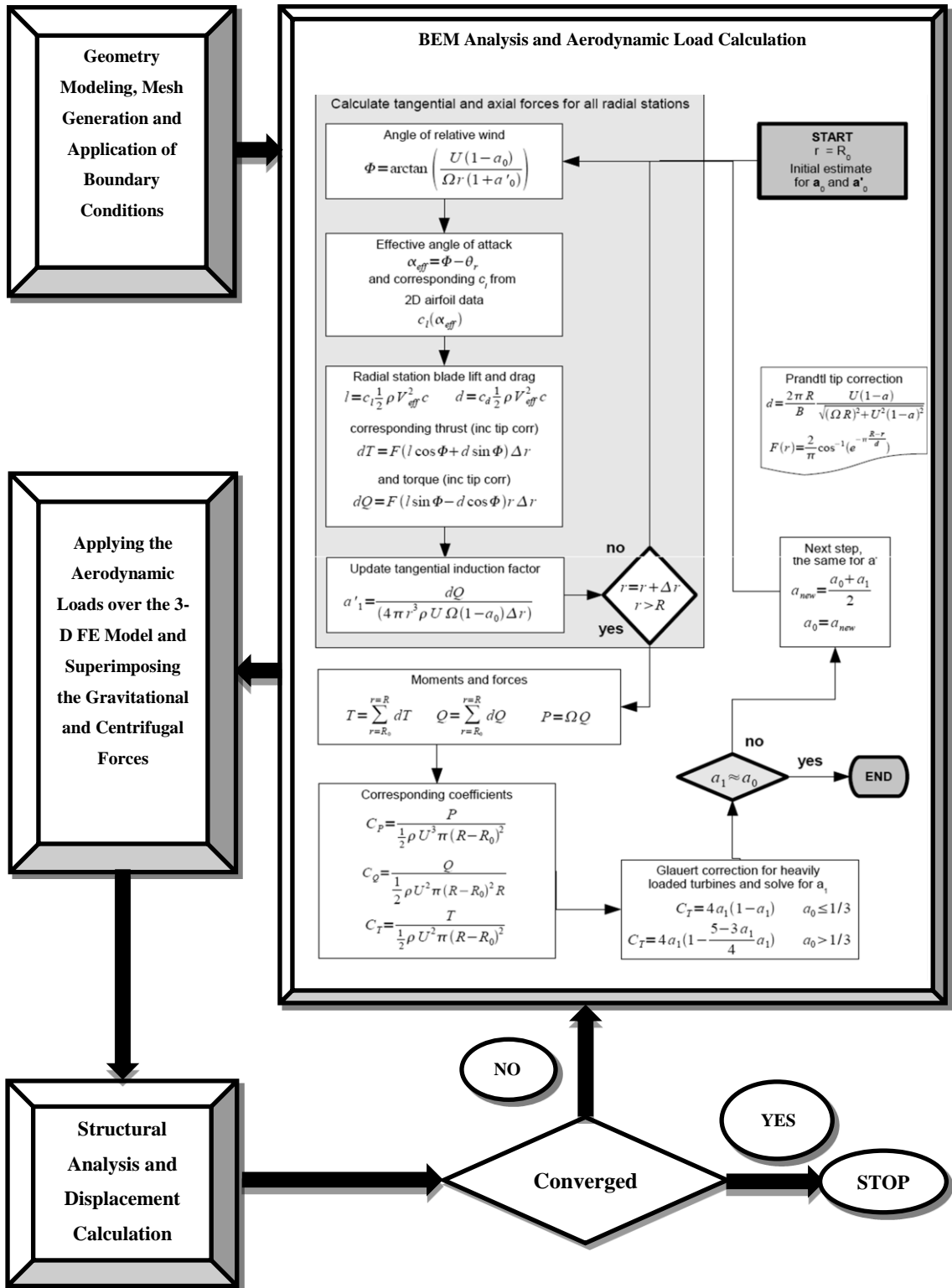
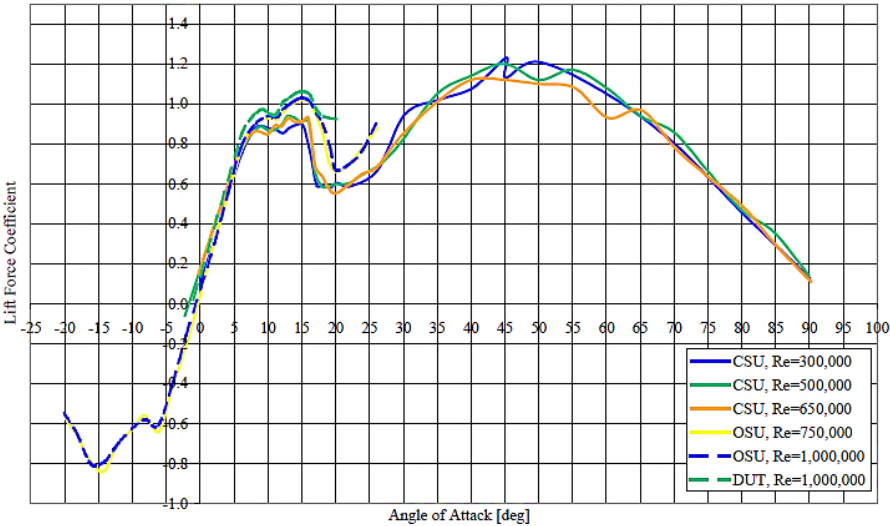


Figure 3.19 Flow Chart of the Coupling Procedure [43]



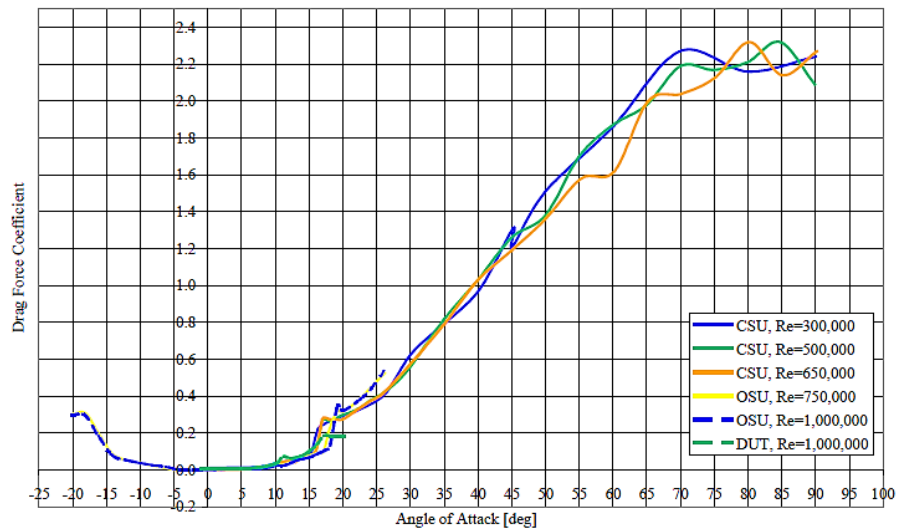
Regarding the calculations, inductions factors are updated and iterative process continues until a balanced response is reached within a prescribed tolerance. In the next step, finite element model is coupled with the BEM results by applying the 2-D aerodynamic lift, drag and moment on the aerodynamic center of the airfoil profile in the structural model. Under the action of the aerodynamic loads, finite element model deforms and hence, inflow angle and corresponding lift, drag, thrust and torque for each section change incrementally. Incremental changes of the aerodynamic forces, in turn, cause incremental changes in the structural deformation of the blade. Therefore, this coupling process is repeated until convergence is achieved based on a prescribed convergence criterion.

It should be noted that to perform the conventional algorithm for the BEM analysis and aerodynamic calculation lift, drag and moment coefficients of the airfoil are needed. Aerodynamic coefficients can be obtained from wind tunnel tests or computational fluid dynamic (CFD) methods. In this study, for the NREL S809 airfoil, aerodynamic coefficients obtained from the wind tunnel tests conducted by the Ohio State University (OSU) at  $Re=750,000$  are used [41]. Figure 3.20 and Figure 3.21 show the lift and the drag coefficient of the airfoil for varying different Reynolds numbers.



**Figure 3.20** Lift Force Coefficient Data of the NREL S809 Airfoil [41]





**Figure 3.21** Drag Force Coefficient Data of NREL S809 Airfoil [41]

However, as it can be seen from the Figure 3.20 and Figure 3.21, the deep stall effects are missing in wind tunnel test results. For this reason aerodynamic data at high angle of attack are extrapolated by using NTWC design code “FoilCheck” [54] which runs the Viterna-Corrigan equations for post stall process [41]. Figure 3.22 is obtained after the airfoil data extrapolation from a limited range of angles to the entire extended range and the results are used in the aerodynamic calculations. The detailed aerodynamic lift, drag and moment coefficients are presented in APPENDIX C.

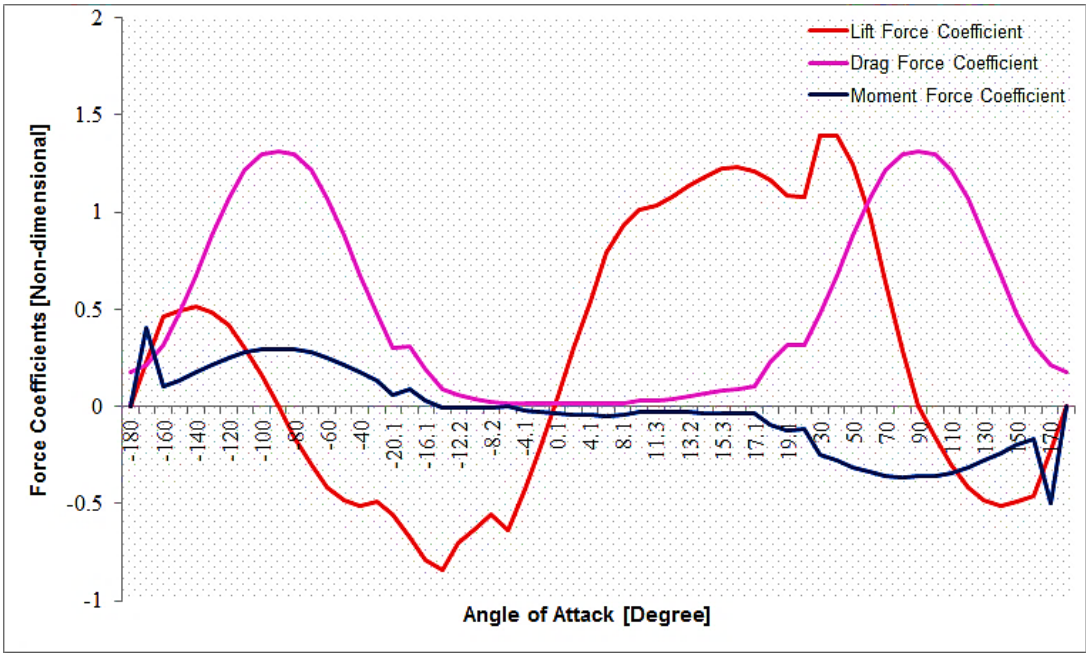
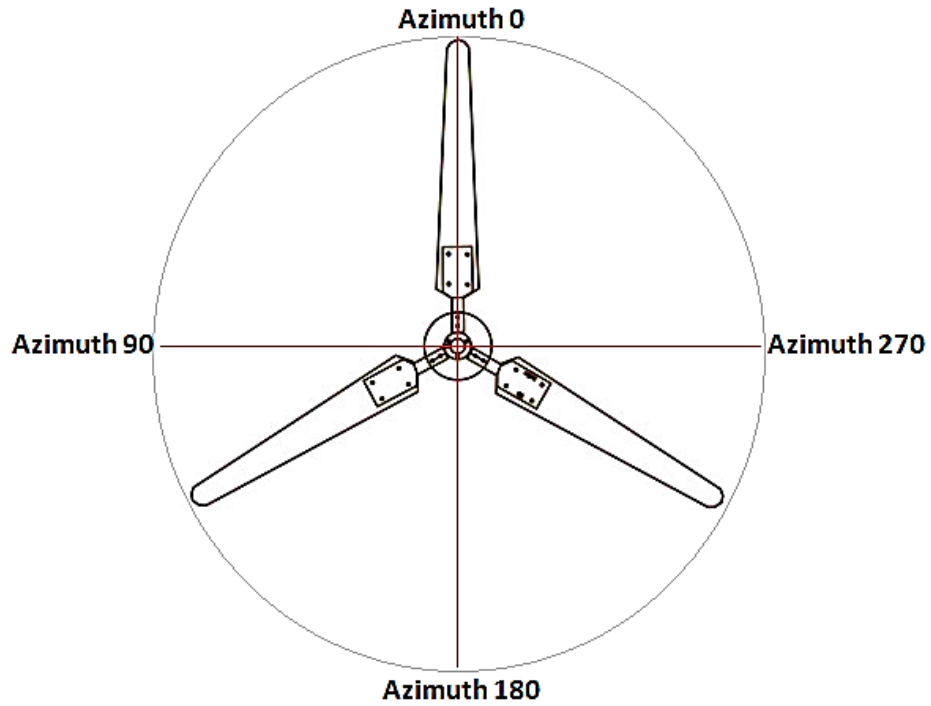


Figure 3.22 NREL S809 Airfoil – Extrapolated Aerodynamic Force Coefficients

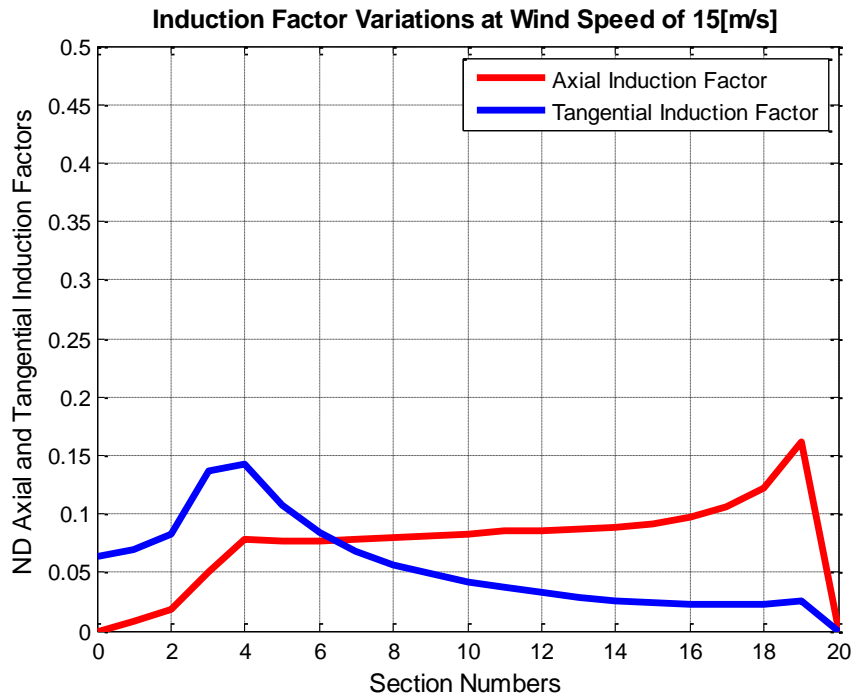
**3.5.1 Results of Quasi-steady Aeroelastic Analysis for Concentrated Load Cases**

Initial aerodynamic loads are computed by following up the algorithm given in Figure 3.19 for different wind conditions. However, only the results for the steady wind speed 15 m/s with a wind shear exponent of 0.2 are presented in this study. To verify that induction factors are within the prescribed tolerance, 30 iterations have been performed for each blade element and to speed up the induction factor estimation process, a wind turbine performance predictor tool, WT\_Perf [53] which is developed by National Wind Technology Center (NTWC) is used. The program is written in FORTRAN 95 language, and it is designed to perform measurements for angle of attack values ranging from 0 degrees to  $\pm 180$  degrees. Azimuthal representation of the wind turbine blades are illustrated in Figure 3.23.



**Figure 3.23** Azimuth Positions of the NREL Blade

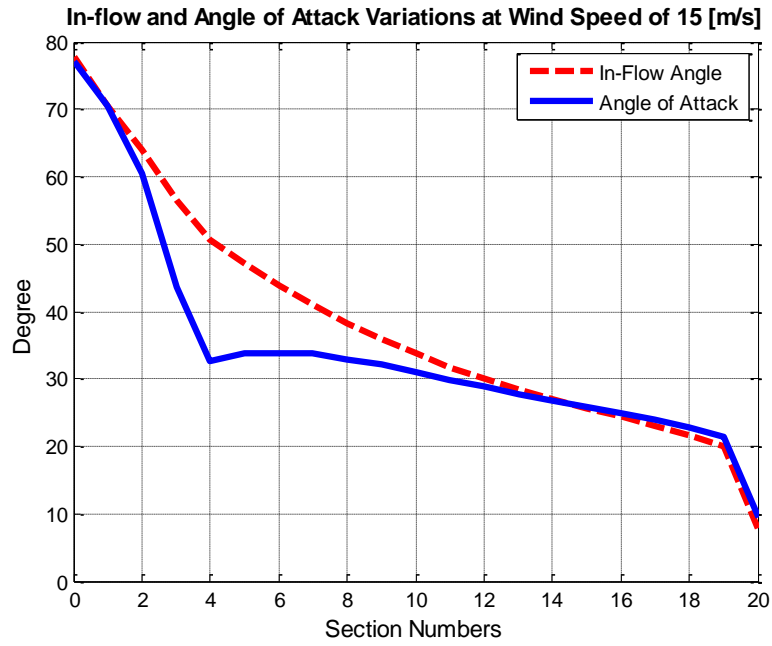
To run the BEM analysis in WT\_Perf, an input file which includes wind turbine model configuration, algorithm configuration, turbine data and geometrical data of NREL blade is prepared as shown in APPENDIX B - Part A in detail. Moreover, Prandtl's tip-loss, hub-loss models and swirl effects are enabled in the input file and these input files are coupled with the 2-D airfoil aerodynamic data by utilizing the WT\_Perf program and some of the results obtained by WT\_Perf are shown in Figure 3.24 and Figure 3.25 .



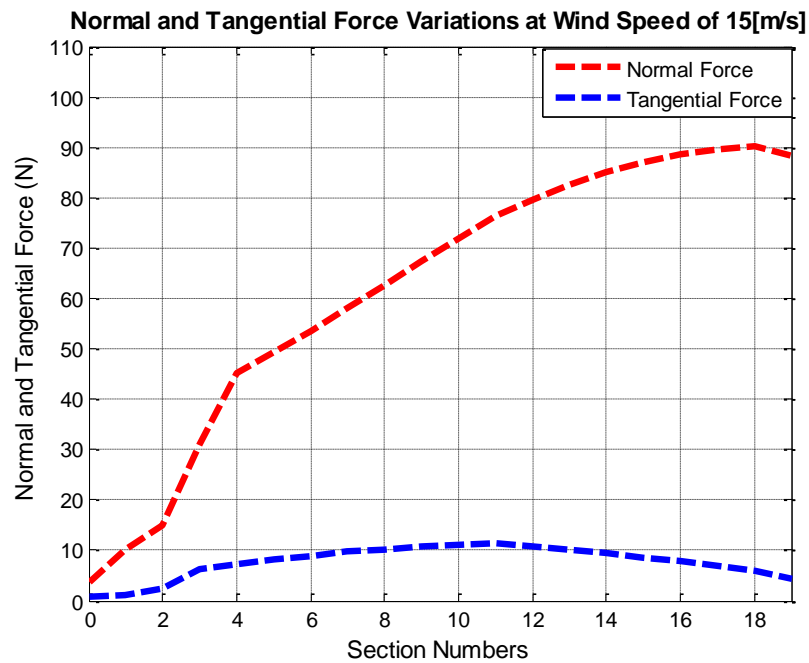
**Figure 3.24** Axial and Tangential Induction Factor Variations of NREL S809

Figure 3.24 shows the extracted axial and tangential induction factors. As it can be seen that tangential induction factor decreases gradually and at the tip it is equal to 0 which is an expected result because of the Prandtl's tip loss correction.

In the next step, induction factors determined, inflow velocities, angle of attacks and aerodynamic coefficients at each section are used to compute the lift, drag and moment forces (Eqn. (2.14) – Eqn. (2.16)). Figure 3.25 shows the in-flow angle and angle of attack variations of the NREL S809 blade calculated by WT\_Perf. Finally, by applying Eqn. (2.24) and Eqn. (2.25) tangential and normal forces are calculated for 20 sections, as shown in Figure 3.26.

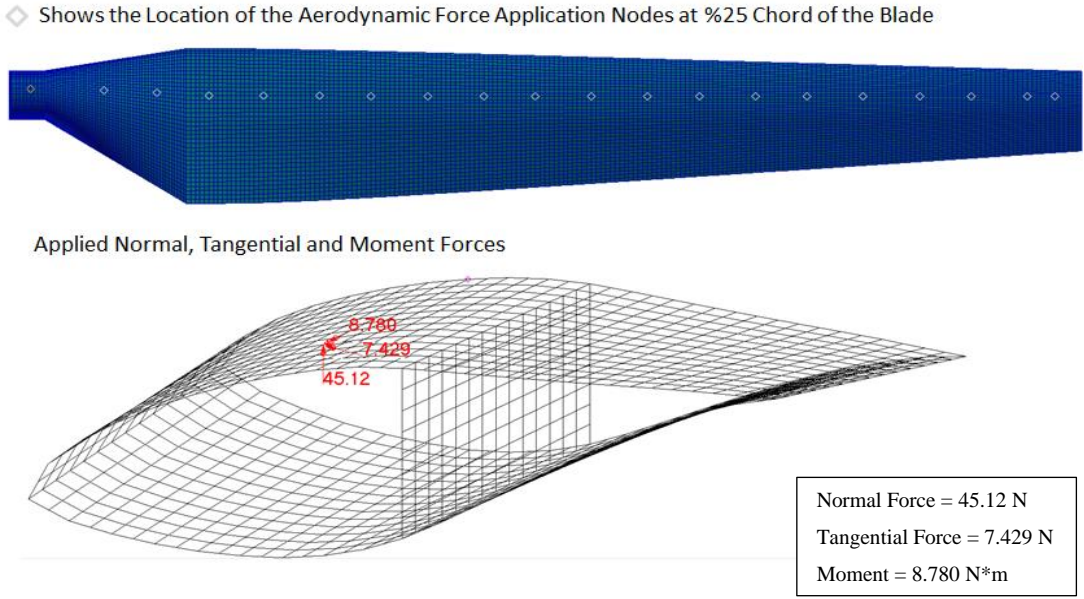


**Figure 3.25** In-flow Angle and Angle of Attack Variations of the NREL S809 Blade  
- Azimuth 0



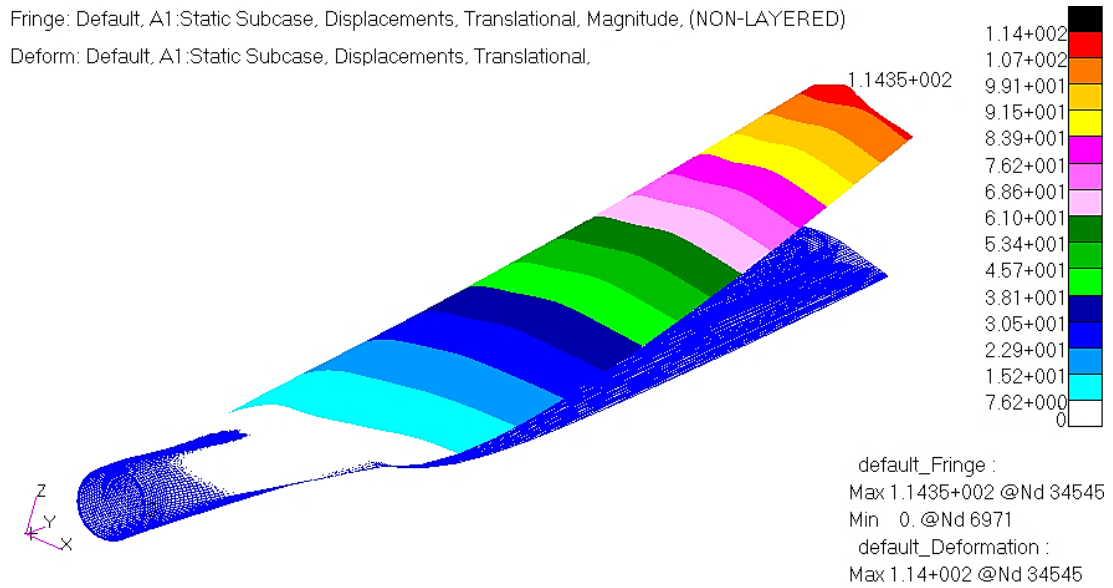
**Figure 3.26** Normal and Tangential Force Variations of NREL S809 Airfoil –  
Azimuth 0

To distribute the calculated normal, tangential force and moment forces over the blade, 20 nodes are defined at %25 chord of the blade measured from the leading edge of the blade and circular root sections. Then, the forces normal and tangential to the global coordinate lines and moments are placed on the defined nodes at the upper layer of the blade as shown in Figure 3.27.



**Figure 3.27** Location of Aerodynamic Force Application Nodes and Loads Applied to the Inverse Design Blade for Flapwise Deflection Calculation

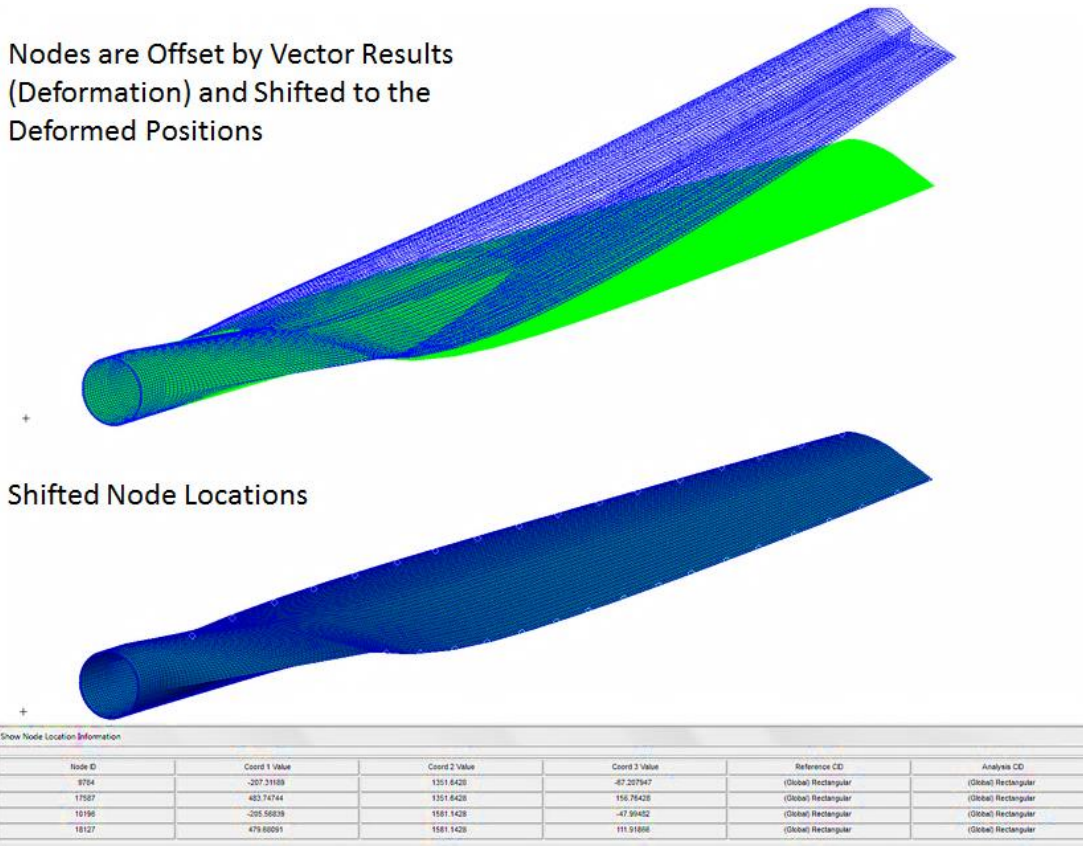
After all the loads are applied over the finite element model of the NREL blade, static analysis is conducted by using the solution sequence 101 of MSC®/NASTRAN to calculate the flapwise deflection at the tip of the blade. As a result of static analysis, displacement at the tip of the blade is obtained as 114.35 mm for the 1<sup>st</sup> Iteration as shown in Figure 3.28.



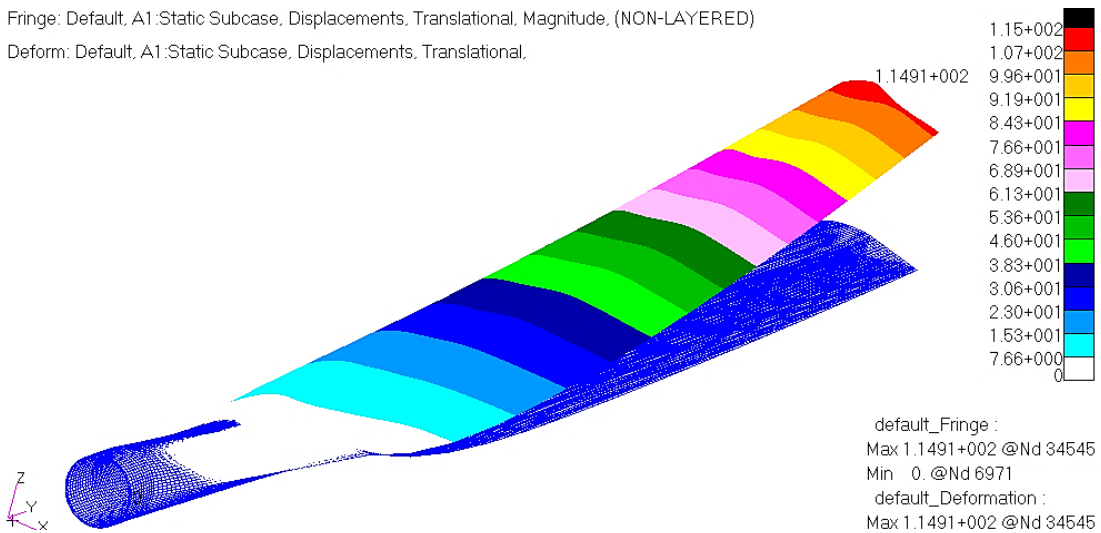
**Figure 3.28** Blade Deflection at 72 rpm and 15m/s Wind Speed – After the 1<sup>st</sup> Iteration

After the 1<sup>st</sup> deformation, inflow angle and corresponding aerodynamic loads and moments are re-calculated for each section. Incremental changes in the aerodynamic loads are computed by utilizing the “*shifting nodes*” feature of MSC®/PATRAN. As illustrated in Figure 3.29, all node locations are shifted to the deformed positions. After the shifting of the nodes, new positions of the node locations at the leading and trailing edges are recorded. These recorded locations are compared with the non-deformed node location data and by using the simple trigonometric formulas, differences in the inflow angle and twist angle are computed. Inflow angle and twist values are added to the initial ones and all the aerodynamic loads are re-computed utilizing the newly calculated inflow angle and twist values by performing BEM analysis at WT\_Perf tool. This coupling process is repeated until convergence is achieved based on a prescribed convergence criterion which is decided as the 0.01 mm for the difference of tip deflection results between the iterations. Figure 3.30 and Figure 3.31 show the 2<sup>nd</sup> and 3<sup>rd</sup> displacement field of the wind turbine blade for Azimuth 0 – Vertical up position of the blade.

Nodes are Offset by Vector Results  
(Deformation) and Shifted to the  
Deformed Positions

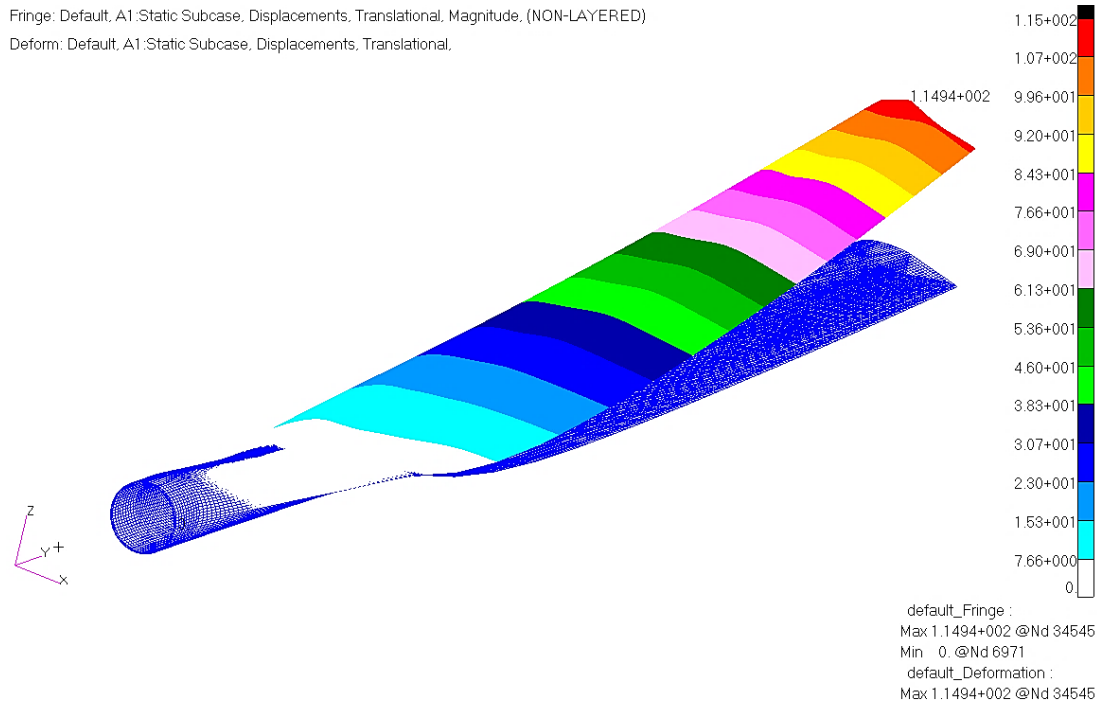


**Figure 3.29** Deformed Blade and Shifted Node Locations



**Figure 3.30** Blade Deflection at 72 rpm and 15m/s Wind Speed – After the 2<sup>nd</sup> Iteration





**Figure 3.31** Blade Deflection at 72 rpm and 15m/s Wind Speed – After the 3<sup>rd</sup> Iteration

In the quasi-steady aeroelastic analysis of the wind turbine blade, 4 iterations have been performed for the 15 m/s steady wind speed with a wind shear exponent of 0.2 and for the azimuthal position of 0 degree which refers to the vertical up position. Ignoring the transient effects due to the rotation, the deflection plots of the blade are plotted. From Figure 3.28 - Figure 3.31, it can be seen that tip deflections are obtained as 114.35 mm, 114.91 mm and 114.94 mm for the first three iterations. At end of the 4<sup>th</sup> iteration, convergence is achieved and same maximum tip deflection value is obtained. For the other azimuthal positions, exactly same procedure is followed and the results are tabulated in Table 3.10

**Table 3.10** Results of Quasi-steady Aeroelastic Analysis for Concentrated Loads

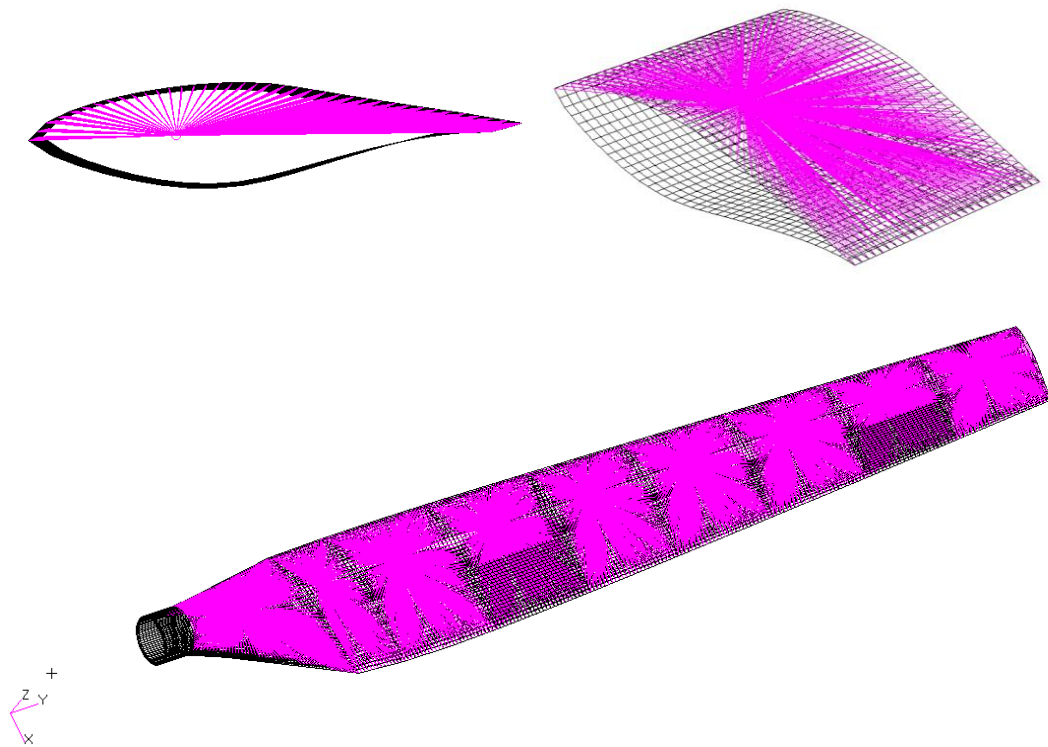
<b># of Iterations</b>	<b>Tip Displacement Azimuth 0 (mm)</b>	<b>Tip Displacement Azimuth 90 (mm)</b>	<b>Tip Displacement Azimuth 180 (mm)</b>	<b>Tip Displacement Azimuth 270 (mm)</b>
1 <sup>st</sup> Iteration	114.35	109.60	104.38	109.60
2 <sup>nd</sup> Iteration	114.91	110.61	105.04	110.61
3 <sup>rd</sup> Iteration	114.94	110.69	105.15	110.69
4 <sup>th</sup> Iteration	114.94	110.69	105.15	110.69

### 3.5.2 Results of Quasi-steady Aeroelastic Analysis for Distributed Load Cases

In the second part of the quasi-steady aeroelastic analysis, similar procedure has been followed to calculate the aerodynamic loads. As a difference from the initial study, turbine model is divided into 10 discrete sections in WT\_Perf as detailed in APPENDIX - Part B to achieve a close match with the aerodynamic model of the transient aeroelastic analysis. After obtaining the induction factors normal, tangential forces and aerodynamic moments are calculated and applied on a node at the center of the each section and at the %25 chord line of the airfoil.

Concentrated aerodynamic forces acting at the aerodynamic center of blade sections are distributed to the suction side nodes of the finite element model by means of multi-point constraint element RBE3 that is available in MSC®/NASTRAN. RBE3 element defines a constraint relation in which the motion at a reference grid point is the least square weighted average of the motions at other grid points. Forces and moments applied to reference points are distributed to a set of independent degrees of freedom based on the RBE3 geometry and local weight factors. The manner in which the forces are distributed is analogous to the classical bolt pattern analysis. The force and moment is transferred directly to the weighted center of gravity location along with the moment produced by the force offset. The force is distributed to the bolts

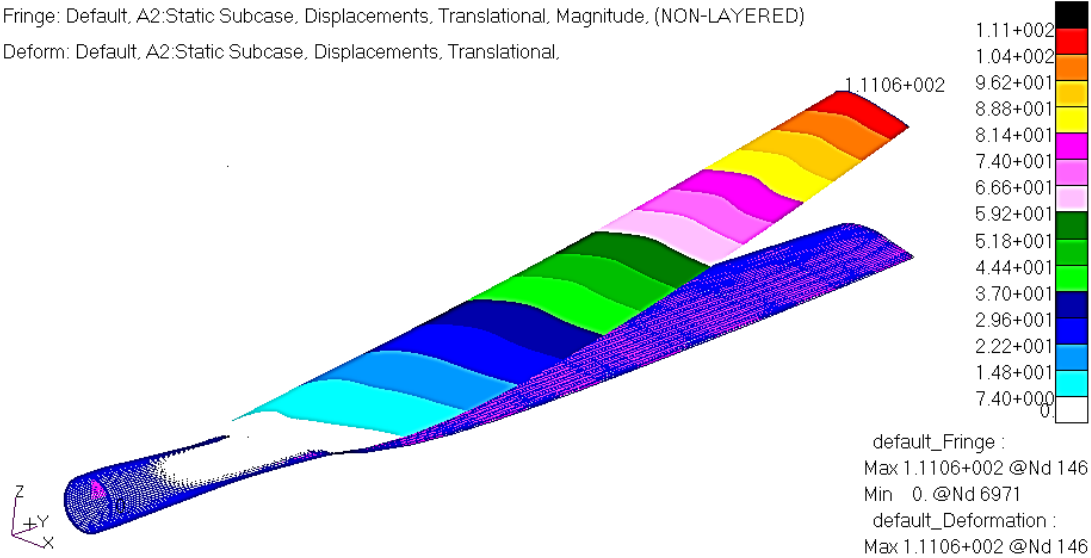
proportional to the weighting factors. The moment is distributed as forces, which are proportional to their distance from the center of gravity times their weighting factors. For the distribution of the forces applied at the aerodynamic center, weight factors are taken as 1 since nodes represent same size bolts. For this purpose, the nodes created at the aerodynamic center of the blade sections are defined as the dependent node and all six degrees of freedom are defined. The nodes in the suction side of the blade sections are selected as the independent nodes and just translational degrees of freedom are selected. Figure 3.32 shows the distribution of aerodynamic forces applied at the aerodynamic center to suction side nodes by RBE3 elements.



**Figure 3.32** RBE3 Elements and Distribution of the Aerodynamic Loads Applied at the Aerodynamic Center to Upper Section Nodes

Once the coupling between finite element model and aerodynamic forces which are calculated by WT\_Perf at the aerodynamic center of each blade is completed, static

analysis is conducted as described previously. For azimuth 0 degree, after the 1<sup>st</sup> iteration, the maximum displacement is obtained as 111.06 mm at the tip of the blade as shown in Figure 3.33.



**Figure 3.33** Flapwise Deflection at 72 rpm and 15m/s Wind Speed – After the 1<sup>st</sup> Iteration

Again by following the same procedure as detailed in the concentrated load case, after the 1<sup>st</sup> deformation, incremental changes in angle of attack values are computed for each azimuth location and corresponding aerodynamic loads and moments are re-calculated for each blade section. As an example, for azimuth 90 degrees, Table 3.11 gives the incremental changes in angle of attack values with the iteration number at each blade element. The first blade element corresponds to the circular root where there is no lift. From Table 3.11, it is seen that in three iterations incremental changes in the angle of attack values become almost negligible. The fourth iteration essentially gives the same deformation of the blade as the third iteration.

**Table 3.11** Incremental Changes in Angle of Attack Values with the Iteration  
Numbers (Azimuthal Position - 90 Degree)

<b>Blade Element</b>	<b>1<sup>st</sup> iteration (Deg.)</b>	<b>2<sup>nd</sup> iteration (Deg.)</b>	<b>3<sup>rd</sup> iteration (Deg.)</b>
<b>2</b>	-0.0222	-0.0150	-0.00003
<b>3</b>	-0.2715	-0.0129	-0.00021
<b>4</b>	-0.3396	-0.0068	-0.00025
<b>5</b>	-0.4030	-0.0086	-0.00030
<b>6</b>	-0.4219	-0.0011	-0.00031
<b>7</b>	-0.4374	0.0038	-0.00031
<b>8</b>	-0.4290	0.0052	-0.00031
<b>9</b>	-0.4628	0.0046	-0.00034
<b>10</b>	-0.4384	0.0065	-0.00029

Table 3.12 gives the maximum tip displacements obtained as a result of quasi-aeroelastic analysis at three different azimuthal locations.

**Table 3.12** Results of Quasi-steady Aeroelastic Analysis for Distributed Loads

<b># of Iterations</b>	<b>Tip Displacement Azimuth 0 (mm)</b>	<b>Tip Displacement Azimuth 90 (mm)</b>	<b>Tip Displacement Azimuth 180 (mm)</b>	<b>Tip Displacement Azimuth 270 (mm)</b>
1 <sup>st</sup> Iteration	111,06	102,82	99,95	102,82
2 <sup>nd</sup> Iteration	112,14	103,52	100,14	103,52
3 <sup>rd</sup> Iteration	112,22	103,61	100,38	103,61
4 <sup>th</sup> Iteration	112,22	103,61	100,38	103,61

From the results presented in Table 3.10 and Table 3.12, it is seen that the change in the maximum tip displacement is very small in each iteration. This is an indication that the inverse design blade structure is actually very rigid. However, the whole process of quasi-steady aeroelastic analysis would not change if the blade structure was more flexible. It should be noted that present analysis only deals with linear structures. Material and geometric non-linearity is not considered. In general, material non-linearity is not a concern in wind turbine blades. But, geometric non-linearity associated with the large deflections and rotations can be important for long

and flexible blade structures. For very flexible blade structure, quasi-steady aeroelastic analysis could still be performed if geometrically non-linear solver MSC®/NASTRAN (Sol 106) is used as the structural solver instead of linear solver Sol 101. It is also noted that for the distributed load case, maximum tip displacements are less than the maximum tip displacements obtained by the concentrated load case.

In Chapter 4, comparisons are made with the deflection results of the transient aeroelastic analysis of the wind turbine system which is performed in Samcef Wind Turbine.

## CHAPTER 4

### MULTI-BODY MODELING of the REFERENCE TURBINE AND TRANSIENT AEROELASTIC ANALYSIS OF THE BLADE

In the design of wind turbine blades, for accurate load analysis, complete turbine model has to be built in a multi-body framework and transient aeroelastic analysis of the wind turbine system which includes major components such as turbine blades, rotor hub and rotor shaft, gearbox, generator and tower has to be performed. Building the multi-body model of the complete wind turbine requires specialized software and detailed information about the major components which build-up the turbine system. For this purpose, a multi-body dynamic code “*Samcef Wind Turbine (SWT)*” [55] is utilized for performing the transient aeroelastic analysis of the blade. “*Samcef Wind Turbine*” integrates the aerodynamic, structural and control features of the wind turbine in a fully dynamic environment. Aerodynamic solver of SWT is based on BEM theory with typical corrections such as tip and hub losses, tower shadow, and deactivation of induction factors at low tip speed ratios. SWT also has built-in semi-empirical sub-models to treat unsteady aerodynamics with higher accuracy. Specifically, SWT has dynamic wake sub-model, skewed flow correction sub-model and dynamic stall sub-models which are of Beddoes-Leishman type. The controller is integrated to the wind turbine model by means of dynamic link library which can be used for typical wind turbine simulations. Multi-body simulation of the wind turbine system is performed by the implicit non-linear finite element solver Samcef Mecano [56] which has the ability to allow the use of multi-body simulation features, such as kinematic joints etc., inside real finite elements models. Transient simulations are performed in time domain taking into account the structural, multi-body, aerodynamic and control features in a fully non-linear dynamic way with strong

coupling. The main non-linear features are present in the aerodynamics, in the controller, and in structural and multi-body elements such as non-linear stiffness, large rotations, bearing gaps etc. [55].

In the present study, to conduct the multi-body dynamic analysis of the wind turbine system, firstly, dynamic superelement of the turbine blade has to be created in the Samcef Field [16] environment since Samcef Wind Turbine recognizes the format of the superelement generated by Samcef Field. Dynamic superelement of the blade is then introduced into the multi-body model of the wind turbine system, and transient aeroelastic analysis is performed in steady wind conditions. Before the generation of the dynamic superelement of the blade, three dimensional finite element model of the blade is created in Samcef Field in a similar manner to the creation of the finite element model in MSC®/PATRAN that is described before. It should be noted that in order to reflect the stiffness and mass properties of the blade, that is generated in two different finite element programs MSC®/NASTRAN-PATRAN and Samcef Field, accurately, three dimensional finite element model of the blade is used rather than the beam model. Another reason for the choice of the three dimensional finite element model of the blade is that neither MSC®/NASTRAN nor SWT have beam formulation that is suitable for modeling composite blades with coupling coefficients. On the other hand, three dimensional finite element models are too costly to be used in the multi-body simulation of the complete wind turbine system. Therefore, in SWT superelement of the blade is used for the multi-body simulation of the wind turbine system.

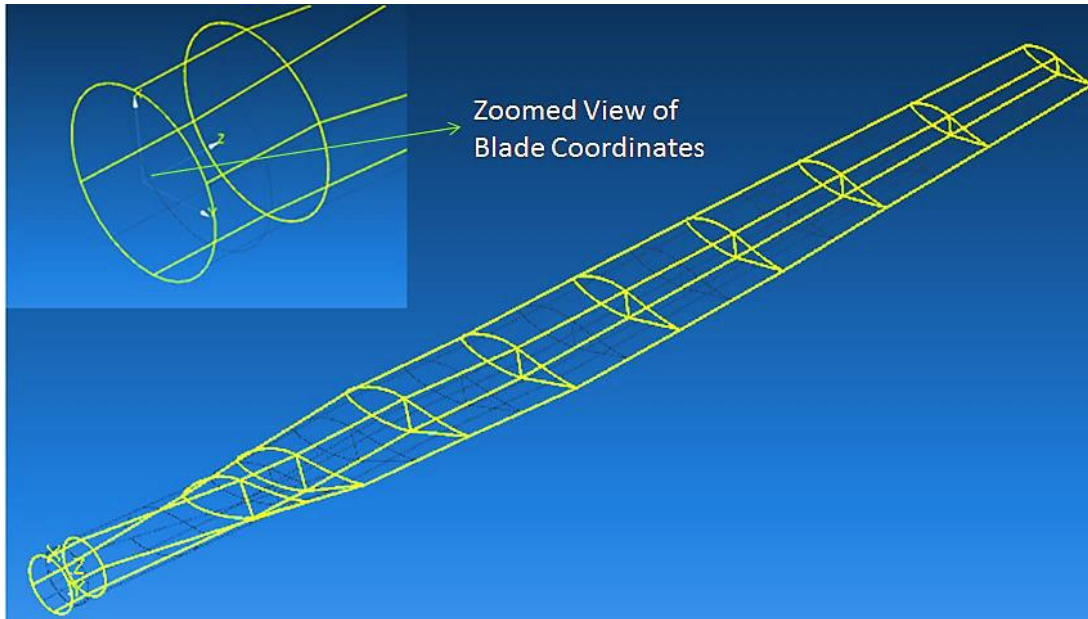
#### **4.1 Generation of Superelement Blade**

In the present study, transient aeroelastic response of the turbine blade is investigated by the multi-body simulation of the reference wind turbine system. Superelement of the wind turbine blade, which is completed through the inverse design process described previously, is created in Samcef Field [16] and introduced into the multi-



body model of the wind turbine system which is generated in Samcef Wind Turbine Dynamic superelement used in the present study is non-linear superelement which is based on the Craig and Bampton component mode method [57]. Non-linearities arise from the fact that formulation of the superelement allows modeling of the blade structure undergoing large displacements and rotations in space, with the only limitation that with respect to the local frame fixed to the blade, blade behaves geometrically linear. The main advantage of using the dynamic superelement of the blade in the multi-body dynamic model of the wind turbine system is to allow the detailed modeling of components with complex geometry and structural function while keeping a relatively simple global dynamic model with the smallest number of degrees of freedom possible [47]. It should be noted that since dynamic superelement is created from three dimensional finite element models of the blade, superelement possesses the whole coupling effects.

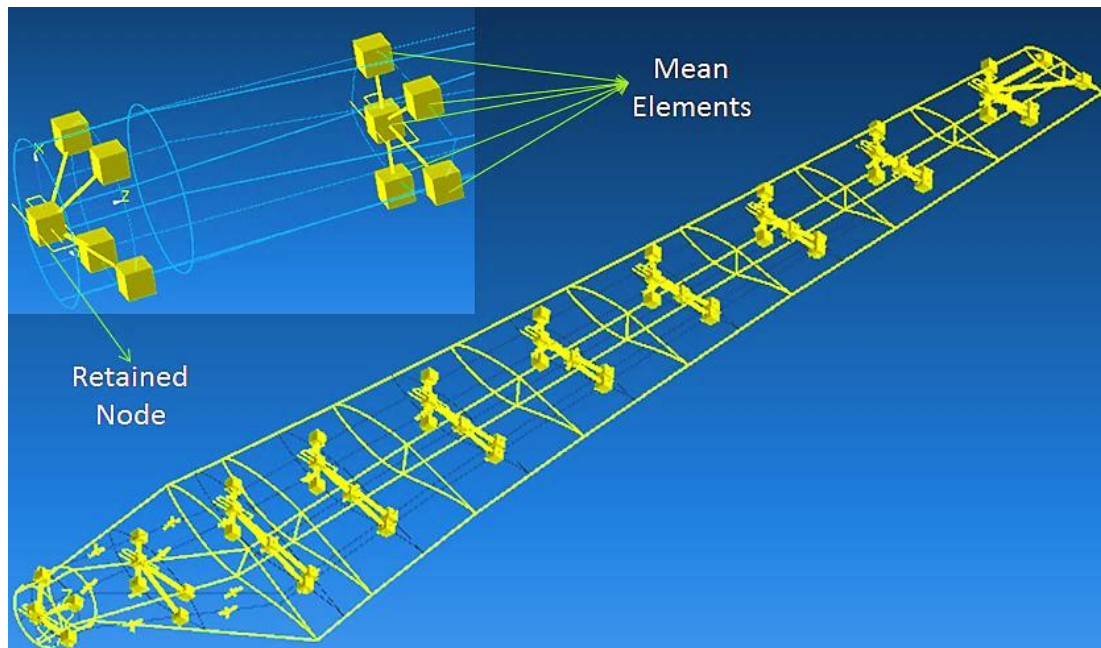
For creating the superelement model of the blade, initially, CAD drawing of the NREL Blade is exported in a “*Step*” format from MSC®/PATRAN and then the file is imported to the Samcef Field. Before the import process, the coordinates of the blade are modified to meet the specifications of the Samcef Field tool. As indicated in Figure 4.1, rotor blade span axis is defined along the z axis while the chord length is varied along the y axis. Furthermore, blade root is moved from 0.508 m to central coordinate point (0, 0, 0).



**Figure 4.1** Isometric View of the Blade Geometry in Samcef Field

In the next step, physical and mechanical properties of the E-Glass and Prepreg the Hybrid Carbon/Fiberglass composite are defined and assigned to the related 10 cross-sections with varying lay-up numbers and orientations. It should be noted that, the same mass tuning that has been applied in finite element model that is created in MSC®/PATRAN, is also repeated in Samcef Field too. After generating the shell model of the blade in graphical user interface, retained nodes are created. For the superelement generation, for each selected cross-section, for the airfoil sections, a retained node must be created at the %25 chord of the blade measured from the leading edge of the blade. At the root section of the blade since the geometry is circular, retained node is placed at the center of the circular cross-section. Once the superelement of the blade is imported into the multi-body model of the wind turbine system, retained nodes are used for applying external loads on the turbine blade. Retained nodes are also used as the connector nodes of the blade to the wind turbine system through the rotor hub. Therefore, at the root section retained node is created at the center of the circular cross-section. This node is also used as the pitch axis location through which the controller in the multi-body model of the wind turbine system controls the rotation of the blade about the pitch axis. Figure 4.2 shows the

retained nodes those are placed at the center of the each section and at the %25 chord of the airfoil sections of the blade measured from the leading edge of the blade.

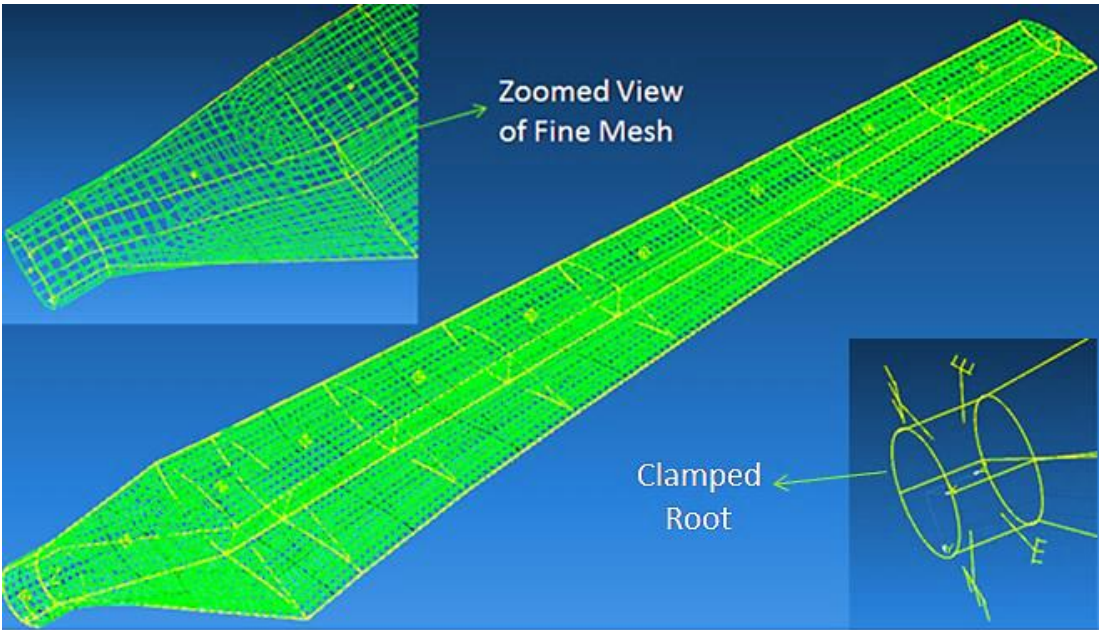


**Figure 4.2** Generation of the Retained Nodes and Mean Elements

To complete the superelement model, each retained node should be connected to the face of the corresponding section of the blade as shown in Figure 4.2. In this study, connection of the retained node with the sections of the blade is established by using the mean element that is defined in Samcef Field. Mean elements connect the retained node, which is taken as the slave node, to the master nodes on the faces of the particular section. By the use of mean elements, mean displacement of the master nodes is assigned to the retained node. Thus, retained node reflects the deformation of the blade section to which it is connected. It should be noted that in the generation of the superelement of the wind turbine blade correct displacement boundary condition must be assigned to the retained node at the root of the blade which connects the blade to the rotor hub in the wind turbine system. At this connection node, a free rotation about pitch axis must be defined to allow for the pitch motion of the blade in the multi-body simulation of the wind turbine system. In the final step of

superelement generation, finite element mesh of the blade structure is created. Fine finite element mesh with a length of 0.03 m is generated on the whole blade structure. The reason for selecting the specified mesh length is to have close element and degree of freedom numbers with the finite element model generated in MSC®/PATRAN and used in quasi-steady aeroelastic analysis. . During the mesh generation process, finite element nodes are also created on retained nodes and the dynamic superelement of the blade is generated based on the Craig and Bampton component mode method.

In the superelement blade model, the retained node that is at the root of the blade is fixed. In the three dimensional model the root section of the blade that is connected to the retained node is fixed. Figure 4.3 shows the isometric view of the meshed blade. The root section of the blade is zoomed to show the clamped root closely.



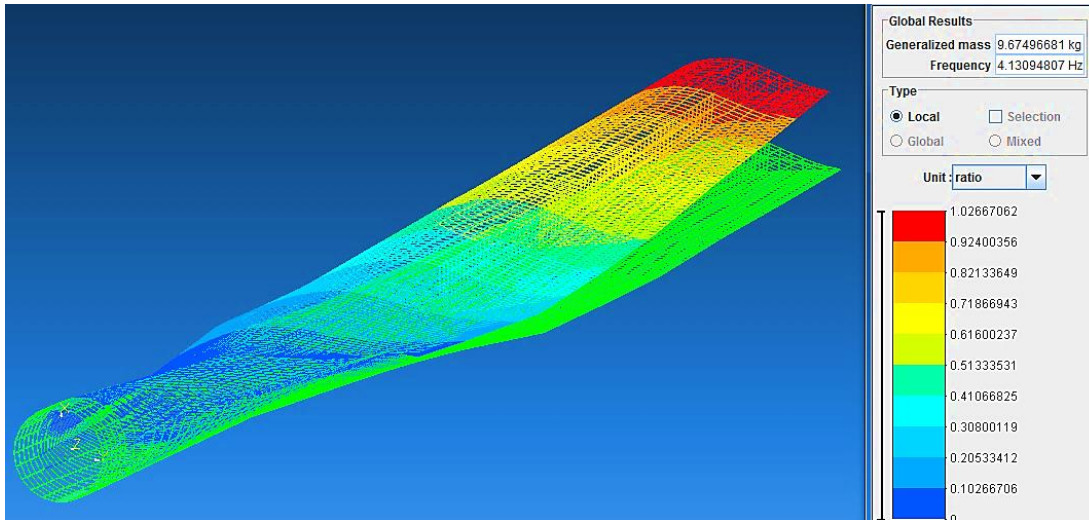
**Figure 4.3** Isometric View of the Meshed Blade

To verify the superelement of the blade, modal analyses are performed for the three dimensional blade and for the superelement blade which are both clamped at the root. Free vibration frequencies for the 1<sup>st</sup> and 2<sup>nd</sup> flapwise bending, 1<sup>st</sup> edgewise

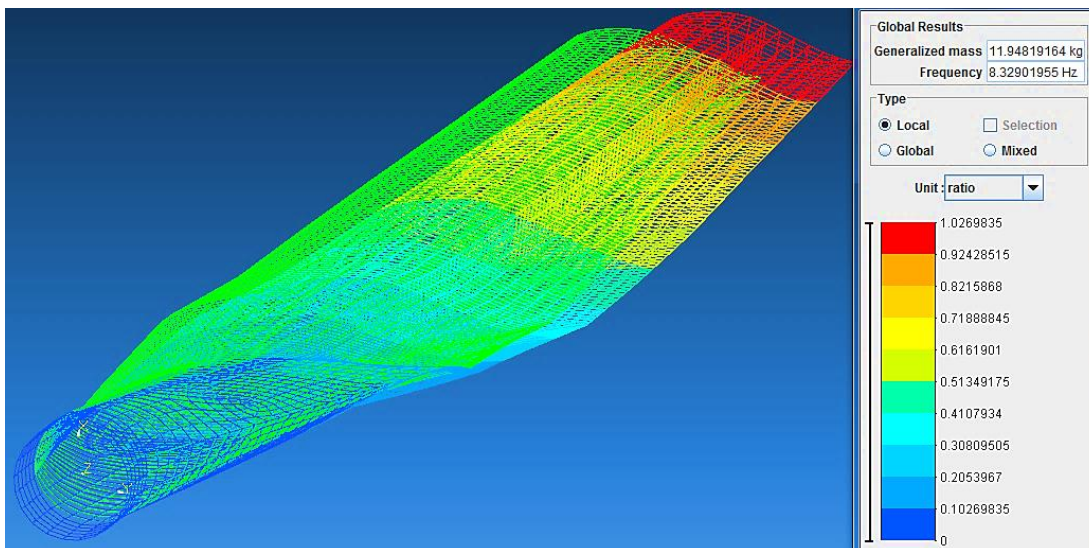
bending and 1<sup>st</sup> torsional vibration modes, which are obtained for the 3-D finite element model of the blade, are compared with the natural frequencies of the superelement of the blade and natural frequencies obtained by the modal analysis of the 3-D finite element model in MSC®/NASTRAN. Natural frequency results are compared in Table 4.1. As it is seen from the 2<sup>nd</sup> and 3<sup>rd</sup> column of Table 4.1, there exists a good agreement between the natural frequencies obtained by the 3-D FE model generated in Samcef Field and the natural frequencies obtained by the superelement of the blade. Good agreement is an indication that the superelement model represents the mass and stiffness properties of the 3-D blade structure accurately. In the 4<sup>th</sup> column of the table the natural frequencies of the finite element model generated in MSC®/NASTRAN are shown. It is seen that there exist slight differences between the natural frequencies of the 3-D Samcef FE model and the 3-D MSC®/NASTRAN FE model. The reason for differences in the natural frequencies of some modes could be due to the different solvers of Samcef and MSC®/NASTRAN. However, these differences are considered to be in an acceptable tolerance range and do not significantly affect the comparison results of quasi-steady and transient aeroelastic analysis. Figure 4.4 - Figure 4.7 show the modes shapes of the superelement blade corresponding to the lowest natural frequencies

**Table 4.1** Comparison of the Natural Frequencies

<b>Global Mode Shapes</b>	<b>3-D FE Model in Samcef Field (Hz)</b>	<b>Superelement Model Samcef Field (Hz)</b>	<b>3-D FE Model in MSC®/NASTRAN (Hz)</b>
1 <sup>st</sup> Flapwise Bending	4.13	4.13	4.13
1 <sup>st</sup> Edgewise Bending	8.32	8.33	8.13
2 <sup>nd</sup> Flapwise Bending	17.52	17.54	14.69
Torsional	28.40	28.44	24.52

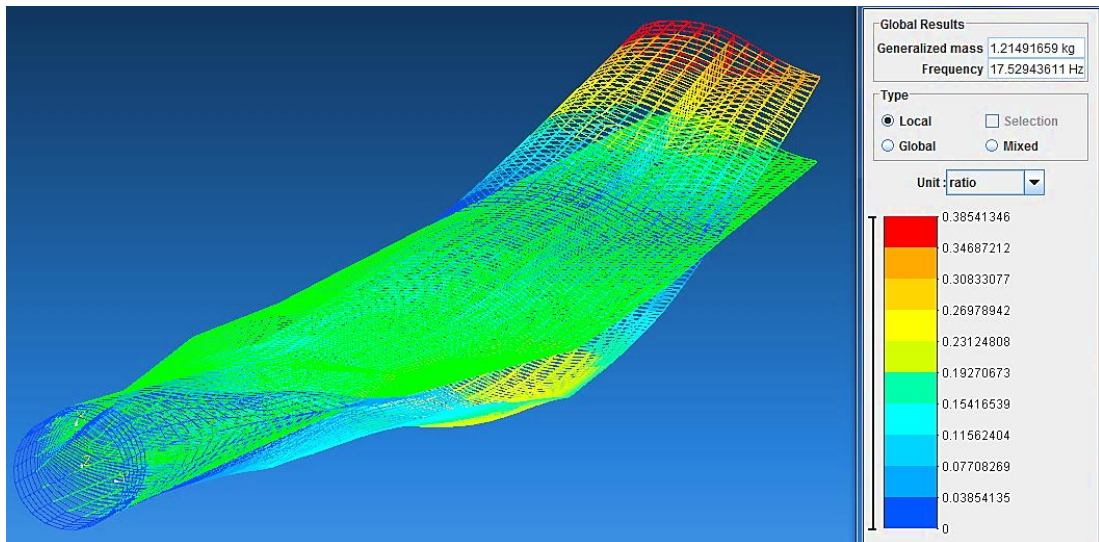


**Figure 4.4** 1st Flapwise Bending Mode Shape of the Superelement Blade Model  
 [4.13 Hz]

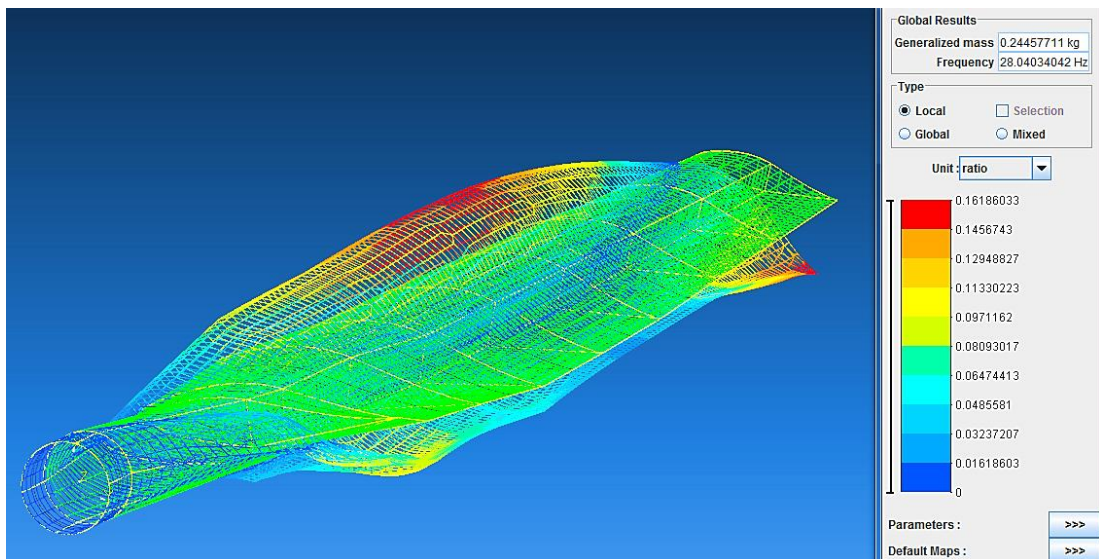


**Figure 4.5** 1st Edgewise Bending Mode Shape of the Superelement Blade Model  
 [8.32 Hz]





**Figure 4.6** 2nd Flapwise Bending Mode Shape of the Superelement Blade Model [17.52 Hz]

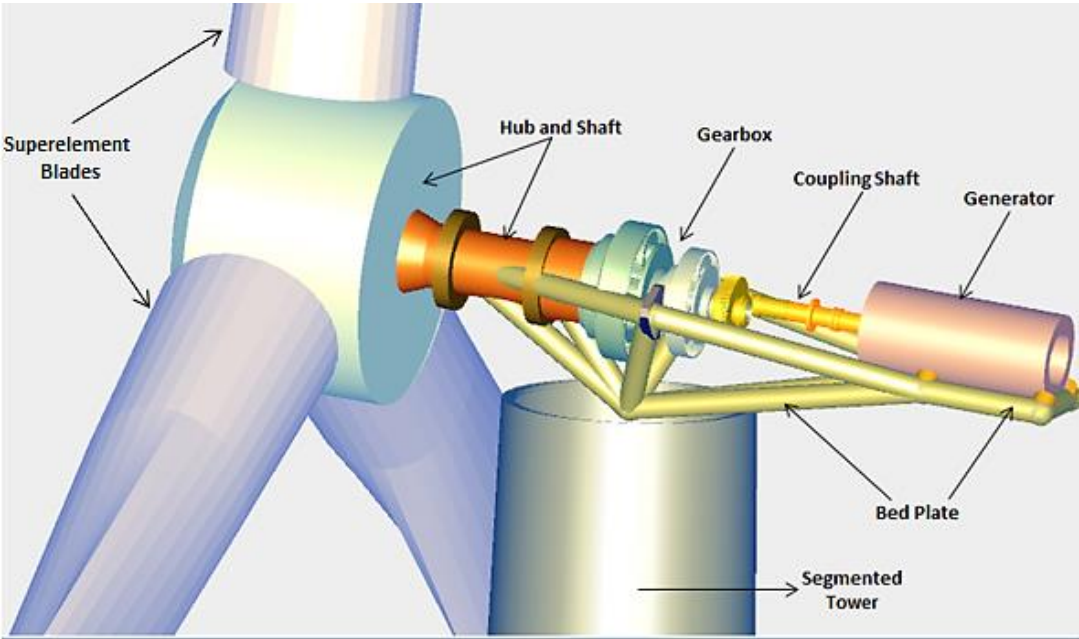


**Figure 4.7** Torsional Mode Shape of the Superelement Blade Model [28.40 Hz]

## 4.2 Wind Turbine Modeling in Samcef Wind Turbine

To study the aeroelastic response of the superelement blade, a 20 kW multi-body wind turbine model is created in Samcef Wind Turbine. For realistic and reliable

computation of the internal loads in the wind turbine system, several sub-structures, including the controller, must be included in the multi-body model of the turbine. For the parameters of the wind turbine, known properties of NREL’s turbine is taken as the reference [15]. For the drive train model, the so-called FAST drive train model that is available in the Samcef Wind Turbine is included in the wind turbine multi-body dynamic model. FAST drive train includes the bedplate, simple gearbox and generator, rotor shaft, coupling shaft, nacelle, main frame and rear frame. When FAST drive train is used, it is not necessary to include components of the drive train separately into the multi-body model of the wind turbine system. In case of separate inclusion of the drive train components, detailed properties must be provided for each component. Therefore, in the present study, to keep the modeling effort of the wind turbine system simple, FAST drive train is used. Figure 4.8 and Table 4.2 - Table 4.4 show the wind turbine and properties of the components used in the multi-body simulation of the wind turbine system.



**Figure 4.8** Multi-body Model of the Wind Turbine Parts [55]



In order to include only the transient effects due to the rotation of the wind turbine blades in the multi-body simulation of the wind turbine system, multi-body model of the wind turbine is created with almost rigid drive train and tower as the main sub-structures. By assigning a modulus of elasticity of 1000 times the modulus of elasticity of steel to the tower, flexibility of the tower is eliminated. Similarly, equivalent drive shaft torsional spring constant value is also increased 1000 times compared to the default value given for the Fast drive train in SWT. By eliminating the flexibility of the drive train and the tower, more realistic comparison of the results of the transient aeroelastic analysis of the complete wind turbine system with the results of the quasi-steady aeroelastic analysis of the turbine blade can be made.

**Table 4.2** Tower Properties Used in the Multi-body Simulation of the Wind Turbine System

<b>Tower Properties</b>	
Tower Height	11.5 m
Upper External Diameter	0.4064 m
Upper Internal Diameter	0.3636 m
Lower External Diameter	0.6096 m
Lower Internal Diameter	0.5746 m
Tower Material Young Modulus	210 E+12 Pa
Tower Material Poisson Ratio	0
Tower Material Density	7.8 E+03 kg/m <sup>3</sup>
Tower Height	11.5 m
Upper External Diameter	0.4064 m

**Table 4.3** Blade Properties Used in the Multi-body Simulation of the Wind Turbine System

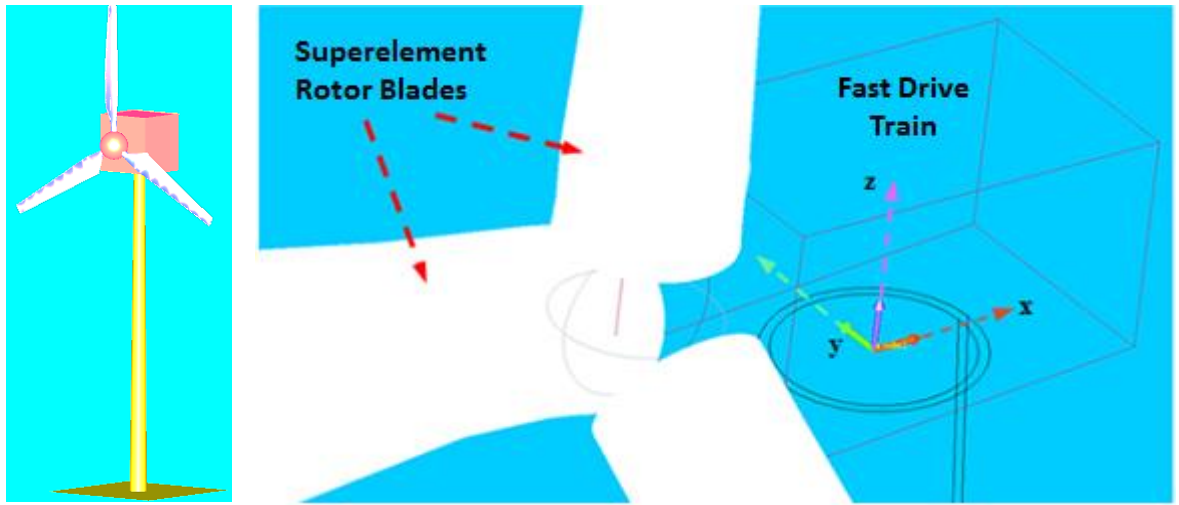
<b>Blade Properties</b>	
Blade Model Type	Super Element
Number of Blades	3
Blade Length	4.521 m
Rotor Conicity/Tilt Angle	0/0
Hub Diameter	1.016 m
Hub Total Mass	237.8 kg
Hub Inertia about Shaft Axis	118 kg.m <sup>2</sup>
Link Between Hub and Blades	Rigid

**Table 4.4** Samtech Controller & Fast Drive Train Properties in the Multi-body Simulation of the Wind Turbine System

<b>Samtech Controller &amp; Fast Drive Train Properties</b>	
Constant Generator Torque	2.6 E+03 N.m
Constant Pitch Angle	0
Angular Speed	Constant 72 R.P.M
Nacelle Total Mass	1.712 E+03 kg
Nacelle Inertia about Yaw Axis	3.789 E+03 kg*m <sup>2</sup>
Gearbox Ratio	25.13
Equivalent Drive Shaft Torsional Spring Constant	3.48 E+06 kg. m <sup>2</sup> /s <sup>2</sup> .deg
Generator Inertia about High-speed Shaft	0.22644 kg.m <sup>2</sup>
Max Torque Delivered by the Disk Brake System	115 N.m

While creating the complete wind turbine system model by defining the structural properties of the simple tower, superelement blades, Samtech controller and Fast drive train, the global coordinates are defined as shown in Figure 4.9. In the wind turbine model defined in SWT, x axis is parallel to the rotor axis, z axis is the vertical

axis perpendicular to the rotor, and y axis is perpendicular to both x and z axes. The global coordinate frame is defined as a fixed frame which does not rotate.



**Figure 4.9** Multi-body Dynamic Model of the Wind Turbine System

For the aeroelastic simulations, the calculation of aerodynamic loads is one of the main aspects for the computational tool considered. For this purpose, 2-D aerodynamic data obtained from wind tunnel experiments are introduced to the rotor system to capture the external loads and tip deflection results accurately. Aerodynamic coefficients of the circular cross-section are assigned to root part and then for the airfoil sections aerodynamic coefficients of the NREL S809 airfoil are assigned to the remaining sections of the superelement blade as shown in Figure 4.10. The aerodynamic lift, drag and moment coefficients are presented in APPENDIX C.

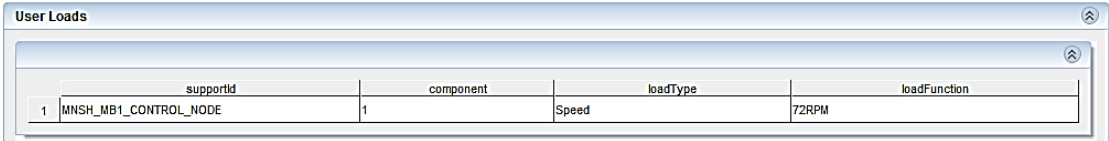
Blade Geometry						
	Blade Station 1	2	3	4	5	6
DistanceFromRoot	0 m	0.152 m	0.875 m	1.2525 m	1.7555 m	2.2585 m
Chord	0.218 m	0.218 m	0.737 m	0.711 m	0.66001 m	0.60872 m
Twist	0 deg	0 deg	20.04 deg	14.315 deg	7.454 deg	3.702 deg
Thickness	100 %	100 %	20.95 %	20.95 %	20.95 %	20.95 %
Foil Section	sect_demo_cyl	sect_S809_CLN_354	sect_S809_CLN_354	sect_S809_CLN_354	sect_S809_CLN_354	sect_S809_CLN_354

**Figure 4.10** Assignment of the Aerodynamic Coefficients to Multi-body Dynamic Model of the Wind Turbine System

It should be noted that the main interest in the transient aeroelastic analysis is to obtain the structural loads and the tip deflections of the blade accurately hence, there is no need to focus on the generated power. For this purpose, a constant function is defined in time domain and the angular speed of the rotor is set to constant angular speed of 72 rpm as illustrated in Table 4.5. Then, the created constant function is assigned to control node as shown in Figure 4.11. This control node assures that the low speed shaft of the wind turbine rotates at constant 72 rpm.

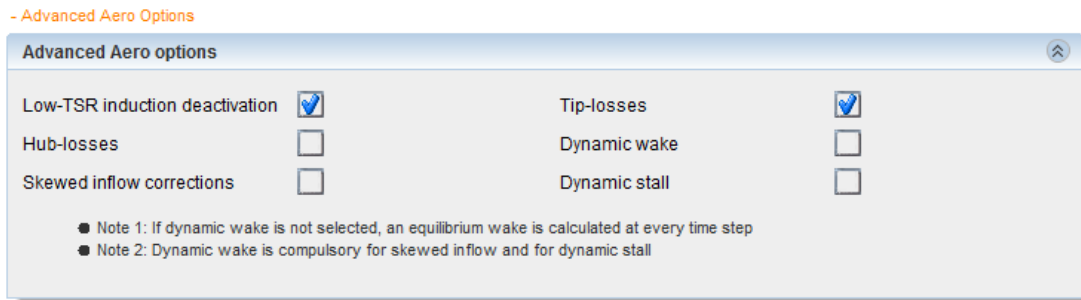
**Table 4.5** Constant Function Table Defined in Multi-body Dynamic Model of the Wind Turbine System

Function Name	X-axis Units	Y-axis Units	Value
ConstantFunc_72rpm	Time	Angular Speed	72 rpm



**Figure 4.11** Assignment of the Constant Function to Control Node

For the transient analysis, the aerodynamic conditions such as the direction and the speed of the wind are set as constant upwind at 15 m/s for the load case. For the advanced aerodynamic options, except for the tip losses which are also taken into account in the WT\_Perf calculations, as it is seen from Figure 4.12, no other unsteady effects are considered in the transient analysis. These procedures are detailed in APPENDIX D.



**Figure 4.12** Advanced Aero Options for Transient Analysis

As far as the controller is concerned, both the pitch angle and the rotor speed are imposed, thus the controller does not have any effect on the simulation.

**Table 4.6** Rated Load Case Defined in Multi-body Dynamic Model of the Wind Turbine System

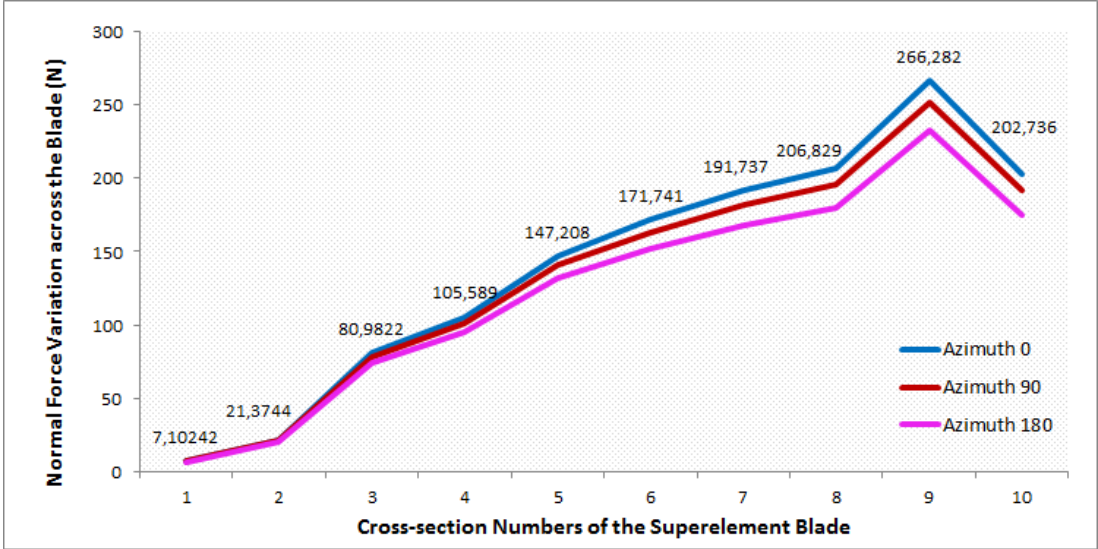
Name	Wind Speed	Rotor Speed	Blade Pitch
Rated Load Case	15 m/s	72 rpm	0 deg.

After the load case and the constant function angular velocity are created, one transient analysis is generated with duration of 30 seconds. In the results part, it can be seen that all the results quickly converge to their steady state value and this points that the transient aeroelastic analysis of the superelement blade has been completed without failure.

### 4.3 Results of the Transient Aeroelastic Analysis

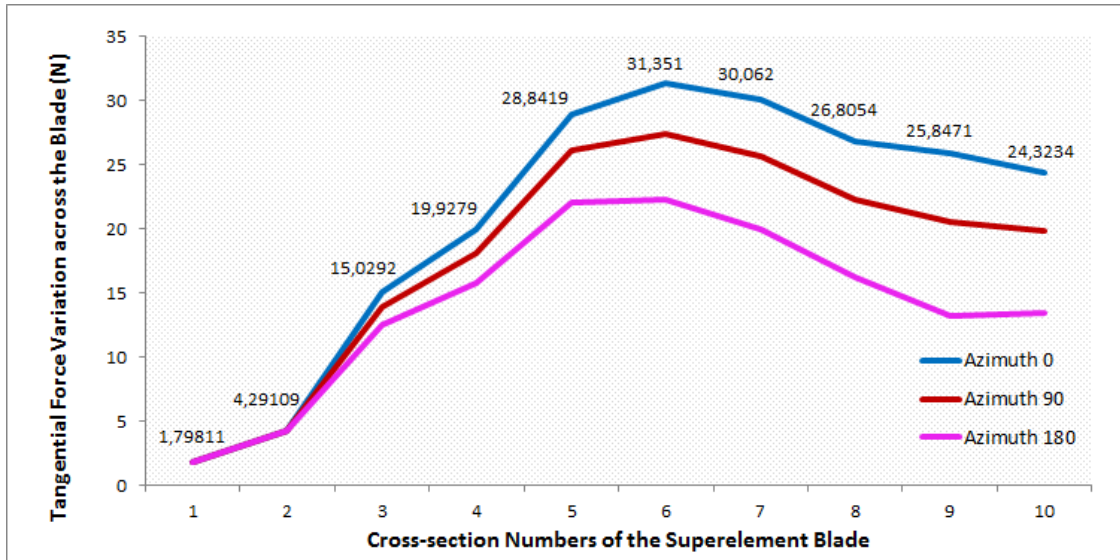
According to chosen sensors, SWT gives plenty of results but in this study only the few required sensor results are presented. Figure 4.13 shows the total force acting normal to the global coordinate system calculated by the Samcef BEM code over the superelement blade. As it is seen from, obtained normal forces for the azimuth 0 are higher than rest which is an expected result. Due to the wind shear exponent, wind

speed increases with an increasing height and this creates an increase in the amount of normal force over the sections of the blade. In Figure 4.13, the numbers on the plot show correspond to the normal force values for the 0 degree azimuthal position.

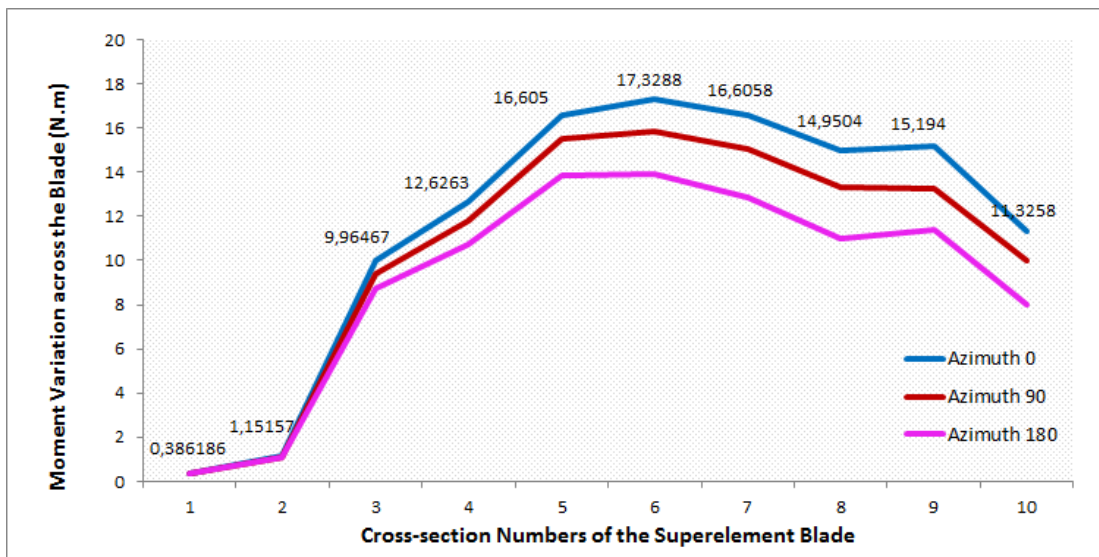


**Figure 4.13** Normal Force Variation across the Blade for Different Azimuthal Positions

Figure 4.14 and Figure 4.15 show the tangential force and moment variations across the blade. The tangential force and moment increase gradually with the radial distance, and because of the non-uniform circulations at the tip, generated moment and force decrease towards the tip section.



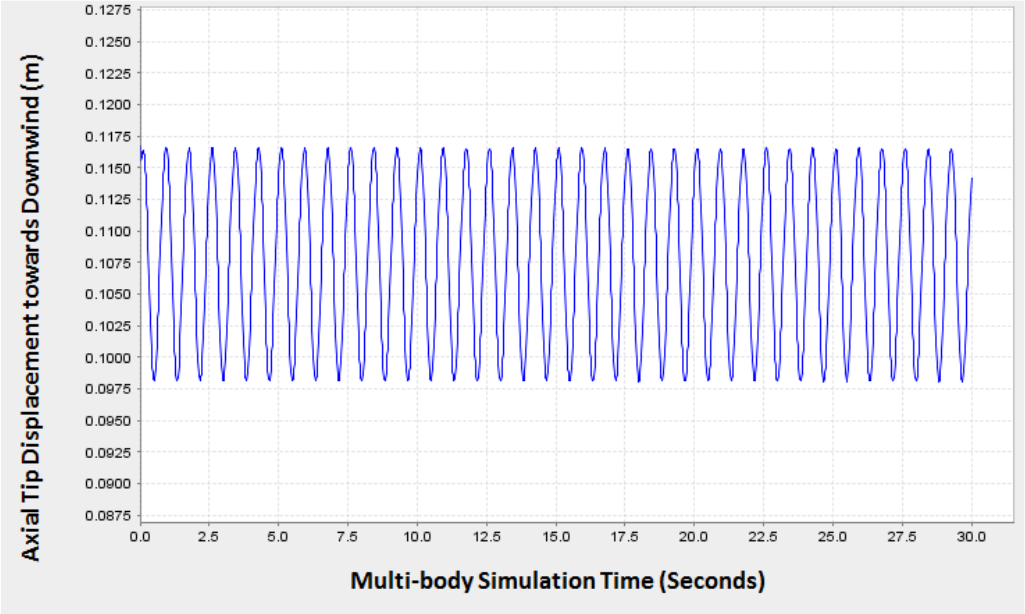
**Figure 4.14** Tangential Force Variation across the Blade for Different Azimuthal Positions



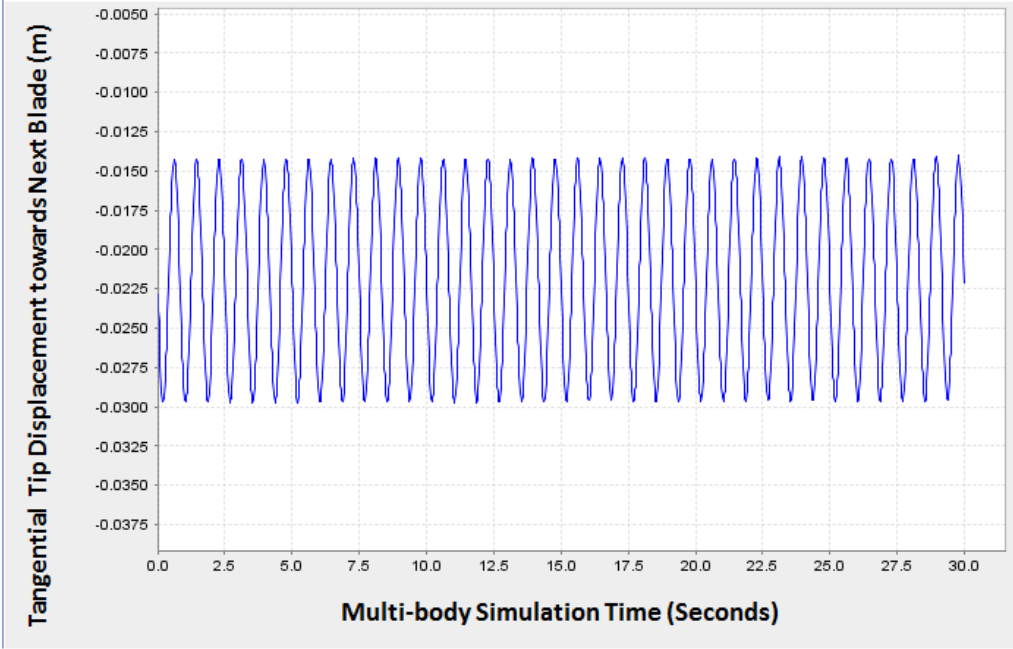
**Figure 4.15** Moment Variation across the Blade for Different Azimuthal Positions

Figure 4.16 and Figure 4.17 give the axial and tangential tip displacement of the superelement blades respectively. The maximum tip displacement converges to a value of almost 116.50 mm and the lowest tip displacement is obtained as 98.15 mm. In this case, it should be explained that that maximum tip displacement does not

correspond to 0 degree azimuthal position but it is observed at the azimuthal position of 45 degree.



**Figure 4.16** Axial Tip Displacement of the Blade towards Downwind



**Figure 4.17** Tangential Tip Displacement of the Blade towards Next Blade



In Table 4.7, sectional axial and tangential tip displacements are detailed for different azimuthal positions. From Table 4.7, it can be seen that tip deflection for the azimuth 0 is obtained as 114.368 mm which is quite close the tip deflection value obtained from the quasi-steady aeroelastic analyses.

For the other azimuthal positions, comparison of the blade tip deflections obtained by the transient analysis of the complete wind turbine system with the blade tip deflections obtained by the both quasi-steady aeroelastic analyses is done in Table 4.8. In the last column of the table, ratios of the tip deflections are presented. Table 4.8 clearly shows that because of the wind shear effect, tip deflection at the 0 degree azimuthal position, which corresponds to the vertically up position of the blade, is higher than the tip deflections at the other azimuthal positions. It is also noted that tip deflections determined by the quasi-steady aeroelastic analysis with concentrated loads are higher than the tip deflections determined by the transient analysis of the wind turbine system. However, ratio column of Table 4.8 shows that tip deflections determined by the quasi-steady aeroelastic analyses are within %10 of the tip deflections determined by the transient analyses for different azimuthal positions. Moreover, it is seen that tip deflection results of quasi-steady aeroelastic analyses with the distributed load case are closer to the tip deflection results obtained by the transient aeroelastic analysis a than the tip deflection results obtained by the concentrated load case.

It can be considered that if the same finite element solver is used for quasi-steady aeroelastic analysis and superelement blade generation, then the differences in the tip deflections would be lower. It should be noted that in the present study, MSC®/NASTRAN is chosen as the finite element solver to make use of the “*shifting nodes*” feature of MSC®/PATRAN so that aerodynamic loads can be applied on the deformed configuration of the blade. It is considered that quasi-steady aeroelastic analyses can be used reliably in the preliminary design stage to perform design iterations to come up with a blade structure that satisfies a certain stiffness

requirement. Obviously, in the detailed design phase, multi-body simulations of the wind turbine system have to be performed for detailed analyses.

**Table 4.7** Axial and Tangential Tip Displacement Variations at Different Azimuthal Positions

# of Section	AxialDisp Azimuth 0 (m)	TangDisp Azimuth 0 (m)	AxialDisp Azimuth 90 (m)	TangDisp Azimuth 90 (m)	AxialDisp Azimuth 180 (m)	TangDisp Azimuth 180 (m)
1	2.33E-12	1.16E-09	2.22E-12	4.93E-09	2.10E-12	1.03E-09
2	0.001444	0.000273	0.001326	1.28E-06	0.001234	0.000322
3	0.005043	0.001092	0.004491	0.00032	0.004329	0.001147
4	0.011759	0.002897	0.010377	0.001457	0.010159	0.002825
5	0.023475	0.005634	0.020803	0.003252	0.020377	0.005354
6	0.037656	0.008668	0.033564	0.005293	0.032763	0.008157
7	0.052568	0.011715	0.046983	0.007333	0.045767	0.010971
8	0.069116	0.014796	0.061929	0.009389	0.060184	0.013816
9	0.086777	0.017802	0.077908	0.011362	0.075556	0.016593
10	0.114368	0.022331	0.102899	0.014343	0.099554	0.020785

**Table 4.8** Comparison of the Tip Deflection Results

Azimuth Positions (degree)	Tip Displacement (Quasi-steady) Concentrated Load Case (mm)	Tip Displacement (Quasi-steady) Distributed Load Case (mm)	Tip Displacement (Transient) (mm)	Ratios
0	114.94	112.22	114.368	1.005/0.981
90	110.69	103.61	102.899	1.076/1.007
180	105.15	100.38	99.554	1.056/1.008
270	110.69	103.61	102.899	1.076/1.007

One last comparison is performed between the flapwise bending moment of quasi-steady aeroelastic analyses and the flapwise bending moment of the transient

aeroelastic analysis. In Table 4.9, the comparison of the flapwise bending moments at the end of the cylindrical region ( $r=0.66$  m) for different azimuthal positions are presented. The bending moments are calculated by utilizing the results of blade element momentum calculations performed in WT\_Perf and SAMCEF. Once the sectional forces are calculated, root bending moment is calculated by summing the moment contribution of each sectional force.

**Table 4.9** Flapwise Bending Moments at  $r=0.66$  m Calculated for the Constant Wind Speed (15 m/s).

<b>Azimuth Positions</b>	<b>Flapwise Moment Concentrated Load Case with 20 Blade Sections (N.m)</b>	<b>Flapwise Moment Distributed Load Case with 10 Blade Sections (N.m)</b>	<b>Flapwise Moment Transient (N.m)</b>
<b>0</b>	3711,121	3612.281	3687.545
<b>90</b>	3559,388	3480.198	3495.479
<b>180</b>	3328,284	3262.835	3255.559

From Table 4.9, it is seen that the flapwise bending moments calculated utilizing the output of WT\_Perf for the concentrated loads case of quasi-steady aeroelastic analysis are higher than the flapwise root bending moments calculated by SWT. The reason for the difference is due to the fact that in WT\_Perf, for the concentrated load case 20 blade segments are used in the analysis whereas in SWT 10 blade segments are used. For the distributed load case same numbers of segments (10 segments) are used in both WT\_Perf and in SWT. Therefore, for distributed load case with the same number blade segments as the transient aeroelastic analysis, similar force distribution is obtained, and better approximation of the root bending moment is achieved. It should also be noted that the reason for the difference in the tip displacements obtained by the quasi-steady aeroelastic analysis with the concentrated

load case and the transient analysis can be mainly attributed to the higher loads used in the quasi-steady aeroelastic analysis.

## CHAPTER 5

### CONCLUSION

This thesis aims to present a comparison study of quasi-steady and transient aeroelastic analysis of a composite wind turbine blade in steady wind conditions. To conduct quasi-steady aeroelastic analysis, inverse design methodology is applied to build up a reference turbine blade to be used in the aeroelastic analysis. Blade of the unsteady aerodynamics experiment (UAE) research wind turbine is taken as the reference blade [15]. A 3-D blade design is performed by performing design iterations such that number of composite layers is modified to obtain closer sectional beam properties as the known sectional beam properties of the reference blade of the unsteady aerodynamics experiment (UAE) research wind turbine. Spanwise and chordwise ply numbers are changed in an iterative fashion, and each blade section is evaluated in VABS tool until the desired sectional beam properties approximately match with the known sectional beam properties of the UAE Phase VI blade. The main goal in the inverse design was to match the flapwise bending stiffness of the NREL blade as closely as possible. It should be noted that with the inverse design approach, it is aimed to come up a 3-D blade design which has reasonable sectional blade properties which are not unrealistically high or low compared to the sectional beam properties of the NREL blade. 3-D blade design is then used to construct the finite element model of the blade to be used for the quasi-steady aeroelastic analyses of the blade only and the transient aeroelastic analysis of the complete wind turbine system in Samcef Wind Turbine (SWT) multi-body code. After completing the finite element model, coupling of the BEM based aerodynamic module with the finite element program MSC®/NASTRAN is performed. Blade element momentum

analyses are performed by WT\_Perf and the sectional loads calculated by WT\_Perf are applied on the deformed structural model of the blade by using the “*shifting nodes*” feature of MSC®/PATRAN. By coupling the BEM based aerodynamics with the structural finite element solver, quasi-steady aeroelastic response of the blade is performed. In the preliminary analysis, three iterations are performed to determine the deformed state of the blade at the 0 degree azimuthal position. At end of the 4<sup>th</sup> iteration, convergence is achieved and same flapwise tip deflection values are obtained. For the other azimuthal positions same procedure has been followed and final tip deflection values are recorded. Another case of quasi-steady aeroelastic analysis is conducted by distributing the forces over the nodes on the upper suction side of the blade. In the distributed load case, to achieve close aerodynamic results with the BEM results of transient analysis, blade is investigated in 10 discrete sections in WT\_Perf analysis and by following the same procedure detailed in the first case, deflection results are obtained for all azimuthal positions. Quasi-steady aeroelastic analyses results showed that the difference between the tip deflections in consecutive iterations is very small. It is therefore concluded that the inverse design blade is actually very rigid.

In the second part of the thesis, transient analysis of NREL blade is conducted by the multi-body dynamic code Samcef Wind Turbine. Initially, dynamic superelement model of the reference blade is created in the Samcef Field in a similar manner to the creation of the finite element model in MSC®/PATRAN. To verify the consistency between the superelement model and the 3-D finite element model, modal analyses are performed for both the superelement blade and the 3-D finite element model of the blade. It is seen that natural frequencies determined by the modal analysis of the superelement blade and the 3-D finite element model of the blade are very close to each other indicating the reliability of the superelement of the blade model. Superelement model of the blade is then introduced into the multi-body model of the wind turbine system to perform wind turbine simulation. In order to include only the transient effects due to the rotation of the wind turbine blades, drive train and tower are created as almost rigid sub-structures. By eliminating the

flexibility of the drive train and the tower, more realistic comparison of the results of the transient aeroelastic analysis of the complete wind turbine system with flexible blades are made with the results of the quasi-steady aeroelastic analysis of the turbine blade only. It should be noted that the main interest in the transient aeroelastic analysis is to obtain the structural loads and the tip deflections of the blade accurately hence, no there is need to focus on the generated power. For this purpose, a constant function is defined in time domain and the angular speed of the rotor is set to constant angular speed of 72 rpm. Blade tip deflections obtained by the transient analysis of the complete wind turbine system are compared with the blade tip deflections obtained by the quasi-steady aeroelastic analyses performed by coupling WT\_Perf and MSC®/NASTRAN. Reasonably good agreement is seen between the tip deflections obtained by the transient analysis of the complete wind turbine system and both load cases of the quasi-steady aeroelastic analyses of the blade only. The main reason for the difference in the tip displacements obtained by the quasi-steady aeroelastic analysis with the concentrated load case and transient aeroelastic analysis is attributed to the higher loads used in quasi-steady aeroelastic analysis. For the concentrated load case, the difference in the loads is considered to be due to the use of different BEM solvers in quasi-steady aeroelastic analysis and transient analysis performed in SWT, and also due to the use of different number of blade segments in the quasi-steady aeroelastic analysis and transient aeroelastic analysis. On the other hand, for the distributed load case, very good agreement is obtained between the tip displacements obtained by the quasi-steady aeroelastic analysis and transient aeroelastic analysis. For the distributed load case, good agreement between the tip displacements is attributed to the same number of blade segments used in the quasi-steady aeroelastic analysis and transient aeroelastic analysis. It is noted that the particular blade that is studied is very rigid, and therefore good agreement between the quasi-steady aeroelastic analysis of the blade only and the transient analysis of the complete wind turbine system may be attributed to the rigidity of the blade. Transient effects do not show up significantly in blades that are more rigid. For small size blades, it is considered that in the preliminary design stage, quasi-steady aeroelastic analysis of the blade can give very

reliable idea about the stiffness and strength of the blade eliminating the need of performing multi-body simulation of the complete wind turbine system. It is concluded that quasi-steady aeroelastic analysis of the blade performed by coupling the finite element solver with a BEM based aerodynamic tool can be used for effectively in preliminary design stage of composite wind turbine blades.

As future work, quasi-steady aeroelastic analysis approach can be extended such that instead of linear structural solver, geometrically non-linear structural solver can be coupled with a BEM based aerodynamic solver. With the use of non-linear structural solver, longer and more flexible blades can also be analyzed by the quasi-steady aeroelastic analysis approach in the preliminary design stage. As a further study, coupling of the BEM based aerodynamics and the structural solver can be fully automated eliminating the need of user intervention during the quasi-steady aeroelastic analysis of the blade. The most challenging future goal would be to gather efforts both in the aerodynamic side and the structural side to develop a national multi-body code that can be used for the simulation of the wind turbine systems.



## REFERENCES

- [1] Golding, E.W.: “*The Generation of Electricity by Windpower*”, Auflage 1955; Reprint with additional material, E. & F.N. Spon Ltd., London 1976.
- [2] Rieseberg, H.J., “*Mühlen in Berlin (Mills in Berlin)*”, Medusa Verlagsges. Berlin-Wien 1983.
- [3] Bennert, W. und Werner, U.-J.: *Windenergie (Wind energy)*, VEB Verlag Technik, Berlin 1989.
- [4] The World Wind Energy Association 2013 Half-year Report.
- [5] Vestas, Discover the Unique Power of the Wind, <http://www.vestas.com/en/modern-energy/experience-the-wind/wind-power-through-the-ages.aspx>, and last accessed date: 26.05.2013.
- [6] Manwell J. F., McGowan J. G. and Rogers A.L., “*Wind Energy Explained: Theory, Design and Application* Second Edition”, Wiley Press, United Kingdom, 2009.
- [7] EWEA – European Wind Energy Association; “*Wind Energy – The Facts: A Guide to the Technology, Economics and Future of Wind Power*”, London, Sterling, V.A, 2009.
- [8] Nelson, Vaughn, “*Wind Energy - Renewable Energy and the Environment*”, CRC Press, Boca Raton, 2009.

- [9] Hills, R.L.: “*Power from the Wind – A history of windmill technology*”, Cambridge University Press, 1996.
- [10] Tong, Wei “*Wind Power Generation and Wind Turbine Design*”, WIT Press, Ashurst, Southampton, 2010.
- [11] Drachmann, A.G., “*Heron’s windmill*”, *Centaurus*, 7, pp. 145–151, 1961.
- [12] Spera, D. A. “*Wind Turbine Technology: Fundamental Concepts of Wind Turbine Engineering*”. ASME Press, New York, 1994.
- [13] M. O. L. Hansen: “*Aerodynamics of Wind Turbines*”. 2nd Edition, Earthscan, London, UK, 2008
- [14] Tsung-Yi Lin, Baichun Zhang; “*The Vertical Shaft Type Wind-power Chinese Square-pallet Chain-pump*”, Department of Mechanical Engineering, Southern Taiwan University, Tainan 710, Taiwan.
- [15] Hand, M.M.; Simms, D.A.; Fingersh, L.J.; Jager, D.W.; Cotrell, J.R.; Schreck, S.J.; Larwood, S.M. “*Unsteady Aerodynamics Experiment Phase VI: Wind Tunnel Test Configurations and Available Data Campaigns*”, NREL/TP-500-29955; Golden, CO: National Renewable Energy Laboratory, 2001.
- [16] Samcef Field, <http://www.lmsintl.com/samcef-field>, last accessed date: 30.11.2013.
- [17] Jain, Pramod: “*Wind Energy Engineering*”, McGraw-Hill Companies, New York, 2011.

- [18] Hermann-Josef Wagner, Jyotirmay Mathur: “*Introduction to Wind Energy Systems*”, Springer, Springer-Verlag Berlin Heidelberg 2009.
- [19] Erich Hau: “*Wind Turbines: Fundamentals, Technologies, Application and Economics*”. 2nd Edition, Springer, 2006.
- [20] A.R. Jha, Ph.D.: “*Wind Turbine Technology*”, CRC Press 2010.
- [21] Holierhoek, Jessica Gabriëlle: “*Aeroelasticity of Large Wind Turbines*”, PhD. Thesis, Technische Universiteit Delft, November 2008.
- [22] Hansen M.O.L. Sørensen J.N. Voutsinas S. Sørensen N. and Madsen H.Aa.: “*State of the art in wind turbine aerodynamics and aeroelasticity*”. Progress in Aerospace Sciences, 42:285–330, 2006.
- [23] Burton T., Sharpe D., Jenkins N., Bossanyi E.: “*Wind Energy Handbook*”, John Wiley and Sons, 2001.
- [24] Sathyajith, M.; Philip, G.S.: “*Advances in Wind Energy Conversion Technology*”, Environmental Science and Engineering, Springer-Verlag Berlin Heidelberg, 2011.
- [25] Başkut, E.; Akgül, A: “*Development of a Closely Coupled Approach for Solution of Static and Dynamic Aeroelastic Problems*” METU, June, 2010.
- [26] Moriarty, Patrick J.; Hansen, A.C.: “*AeroDyn Theory Manual*”, National Renewable Energy Laboratory.
- [27] Griffin D.A.; Ashwill T.D.: “*Alternative Composite Materials for Megawatt-Scale Wind Turbine Blades: Design Considerations and Recommended Testings*”,

American Institute of Aeronautics and Astronautics, Inc. and the American Society of Mechanical Engineers, 2003.

[28] Yu. W. 2011; “*VABS Manual for Users*”. ”, Utah State University, Logan, 2011.

[29] Yu. W and Chen H.; “*Manual of PreVABS*”, Utah State University, Logan, Utah 84322-4130.

[30] Yu. W. 2011; “*VABS Manual for Developers*”. Utah State University, Logan, 2011.

[31] Rwigema M. K.; “*Propeller Blade Element Momentum Theory with Vortex Wake Deflection*”, School of Mechanical, Industrial and Aeronautical Engineering University of the Witwatersrand, Private Bag 3, Johannesburg, 2050, South Africa.

[32] Simms, D.; Schreck, S.; Hand, M.; Fingersh, L.J. 2001: “*NREL Unsteady Aerodynamics Experiment in the NASA-Ames Wind Tunnel: A Comparison of Predictions to Measurements*” NREL/TP-500-29494. Golden, CO: National Renewable Energy Laboratory.

[33] D.P. Molenaar: “*Cost-effective Design and Operation of Variable Speed Wind Turbines-Closing the Gap between the Control Engineering and the Wind Engineering Community*”. PhD. Thesis, Technische Universiteit Delft, 2003.

[34] Weinzierl, Guido; “*QBLADE: A BEM Based Simulation-Tool for Wind Turbine Blades with Active Flow Control Elements*”, Technische Universität Berlin Fakultät V Institut für Strömungsmechanik und Technische Akustik Fachgebiet für Experimentelle Strömungsmechanik.

- [35] R. R. Ramsay, J. M. Janiszewska, G.M. Gregorek; “*Wind Tunnel Testing of Three S809 Aileron Configurations for use on Horizontal Axis Wind Turbines - Airfoil Performance Report*”, The Ohio State University, Columbus, Ohio ,July 1996.
- [36] Dan M. Somers; “*Design and Experimental Results of S809*”, Airfoils Incorporated State College, Pennsylvania, January 1997.
- [37] Wenbin Yu, Dewey H. Hodges; “*Generalized Timoshenko Theory of the Variational Asymptotic Beam Sectional Analysis*”, Georgia Institute of Technology, Atlanta, Georgia 30332-0150.
- [38] Al-Bahadly, Ibrahim; “*Wind Turbines*”, Janeza Trdine 9, 51000 Rijeka, Croatia, March- 2011.
- [39] Wenbin Yu, Vitali V. Volovoi, Dewey H. Hodges and Xianyu Hong; “*Validation of the Variational Asymptotic Beam Sectional Analysis VABS*”, Georgia Institute of Technology, Atlanta, Georgia 30332-0150.
- [40] Wenbin Yu, Dewey H. Hodges, Vitali V. Volovoi and Eduardo D. Fuchs; “*A generalized Vlasov theory for composite beams*”, Department of Mechanical and Aerospace Engineering, Utah State University, Logan, UT 84322-4130, USA and School of Aerospace Engineering, Georgia Institute of Technology, Atlanta, GA 30332-0150, USA
- [41] J.M. Jonkman; “*Modeling of the UAE Wind Turbine for Refinement of FAST-AD*”, NREL/TP-500-34755, National Renewable Energy Laboratory 1617 Cole Boulevard Golden, Colorado 80401-3393, December 2003.

- [42] Bir, G.; Migliore, P; “*Preliminary Structural Design of Composite Blades for Two and Three-Blade Rotors*”, NREL/TP-500-31486; Golden, CO: National Renewable Energy Laboratory, 2004.
- [43] David Verelst; “*Flexible Wind Turbine Blades: a FEM-BEM Coupled Model Approach*”, Delft University of Technology (TU Delft), January 2009.
- [44] Leihong Li; “*Structural Design of Composite Rotor Blades with Consideration of Manufacturability, Durability, and Manufacturing Uncertainties*”, PhD. Thesis, Georgia Institute of Technology, August 2008.
- [45] Evangelos Papadopoulos; “*Heron of Alexandria*”, Department of Mechanical Engineering, National Technical University of Athens, 15780 Athens, Greece.
- [46] Dayton A. Griffin.; “*NREL Advanced Research Turbine (ART) Aerodynamic Design of ART-2B Rotor Blades*”, Golden, CO: NREL, 2001.
- [47] Heege, A., Hemmelmann, J., Bastard, L., Sanchez, J.L., Lens, L., Omiciuolo, M.; “*Matching Experimental and Numerical Data of Dynamic Wind Turbine Loads by Modeling of Defects*”, EWEC 2009, Marseille, France, 16-19 March 2009.
- [48] Robert E. Wilson, Peter B. S. Lissaman, Stel N. Walker; “*Aerodynamic Performance of Wind Turbines*”, Oregon State University Corvallis, Oregon June, 1976.
- [49] Mikkelsen, Robert: “*Actuator Disc Methods Applied to Wind Turbines*”, MEK-FM-PHD 2003-02, Fluid Mechanics Department of Mechanical Engineering Technical University of Denmark June, 2003.
- [50] Froude, R. E.; “*On the Part Played in Propulsion by Difference in Pressure*”. Transaction of the Institute of Naval Architects, 1889; 30: 390.

- [51] “*Ullesthorpe Windmill – The Oldest Windmill, Ancient Persian Vertical Axis Windmills*”, <http://www.ullesthorpewindmill.org.uk/>, last visited on 02.03.2013.
- [52] “*Department of Defense Handbook – Composite Materials Handbook, Volume 2*”. Polymer Matrix Composites Material Properties, MIL-HDBK-17-2F, Volume 2 of 5, JUNE 2002.
- [53] Buhl, Marshall L. “*WT\_Perf User’s Guide*.” National Wind Technology Center, 2004.
- [54] Dr. David J. Laino, “*FoilCheck; a utility for creating aerodynamic input files for AeroDyn-based programs*”, National Wind Technology Center, May 2002.
- [55] “*Samcef Wind Turbines (SWT) User Help*”, V.3.3, LMS Inc. (2013), P.87, P. 154, Pp: 234-236.
- [56] “*Samcef Mecano*”, <http://www.lmsintl.com/?sitenavid=8435E5BB-C04D-49AB-B72A-9CB01D6FD9DB>, last accessed date: 02.11.2013.
- [57] John T. Young, William B. Haile; “*Premier on the Craig-Bampton Method: An Introduction to Boundary Node Functions, Base Shake Analyses, Load Transformation Matrices, Modal Synthesis and Much More*”, October 4, 2000.
- [58] P. P. Friedmann; “*Aeroelastic modeling of large wind turbines*”, Journal of the American Helicopter Society, 1976, 21(4): 17–28.
- [59] H. Ottens, R. J. Zwaan; “*Description of a method to calculate the aeroelastic stability of a 2-bladed horizontal axis wind turbine*”. Technical Report NLR/TR-78115L. NLR National Aerospace Laboratory, Roskilde 1978.

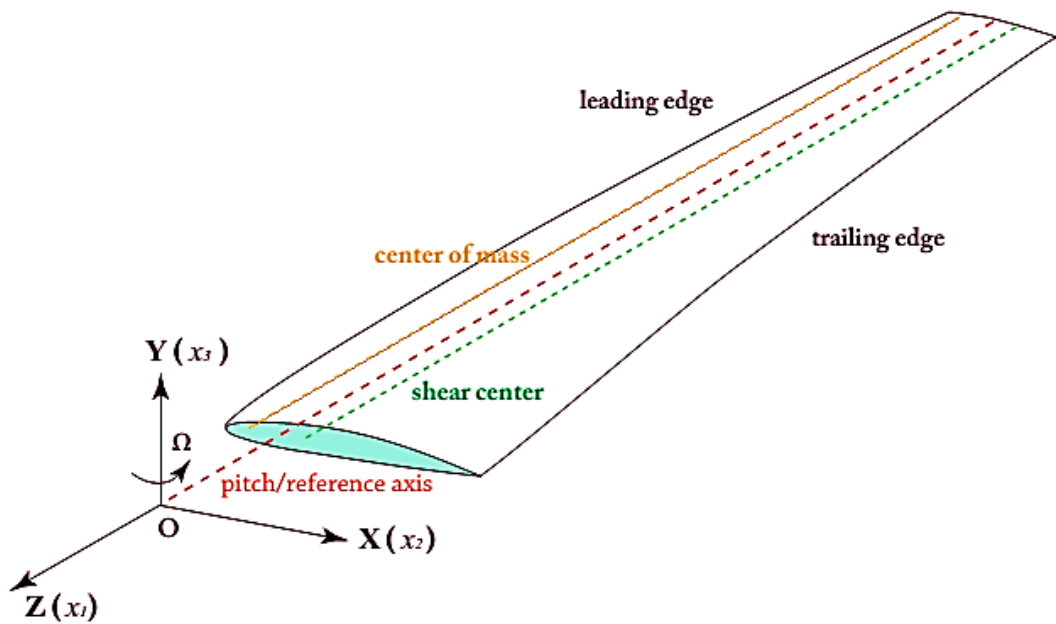
- [60] A. D. Garrad; “*Dynamics of wind turbines*”. IEE Proceedings. Part A. Physical Science, Measurements and Instrumentation, Management and Education, Reviews, 1983, 130(9): 523–530.
- [61] D. C. Quarton; “*The evolution of wind turbine design analysis-a twenty year progress review*”, Wind Energy (Chichester, England), 1998, 1(S1): 5–24.
- [62] J.T. Petersen, H.A. Madsen, A. Björck, P. Enevoldsen, S. Øye, H. Ganander, D. Winkelaar; “*Prediction of Dynamic Loads and Induced Vibrations in Stall*”, Risø-R-1045(EN), Risø National Laboratory, Roskilde, 1998.
- [63] Professional Services Group. “*ADAMS/WT 2.0 User’s Guide*”. Technical report, Mechanical Dynamics, 6530 E. Virginia St. Mesa, AZ 85215, 1998.
- [64] Garrad Hassan and Partners; “*GH-BLADED for Windows, A design Tool for Wind Turbine Performance and Loading – User Manual*”. Garrad Hassan & Partners Limited, Bristol, England, 2003.
- [65] P.M.M. Bongers; “*DUWECS Reference guide V2.0, Delft University Wind Energy Converter Simulation Package*”, Delft University of Technology, The Netherlands, DUT-MEMT 26, 1993.
- [66] Jason M. Jonkman, Marshall L. Buhl Jr.; “*FAST User’s Guide*”, Technical Report NREL/EL-500-38230, August 2005.
- [67] Torben Juul Larsen, Anders Melchior Hansen; “*HAWC2, the User’s Manual*”, Risø National Laboratory Technical University of Denmark Roskilde, Denmark December 2007



## APPENDIX A

### PREVABS INPUT FILES

**The airfoil geometric data file:** This PreVABS input file includes the specification of the blade airfoil configuration. As can be observed from the example of an input file, first line represents the four variables; dimensional chord length (m), twist angle (deg) and pitch axis locations in x-y coordinate frame of the consisting blade section.



A. 1 Schematic of VABS Coordinates System

The coordinate system of the cross-section lies on the chord line and the origin is the intersecting point of the chord line and outer profile of the section which is the

leading point of the cross section as shown in A.1. Thus, pitch axis location in X coordinate should always be positive at the input file because the origin of the coordinate system is always before the intersecting point of the pitch/reference axis and the chord line. Y coordinate could be either positive or negative depending on the relative position to the chord line. In the example, chord line of the reference blade section is given as 0.355 m and the pitch axis location is defined at the %25 of the chord line. In PreVABS input file, the twist angle represents a counter-clock-wise rotation of the cross-section and in the given example the twist angle is decided as -1.815 degree.

The second section in the input file represents the number of webs, location of webs in X-Y coordinate frame and web orientations (tilting angle in degree). In the reference blade there is only one shear web placed at the center of the cross-section and vertical w.r.t chord line. The remaining blocks in the input file (3<sup>rd</sup> and 4<sup>th</sup> ) define the profile of airfoil section by providing the coordinates of the nodal points for low pressure surface and high pressure surface. Both LPS and HPS of the reference blade cross-sections consist of 33 nodes as can be seen from the input file.

The following is an example of a blade section profile input file.

```
! Sec_profile_real_balde_NREL_S809.input
!
!=====
!(1) Chord length (m) twisted angle (deg) pitch axis location (x y) (m)
!=====
!
!           0.355           -1.815           0.08875           0.000
!
!=====
!(2) (A) Non-dimensional positions for Web centers ((x, y) position for each web)
!(b) Webs' titling angles (w.r.t. chord line)
!Web center should be on the cord line (y=0.0)
!=====
! Total number of webs in this cross section
! Nwebs
!     1
!
! Webi_nd_x, Webi_nd_y Web_tl_angles (deg)
! .48882           0.0           90
!
```

```

=====
!(3) Non-dimensional profile data for low pressure surface (LPS)
=====
!
! Chord line status 'Tilt' or 'Regular'
! Currently (8/08) always 'Regular' -->: farthest trailing edge point lies on the
  Regular
!
! Chord line rotation angle (deg) (0 deg if cord line is on x axis)
  0.0
!
! Number of nods @ LPS (top surface)
!
33
!
!   x   y (non-dimensional)
!
0       0
0.000204 0.001942
0.000658 0.003723
0.006026 0.012615
0.016590 0.022290
0.031910 0.032299
0.051823 0.042352
0.076035 0.052224
0.104263 0.061697
0.136174 0.070580
0.171409 0.078687
0.209576 0.085851
0.250247 0.091908
0.292970 0.096703
0.337260 0.100070
0.382612 0.101840
0.428461 0.101760
0.474243 0.099392
0.519832 0.093268
0.567830 0.084095
0.617331 0.074214
0.667064 0.064353
0.715952 0.054872
0.763042 0.045974
0.807470 0.037766
0.848455 0.030280
0.885293 0.023458
0.917488 0.017033
0.945073 0.011024
0.967844 0.005960
0.985190 0.002373
0.996203 0.000487
1       0
!

```

```

=====
!
=====
! (4) Non-dimensional profile data for high pressure surface (HPS)
=====
!
! Number of nods @ HPS      (bottom surface)
!
33
!
!   x      y (non-dimensional)
!
0          0
0.000213  -0.001794
0.001045  -0.003477
0.002398  -0.005266
0.009313  -0.011499
0.023230  -0.020399
0.042320  -0.030269
0.065877  -0.040821
0.093426  -0.051923
0.124111  -0.063082
0.157653  -0.073730
0.193738  -0.083567
0.231914  -0.092442
0.271438  -0.099905
0.311968  -0.105281
0.353370  -0.108181
0.395329  -0.108011
0.438273  -0.104552
0.481920  -0.097347
0.527928  -0.086571
0.576211  -0.073979
0.626092  -0.060644
0.676744  -0.047441
0.727211  -0.035100
0.776432  -0.024204
0.823285  -0.015163
0.866630  -0.008204
0.905365  -0.003363
0.938474  -0.000487
0.965086  0.000743
0.984478  0.000775
0.996141  0.000290
1          0

```

**The cross-sectional laminate lay-up data file;** defines the composite laminate lay-up for the blade sections which may vary in the chordwise and spanwise directions. This input file identifies the sections by LPS and HPS respectively. Then, the LPS

and HPS of the cross-section is separated into several segments depending on the variation of lamina data, fiber lay-up orientations and material type to increase the level of complexity. In the input file of the reference blade, both low and high pressure surface are identical and they are separated into 2 segments. First segment starts from leading edge and ends at 18<sup>th</sup> node. The number of laminate is settled as 10 for the segment and the orientation of fibers are detailed as shown in the input file. The second segment starts from last node of the first segment and end with the trailing edge node. This section consists of 6 layers of laminate with a ply thickness of 0.0002159 m and 0 degree fiber orientation. The last section of the input file is lay-up configuration data of the shear web and it has same exact configuration with the first segment of LPS and HPS.

The following is an example of a cross-sectional laminate lay-up data file.

```
! Sec_Layup_Config_Real_Balde_NREL_S809.input
!=====
! (1) Chordwise lamina data for low press surface (LPS, top surface)
!   (Thickness or offset, ply angle, and material ID)
!=====
!
! Surface indicator ('Low_PS' or 'High_PS', (top/bottom surface)) Id_Hig_low_PS
!
Low_PS
!
! Total number of chordwise segments (N_segm)
2
!
! Segment number for a particular cross section must run from leading edge to trailing edge
! and in that order.
!
!   LE  TE
!   1   2
!
!-----
! Segment No. 1 (LE)
!-----
!
! Starting and ending node number of Segment No. #1
! Node here refers to the spline node used to generate the foil cross section profile.
!
! Starting node      ending node
!       1             18
!
! Number of lamina in this segment
```

```

10
!
! Thickness (m)  fiber orientation (deg)  material id
!
0.00014224      45          1
0.00014224     -45          1
0.00014224      0          1
0.00014224     15          1
0.00014224      0          1
0.00014224      0          1
0.00014224     15          1
0.00014224      0          1
0.00014224     -45          1
0.00014224     45          1
!
!-----
! Segment No. 2 (Sand_1)
!-----
!
! Starting and ending node number of Segment No. #2
! Node here refers to the spline node used generate the foil cross section profile.
! Starting node      ending node
      18              33
! Number of lamina in this segment
6
! Thickness (m)  fiber orientation (deg)  material id
0.0002159       0          2
0.0002159       0          2
0.0002159       0          2
0.0002159       0          2
0.0002159       0          2
0.0002159       0          2
!
!=====
! (2) Chordwise lamina data for high press surface (HPS, bottom surface)
! (Thickness or offset, plyer angle, and material ID)
!=====
!
! Surface indicator ('Low_PS' or 'High_PS') Id_Hig_low_PS
!
      High_PS
!
! Total number of chordwise segments (N_segm)
      2
!
! Segment number
! Segment number for a partial cross section MUST run from leading edge to trailing edge
! and in that order.
!
!   LE  TE
      1   2

```

```

!
!-----
!Segment No. 1 (LE)
!-----
!
! Starting and ending node number of Segment No. #1
! Node here refers to the spline node used generate the foil cross section profile.
!
! Starting node      ending node
!      1              19
!
! Number of lamina in this segment
10
!
! Thickness (m)  fiber orientation (deg)  material id
!
0.00014224      45                      1
0.00014224     -45                      1
0.00014224      0                      1
0.00014224     15                      1
0.00014224      0                      1
0.00014224      0                      1
0.00014224     15                      1
0.00014224      0                      1
0.00014224     -45                      1
0.00014224     45                      1
!
!-----
!Segment No. 2 (Sand_1)
!-----
!
! Starting and ending node number of Segment No. #2
! Node here refers to the spline node used generate the foil cross section profile.
!
! Starting node      ending node
!      19             33
!
! Number of lamina in this segment
6
! Thickness (in)  fiber orientation (deg)  material id
0.0002159         0                      2
0.0002159         0                      2
0.0002159         0                      2
0.0002159         0                      2
0.0002159         0                      2
0.0002159         0                      2
!
!=====
=
!(3) Webs layup configuration data (thickness or offset, plyer angle, and material ID)
!=====
=

```

```

!
! Total number of webs in this cross section
1
!
! (3.1) lamina layup configuration of Web 1: main shear web
!
!-----
! Number of lamina: Nweb1
10
!
! Thickness (in)  fiber orientation (deg)  material id
!
0.00014224      45          1
0.00014224     -45          1
0.00014224      0          1
0.00014224     15          1
0.00014224      0          1
0.00014224      0          1
0.00014224     15          1
0.00014224      0          1
0.00014224     -45          1
0.00014224     45          1
!
! (3.2) lamina layup configuration of Web 2: aft shear web
!
!-----
!
! Number of lamina: Nweb 2
0

```

**The material property data file;** starts with the specification of the structural analysis models. First two lines of the input file provide six flags to choose the VABS analysis types like, Timoshenko flag, recover flag, curve flag, oblique flag, trapeze flag, and Vlasov flag (these analyses are detailed in [30]). Furthermore, the input file provides the user to define the physical and mechanical properties of the materials that are used to build up the segments. In the input file shown below, the orthotropic block (orthoflag=1) is chosen to define the Unidirectional Prepreg hybrid CF and harness satin weave fabric E-Glass.

Example of material input data file:

```

! Sec_profile_real_balde_NREL_S809.input
! VABS title flags
!=====

```



```

! Timoshenko_flag recover_flag thermal flag
      1           0           0
! curve_flag (k1 (deg/in), k2, k3) oblique_flag Trapeze_flag Vlasov_flag
      0           0           0           0
=====
! Material Properties
=====
! Number of material ids
2
! Material Properties
! Prepreg hybrid Carbon Fiber AS4 12k/997 Unidirectional / fiberglass triax, 70% 0°
! Material ID 1 orth_flag 1
      1           1
! E1 E2 E3 (n/m^2)
74.305E+09 9.376E+09 9.376E+09
! G12 G13 G23 (n/m^2)
4.863E+09 4.863E+09 4.863E+09
! nu12 nu13 nu23
0.35 0.30 0.35
! Rho (kg/m^2)
1.621E+03

! E-Glass 7781/EA 9396 8-harness satin weave fabric
! Material ID 2 orth_flag 2
      1           1
! E1 E2 E3 (n/m^2)
23.786E+09 23.235E+09 23.235E+09
! G12 G13 G23 (n/m^2)
5.2252E+09 5.2252E+09 5.2252E+09
! nu12 nu13 nu23
0.21 0.21 0.21
! Rho (kg/m^2)
1.89E+03

```

**The VABS output data file;**

The 6X6 Mass Matrix

```

=====
1.8502502624 0.0000000000 0.0000000000 0.0000000000 -0.0030747326 -0.1570496174
0.0000000000 1.8502502624 0.0000000000 0.0030747326 0.0000000000 0.0000000000
0.0000000000 0.0000000000 1.8502502624 0.1570496174 0.0000000000 0.0000000000
0.0000000000 0.0030747326 0.1570496174 0.0317674142 0.0000000000 0.0000000000
-0.0030747326 0.0000000000 0.0000000000 0.0000000000 0.0010728591 0.0005951776
-0.1570496174 0.0000000000 0.0000000000 0.0000000000 0.0005951776 0.0306945552

```

The Mass Center of the Cross Section

=====

Xm2 = 8.4880202759E-02

Xm3 = -1.6617928128E-03

The 6X6 Mass Matrix at the Mass Center

=====

1.8502502624	0.0000000000	0.0000000000	0.0000000000	0.0000000000	0.0000000000
0.0000000000	1.8502502624	0.0000000000	0.0000000000	0.0000000000	0.0000000000
0.0000000000	0.0000000000	1.8502502624	0.0000000000	0.0000000000	0.0000000000
0.0000000000	0.0000000000	0.0000000000	0.0184319013	0.0000000000	0.0000000000
0.0000000000	0.0000000000	0.0000000000	0.0000000000	0.0010677495	0.0003341936
0.0000000000	0.0000000000	0.0000000000	0.0000000000	0.0003341936	0.0173641518

The Mass Properties with respect to Principal Inertial Axes

=====

Mass per Unit Span = 1.8502502624E+00

Mass Moments of inertia about x1 axis = 1.8431901273E-02

Mass Moments of inertia about x2 axis = 1.0608989940E-03

Mass Moments of inertia about x3 axis = 1.7371002279E-02

The Principal Inertial Axes Rotated from User Coordinate System by 1.7882568200E+02

Degree about the positive direction of x1 axis.

The mass-weighted radius of gyration = 9.9809028997E-02

The Geometric Center of the Cross Section

=====

Xg2 = 7.8740373254E-02

Xg3 = -1.5760724775E-0

Classical Stiffness Matrix (1-extension; 2-twist; 3, 4-bending)

=====

4.0300958139E+07	-7.1201978098E+04	-4.8706338625E+04	-2.1124412957E+06
-7.1201978098E+04	1.7428365333E+04	3.5179061577E+01	2.7127442735E+02
-4.8706338625E+04	3.5179061577E+01	2.6358840602E+04	9.5354554072E+03
-2.1124412957E+06	2.7127442735E+02	9.5354554072E+03	4.4030862854E+05

Classical Flexibility Matrix (1-extension; 2-twist; 3, 4-bending)

```
=====  
3.3460968498E-08  1.3419815015E-07  3.6351491361E-09  1.6037220200E-07  
1.3419815015E-07  5.7916599481E-05  -4.9714640447E-08  6.0922829162E-07  
3.6351491361E-09  -4.9714640447E-08  3.8237966138E-05  -8.1062207820E-07  
1.6037220200E-07  6.0922829162E-07  -8.1062207820E-07  3.0577216924E-06
```

The Neutral Axes (or Tension Center) of the Cross Section

```
=====  
Xt2 =  5.2770042149E-02  
Xt3 = -1.2137599108E-03
```

Timoshenko Stiffness Matrix (1-extension; 2, 3-shear, 4-twist; 5,6-bending)

```
=====  
4.0301802402E+07  -1.8626195652E+04  3.1619660387E+04  -7.0203091136E+04  -4.8762268067E+04  -2.1115650821E+06  
-1.8626195652E+04  6.0034421086E+06  -1.2345907273E+05  6.8802315609E+03  2.6055175765E+04  5.2555793862E+02  
3.1619660387E+04  -1.2345907273E+05  1.2431724021E+06  4.0379408422E+04  4.5349976800E+02  3.4854772622E+04  
-7.0203091136E+04  6.8802315609E+03  4.0379408422E+04  1.8759722010E+04  9.7352073940E+01  1.4106374210E+03  
-4.8762268067E+04  2.6055175765E+04  4.5349976800E+02  9.7352073940E+01  2.6472710004E+04  9.5655391713E+03  
-2.1115650821E+06  5.2555793862E+02  3.4854772622E+04  1.4106374210E+03  9.5655391713E+03  4.4128850356E+05
```

Timoshenko Flexibility Matrix (1-extension; 2, 3-shear, 4-twist; 5, 6-bending)

```
=====  
3.3460968498E-08  -2.8000446045E-10  -9.7354322060E-09  1.3419815015E-07  3.6351491361E-09  1.6037220200E-07  
-2.8000446045E-10  1.6782472130E-07  2.0126082731E-08  -1.0511820893E-07  -1.6594213180E-07  8.0371535797E-10  
-9.7354322060E-09  2.0126082731E-08  8.7181130806E-07  -1.9121009166E-06  -6.1788828903E-09  -1.0922100893E-07  
1.3419815015E-07  -1.0511820893E-07  -1.9121009166E-06  5.7916599481E-05  -4.9714640447E-08  6.0922829162E-07  
3.6351491361E-09  -1.6594213180E-07  -6.1788828903E-09  -4.9714640447E-08  3.8237966138E-05  -8.1062207820E-07  
1.6037220200E-07  8.0371535797E-10  -1.0922100893E-07  6.0922829162E-07  -8.1062207820E-07  3.0577216924E-06
```

The Generalized Shear Center of the Cross Section in the User Coordinate System

```
=====  
Xs2 =  3.3014730383E-02  
Xs3 = -1.8149927632E-03
```



## APPENDIX B

### WT\_PERF INPUT FILE

**Part A:** WT\_Perf which is developed by National Wind Technology Center (NTWC) is a wind turbine performance tool based on blade element momentum theory. The program is written in FORTRAN 95 language and is designed to perform measurements at varying angle of attacks according to input files as given below.

```
----- WT_Perf Input File -----
WT_Perf Test05 input file. WindLite 8kW (Dimen, Metric, Space, Old AF, BEM).
Compatible with WT_Perf v3.05.00a-adp.

----- Input Configuration -----
False      Echo:          Echo input parameters
True       DimenInp:    Turbine parameters are dimensional?
True       Metric:      Turbine parameters are Metric (MKS vs FPS)?

----- Model Configuration -----
4          NumSect:     Number of circumferential sectors.
30         MaxIter:     Max number of iterations for Newton's method to find induction
35         NSplit:      Max number of splits for binary search method
1.0e-5     ATol:        Error tolerance for induction iteration.
1.0e-5     SWTol:       Error tolerance for skewed-wake iteration.

----- Algorithm Configuration -----
True       TipLoss:     Use the Prandtl tip-loss model?
True       HubLoss:     Use the Prandtl hub-loss model?
True       Swirl:       Include Swirl effects?
True       SkewWake:    Apply skewed-wake correction?
True       IndType:     Use BEM induction algorithm?
False      AIDrag:      Use the drag term in the axial induction calculation.
False      TIDrag:      Use the drag term in the tangential induction calculation.
```

True	TISingularity:	Use the singularity avoidance method in the tangential-induction
False	DAWT	Run Diffuser Augmented Water Turbine Analysis?
False	Cavitation:	Run cavitation check?

----- Cavitation Model -----

101325	PressAtm:	Air Atmospheric Pressure, Pa units, absolute
2300	PressVapor:	Vapor Pressure of Water, Pa units, absolute
1.0	CavSF:	Cavitation safety factor
33.0	WatDepth:	Depth from water free surface to mudline (tower base)

----- Turbine Data -----

3	NumBlade:	Number of blades.
5.030	RotorRad:	Rotor radius [length].
0.432	HubRad:	Hub radius [length or div by radius].
0.0	PreCone:	Precone angle, positive downwind [deg].
0.0	Tilt:	Shaft tilt [deg].
0.0	Yaw:	Yaw error [deg].
12.192	HubHt:	Hub height [length or div by radius].
20	NumSeg:	Number of blade segments (entire rotor radius).

RElm	Twist	Chord	Affile	PrntElem
------	-------	-------	--------	----------

0.432	0.000	0.218	1	TRUE
0.662	0.000	0.209	2	TRUE
0.892	3.660	0.283	2	TRUE
1.122	12.78	0.526	2	TRUE
1.351	17.89	0.727	2	TRUE
1.581	13.33	0.704	2	TRUE
1.811	10.19	0.680	2	TRUE
2.041	7.240	0.657	2	TRUE
2.271	5.520	0.634	2	TRUE
2.501	3.810	0.611	2	TRUE
2.731	2.810	0.588	2	TRUE
2.960	1.860	0.565	2	TRUE
3.190	1.210	0.542	2	TRUE
3.420	0.660	0.518	2	TRUE
3.650	0.210	0.495	2	TRUE
3.880	-0.15	0.472	2	TRUE
4.110	-0.51	0.448	2	TRUE
4.339	-0.84	0.425	2	TRUE
4.569	-1.17	0.402	2	TRUE
4.799	-1.49	0.378	2	TRUE

```

----- Aerodynamic Data -----
1.225      Rho:          Air density [mass/volume].
1.4639e-5  KinVisc:       Kinematic air viscosity
0.2        ShearExp:     Wind shear exponent (1/7 law = 0.143).
True       UseCm:          Are Cm data included in the airfoil tables?
False      UseCpmin:    Are Cp,min data included in the airfoil tables?
2          NumAF:      Number of airfoil files.
"Airfoils/UnsteadyAeroExp/cylinder.dat" AF_File:    List of NumAF airfoil files.
"Airfoils/UnsteadyAeroExp/S809_Cln.dat"

```

```

----- Output Configuration -----
False      UnfPower:    Write parametric power to an unformatted file?
True       TabDel:     Make output tab-delimited (fixed-width otherwise).
1          ConvFlag:   For non-converging cases, 0 to output the result, 1 to output
True       Beep:       Beep if errors occur.
False      KFact:      Output dimensional parameters in K (e.g., kN instead on N)
True       WriteBED:   Write out blade element data
False      InputTSR:   Input speeds as TSRs?
True       OutMaxCp:   Output conditions for the maximum Cp?
"mps"     SpdUnits:    Wind-speed units (mps, fps, mph).

```

```

----- Combined-Case Analysis -----
0          NumCases:   Number of cases to run. Enter zero for parametric analysis.
WS or TSR  RotSpd  Pitch  Remove following block of lines if NumCases is zero.

```

```

----- Parametric Analysis (Ignored if NumCases > 0 ) -----
3          ParRow:     Row parameter (1-rpm, 2-pitch, 3-tsr/speed).
2          ParCol:     Column parameter (1-rpm, 2-pitch, 3-tsr/speed).
1          ParTab:     Table parameter (1-rpm, 2-pitch, 3-tsr/speed).
True       OutPwr:     Request output of rotor power?
True       OutCp:      Request output of Cp?
True       OutTrq:     Request output of shaft torque?
True       OutFlp:     Request output of flap bending moment?
True       OutThr:     Request output of rotor thrust?
0, 0, 0    PitSt, PitEnd, PitDel:    First, last, delta blade pitch (deg).
72, 72, 0  OmgSt, OmgEnd, OmgDel:     First, last, delta rotor speed (rpm).
10, 20, 0  SpdSt, SpdEnd, SpdDel:         First, last, delta speeds.

```

Output file of the WT\_Perf contains the following variables;

```

Element    : The blade element number
RElm      : The radius of the blade element w.r.t rotation center

```

- IncidAng : The incidence angle of the blade element (Twist + Pitch)
- Azimuth : The azimuth position of the blade.
- Loc. Vel. : The total induced velocity at the rotor blade element plane
- Re : Reynolds number
- Loss : The loss factor induced by the tip loss model
- Axial Ind. : The axial induction factor
- Tang. Ind. : The tangential induction factor
- Airflow Ang. : The angle between the cone of rotation and the total induced velocity
- AlfaD : The angle of attack
- Cl : The lift coefficient
- Cd : The drag coefficient
- Cm : The pitching moment coefficient

	A	B	C	D	E	F	G	H	I	J	K	L	M	N
1	Element	RElm	IncidAng	Azimuth	Loc Vel	Re	Loss	Axial Ind.	Tang. Ind.	Airflow Angle	AlfaD	Cl	Cd	Cm
2	(-)	(m)	(deg)	(deg)	(m/s)	(millions)	(-)	(-)	(-)	(deg)	(deg)	(-)	(-)	(-)
3														
4	1	0.661	0	0	15.95	0.228	0.718	0.013	0.109	69.72	69.72	0.65	1.211	-0.355
5	1	0.661	0	90	15.8	0.226	0.718	0.014	0.109	69.51	69.51	0.657	1.208	-0.355
6	1	0.661	0	180	15.64	0.223	0.719	0.014	0.109	69.3	69.29	0.664	1.204	-0.355
7	1	0.661	0	270	15.8	0.226	0.718	0.014	0.109	69.51	69.51	0.657	1.208	-0.355
8														
9	2	0.891	3.66	0	16.61	0.321	0.892	0.023	0.104	63.5	59.84	0.985	1.065	-0.338
10	2	0.891	3.66	90	16.42	0.317	0.893	0.023	0.103	63.16	59.51	0.994	1.059	-0.338
11	2	0.891	3.66	180	16.21	0.313	0.893	0.024	0.103	62.81	59.15	1.004	1.052	-0.337
12	2	0.891	3.66	270	16.42	0.317	0.893	0.023	0.103	63.17	59.51	0.994	1.059	-0.338
13														
14	3	1.121	12.78	0	17.37	0.624	0.964	0.061	0.162	55.58	42.8	1.354	0.732	-0.29
15	3	1.121	12.78	90	17.14	0.616	0.965	0.063	0.16	55.09	42.32	1.361	0.722	-0.289
16	3	1.121	12.78	180	16.89	0.607	0.965	0.065	0.159	54.55	41.78	1.369	0.711	-0.287
17	3	1.121	12.78	270	17.14	0.616	0.965	0.063	0.16	55.1	42.32	1.361	0.722	-0.289
18														
19	4	1.351	17.89	0	18.27	0.907	0.987	0.092	0.162	49.6	31.71	1.391	0.512	-0.252
20	4	1.351	17.89	90	18	0.894	0.988	0.094	0.16	48.98	31.1	1.391	0.5	-0.25
21	4	1.351	17.89	180	17.72	0.88	0.988	0.097	0.157	48.28	30.4	1.39	0.486	-0.247
22	4	1.351	17.89	270	18	0.894	0.988	0.094	0.16	49	31.1	1.391	0.5	-0.25
23														
24	5	1.581	13.33	0	19.35	0.93	0.991	0.09	0.121	46.32	32.98	1.391	0.537	-0.256
25	5	1.581	13.33	90	19.06	0.916	0.991	0.093	0.119	45.55	32.23	1.391	0.522	-0.254

## B.1 WT\_Perf Output File

### Part B - WT\_Perf Input File

----- WT\_Perf Input File -----

WT\_Perf Test05 input file. WindLite 8kW (Dimen, Metric, Space, Old AF, BEM).

Compatible with WT\_Perf v3.05.00a-adp.



```

----- Input Configuration -----
False      Echo:          Echo input parameters
True       DimenInp:      Turbine parameters are dimensional?
True       Metric:        Turbine parameters are Metric (MKS vs FPS)?
----- Model Configuration -----
4          NumSect:       Number of circumferential sectors.
30         MaxIter:      Max number of iterations for Newton's method to find induction
35         NSplit:     Max number of splits for binary search method
1.0e-5     ATol:         Error tolerance for induction iteration.
1.0e-5     SWTol:        Error tolerance for skewed-wake iteration.
----- Algorithm Configuration -----
True       TipLoss:      Use the Prandtl tip-loss model?
True       HubLoss:      Use the Prandtl hub-loss model?
True       Swirl:        Include Swirl effects?
True       SkewWake:    Apply skewed-wake correction?
True       IndType:     Use BEM induction algorithm?
False      AIDrag:       Use the drag term in the axial induction calculation.
False      TIDrag:       Use the drag term in the tangential induction calculation.
True       TISingularity: Use the singularity avoidance method in the tangential-induction
False      DAWT        Run Diffuser Augmented Water Turbine Analysis?
False      Cavitation:  Run cavitation check?
----- Cavitation Model -----
101325     PressAtm:      Air Atmospheric Pressure, Pa units, absolute
2300       PressVapor:    Vapor Pressure of Water, Pa units, absolute
1.0        CavSF:        Cavitation safety factor
33.0       WatDepth:    Depth from water free surface to mudline (tower base)
----- Turbine Data -----
3          NumBlade:    Number of blades.
5.030     RotorRad:     Rotor radius [length].
0.432     HubRad:       Hub radius [length or div by radius].
0.0       PreCone:      Precone angle, positive downwind [deg].
0.0       Tilt:         Shaft tilt [deg].
0.0       Yaw:         Yaw error [deg].
12.192    HubHt:        Hub height [length or div by radius].
20        NumSeg:       Number of blade segments (entire rotor radius).
RElm      Twist        Chord   AFile   PrntElem
0.5460    0            0.2180  1       TRUE
0.9585    5.5570       0.3180  2       TRUE

```

1.3830	17.177	0.7240	2	TRUE
1.7605	10.884	0.6705	2	TRUE
2.2635	5.5780	0.6200	2	TRUE
2.7665	2.6615	0.5845	2	TRUE
3.2690	1.0210	0.5330	2	TRUE
3.7715	0.0200	0.4820	2	TRUE
4.2745	-0.746	0.4315	2	TRUE
4.7775	-1.463	0.3805	2	TRUE

----- Aerodynamic Data -----

1.225	Rho:	Air density [mass/volume].
1.4639e-5	KinVisc:	Kinematic air viscosity
0.2	ShearExp:	Wind shear exponent (1/7 law = 0.143).
True	UseCm:	Are Cm data included in the airfoil tables?
False	UseCpmin:	Are Cp,min data included in the airfoil tables?
2	NumAF:	Number of airfoil files.
"Airfoils/UnsteadyAeroExp/cylinder.dat" AF_File:		List of NumAF airfoil files.
"Airfoils/UnsteadyAeroExp/S809_Cln.dat"		

----- Output Configuration -----

False	UnfPower:	Write parametric power to an unformatted file?
True	TabDel:	Make output tab-delimited (fixed-width otherwise).
1	ConvFlag:	For non-converging cases, 0 to output the result, 1 to output
True	Beep:	Beep if errors occur.
False	KFact:	Output dimensional parameters in K (e.g., kN instead on N)
True	WriteBED:	Write out blade element data
False	InputTSR:	Input speeds as TSRs?
True	OutMaxCp:	Output conditions for the maximum Cp?
"mps"	SpdUnits:	Wind-speed units (mps, fps, mph).

----- Combined-Case Analysis -----

0	NumCases:	Number of cases to run. Enter zero for parametric analysis.
WS or TSR	RotSpd Pitch	Remove following block of lines if NumCases is zero.

----- Parametric Analysis (Ignored if NumCases > 0 ) -----

3	ParRow:	Row parameter (1-rpm, 2-pitch, 3-tsr/speed).
2	ParCol:	Column parameter (1-rpm, 2-pitch, 3-tsr/speed).
1	ParTab:	Table parameter (1-rpm, 2-pitch, 3-tsr/speed).
True	OutPwr:	Request output of rotor power?
True	OutCp:	Request output of Cp?
True	OutTrq:	Request output of shaft torque?
True	OutFlp:	Request output of flap bending moment?

True	OutThr:	Request output of rotor thrust?
0, 0, 0	PitSt, PitEnd, PitDel:	First, last, delta blade pitch (deg).
72, 72, 0	OmgSt, OmgEnd, OmgDel:	First, last, delta rotor speed (rpm).
10, 20, 0	SpdSt, SpdEnd, SpdDel:	First, last, delta speeds.

Output file of the WT\_Perf contains the following variables;

Element	: The blade element number
RElm	: The radius of the blade element w.r.t rotation center
IncidAng	: The incidence angle of the blade element (Twist + Pitch)
Azimuth	: The azimuth position of the blade.
Loc. Vel.	: The total induced velocity at the rotor blade element plane
Re	: Reynolds number
Loss	: The loss factor induced by the tip loss model
Axial Ind.	: The axial induction factor
Tang. Ind.	: The tangential induction factor
Airflow Ang.	: The angle between the cone of rotation and the total induced velocity
AlfaD	: The angle of attack
Cl	: The lift coefficient
Cd	: The drag coefficient
Cm	: The pitching moment coefficient



## APPENDIX C

### AERODYNAMIC COEFFICIENTS of NREL BLADE

#### Round Root Section Aerodynamic Data:

AeroDyn airfoil file. Compatible with AeroDyn v13.0.

Round Root Section

File: WTCRound.dat

1	Number of airfoil tables in this file
9.9e9	Reynolds number in millions. For efficiency, make very large if only one table.
0.0	Control setting
14.0	Stall angle (deg)
0.0	Zero lift angle of attack (deg)
0.0	Cn slope for zero lift (dimensionless)
0.0	Cn at stall value for positive angle of attack
0.0	Cn at stall value for negative angle of attack
0.0	Angle of attack for minimum CD (deg)
1.0	Minimum CD value
-180.0	0.0 0.5 0.0
0.0	0.0 0.5 0.0
180.0	0.0 0.5 0.0

EOT

#### S809 Airfoil Aerodynamic Data, Ohio State University at Re=.75 Million:

AeroDyn airfoil file. Compatible with AeroDyn v13.0.

S809 Airfoil, OSU data at Re=.75 Million, Clean roughness

NREL/TP-442-7817 Appendix B, Viterna used aspect ratio=11

1	Number of airfoil tables in this file
9.9e9	Reynolds number in millions. For efficiency, make very large if only one table.

0.0	Control setting		
15.3	Stall angle (deg)		
-0.38	Zero lift angle of attack (deg)		
7.12499	Cn slope for zero lift (dimensionless)		
1.9408	Cn at stall value for positive angle of attack		
-0.8000	Cn at stall value for negative angle of attack		
2.0000	Angle of attack for minimum CD (deg)		
0.0116	Minimum CD value		
-180.00	0.0000	0.1748	0.0000
-170.00	0.2300	0.2116	0.4000
-160.00	0.4600	0.3172	0.1018
-150.00	0.4940	0.4784	0.1333
-140.00	0.5100	0.6743	0.1727
-130.00	0.4860	0.8799	0.2132
-120.00	0.4150	1.0684	0.2498
-110.00	0.3020	1.2148	0.2779
-100.00	0.1590	1.2989	0.2933
-90.00	0.0000	1.3080	0.2936
-80.00	-0.1590	1.2989	0.2933
-70.00	-0.3020	1.2148	0.2779
-60.00	-0.4150	1.0684	0.2498
-50.00	-0.4860	0.8799	0.2132
-40.00	-0.5100	0.6743	0.1727
-30.00	-0.4940	0.4784	0.1333
-20.10	-0.5600	0.3027	0.0612
-18.10	-0.6700	0.3069	0.0904
-16.10	-0.7900	0.1928	0.0293
-14.20	-0.8400	0.0898	-0.0090
-12.20	-0.7000	0.0553	-0.0045
-10.10	-0.6300	0.0390	-0.0044
-8.20	-0.5600	0.0233	-0.0051
-6.10	-0.6400	0.0131	0.0018
-4.10	-0.4230	0.0134	-0.0216
-2.10	-0.2070	0.0119	-0.0282
0.10	0.0530	0.0122	-0.0346
2.00	0.2980	0.0116	-0.0405
4.10	0.5400	0.0144	-0.0455
6.20	0.7900	0.0146	-0.0507

8.10	0.9270	0.0162	-0.0404
10.20	1.0080	0.0274	-0.0321
11.30	1.0320	0.0303	-0.0281
12.10	1.0770	0.0369	-0.0284
13.20	1.1380	0.0509	-0.0322
14.20	1.1820	0.0648	-0.0361
15.30	1.2200	0.0776	-0.0363
16.30	1.2330	0.0917	-0.0393
17.10	1.2090	0.0994	-0.0398
18.10	1.1680	0.2306	-0.0983
19.10	1.0820	0.3142	-0.1242
20.10	1.0790	0.3186	-0.1155
30.00	1.3900	0.4784	-0.2459
40.00	1.3950	0.6743	-0.2813
50.00	1.2480	0.8799	-0.3134
60.00	0.9810	1.0684	-0.3388
70.00	0.6400	1.2148	-0.3557
80.00	0.2880	1.2989	-0.3630
90.00	0.0000	1.3080	-0.3604
100.00	-0.1590	1.2989	-0.3600
110.00	-0.3020	1.2148	-0.3446
120.00	-0.4150	1.0684	-0.3166
130.00	-0.4860	0.8799	-0.2800
140.00	-0.5100	0.6743	-0.2394
150.00	-0.4940	0.4784	-0.2001
160.00	-0.4600	0.3172	-0.1685
170.00	-0.2300	0.2116	-0.5000
180.00	0.0000	0.1748	0.0000
EOT			





## APPENDIX D

### SAMCEF AERODYNAMIC VALIDATION


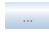
The calculation of aerodynamic loads is a central aspect for wind turbine aeroelastic simulations. Like most of the tools dedicated to perform wind turbine aeroelastic analysis, SAMCEF Wind Turbines uses the BEM theory in order to solve the wake equilibrium problem at the rotor plane. As stated in the BEM theory, wind turbine blades are divided into sections in SAMCEF for Wind Turbines and foil section data which includes aerodynamic coefficients are defined for each divided sections.

To define the “*Foil Section*” data, initially create MS Excel files those include the aerodynamic coefficients and save the files in “.csv” format as shown in Figure A.3.



	A	B	C	D
1	FUNC_TYPE	COUPLES		
2	TITLE	Lift/Drag/Moment coefficient		
3	XLABEL	Blade Angle of Attack		
4	XUNIT	deg		
5	YLABEL	Lift	Drag	Moment
6				
7	FUNC_DATA			
8	-180.000	-0.088	0.036	-0.041
9	-177.790	0.083	0.039	0.041
10	-172.180	0.701	0.070	0.317
11	-168.550	0.917	0.172	0.389
12	-165.100	0.661	0.268	0.286
13	-159.590	0.477	0.344	0.221
14	-154.910	0.612	0.426	0.279
15	-150.610	0.697	0.536	0.322
16	-145.490	0.757	0.681	0.360
17	-141.270	0.716	0.772	0.362
18	-134.540	0.643	0.829	0.347
19	-127.580	0.572	0.886	0.337
20	-124.170	0.537	0.938	0.338
21	-120.560	0.466	1.000	0.337
22	-115.240	0.361	1.069	0.332

#### D.1 Aerodynamic Input File Sample for SWT


After that, in the “*Shared Data*” tab:

- a) Click on the button  “*Add Engineering Object In Shared Workspace*”.
- b) In the Filter cell, type the word “*aero*”.
- c) Select “*S4WTAerofoilData*” from the appearing options.
- d) Name it as “*data\_demo\_cyl*” in the EO label cell.
- e) Click OK.
- f) In the Tree Editor, select the “*Single File*” option and then select the function of lift, drag and moment coefficients by clicking on  . These functions are stored in the file “*demo\_cyl.csv*”.
- g) Repeat steps a) to f) for the remaining sets of aerofoil data:

After defining the aerodynamic data, the implementation is needed to the model. For this purpose, in the *Shared Data* tab:

- a) Click on the button  “*Add Engineering Object In Shared Workspace*”.
- b) In the Filter cell, type the word “*aero*”.
- c) Select “*S4WTAerofoilSection*” from the appearing options.
- d) Name it as “*sect\_demo\_cyl*” in the *EO label* cell.
- e) Click OK.
- f) In the “*Tree Editor*”, remove two of the three rows of “*Thickness/Chord ratio interpolation table*” by right-clicking on a cell and then by selecting *Remove selected rows*.
- g) Double click on the remaining cell of the table and click on this button .
- h) Select the “*data\_demo\_cyl*” item.
- i) Repeat steps a) to h) for new aerofoil sections.

The aerofoil sections are defined and then to apply the *Foil Section* data go back to the blade geometry table, in the *Model* tab:

- a) Double click on the 1<sup>st</sup> cell of the “*FoilSection*” row and click on this button .
- b) From the drop down menu appearing, select the *sect\_demo\_cyl*.

c) Repeat steps a) and b) for the rest of the columns, and select the appropriate foils section.

Blade Geometry						
	Blade Station 1	2	3	4	5	6
DistanceFromRoot	0 m	0.152 m	0.875 m	1.2525 m	1.7555 m	2.2585 m
Chord	0.218 m	0.218 m	0.737 m	0.711 m	0.66001 m	0.60872 m
Twist	0 deg	0 deg	20.04 deg	14.315 deg	7.454 deg	3.702 deg
Thickness	100 %	100 %	20.95 %	20.95 %	20.95 %	20.95 %
Foil Section	sect_demo_cyl	sect_S809_CLN_354	sect_S809_CLN_354	sect_S809_CLN_354	sect_S809_CLN_354	sect_S809_CLN_354

## D.2 Assignment of the Aerodynamic Coefficients to Multi-body Dynamic Model

In the transient analysis, the WT rotor speed is simply imposed by the user. To replicate this behavior in the SWT simulation, the rotor velocity is imposed via a “*User Load*” boundary condition introduced in the load case. The corresponding feature is shown in Figure A. 6. The function object “72RPM” is that used to impose a rotor speed of 72 rpm on the main rotor bearing throughout the SWT simulation for the load case.


supportid	component	loadType	loadFunction	
1	MNSH_MB1_CONTROL_NODE	1	Speed	72RPM

## D.3 Imposition of Rotor Speed Boundary Condition in SWT

Similarly, the pitch angle is required in these simulations to be fixed to either 0 degree.



## D.4 Imposition of Pitch Angle Boundary Condition in SWT

Once, the boundary conditions are completed by clicking on the load case creation button , create load cases;

In the “*Global Definition*” Tab;

- a) Increase the “*Duration*” at 30 seconds.

In the “*Wind Definition*” Tab;

- a) Select “*Constant Wind*” in the menu.
- b) Set “*Wind shear exponent*” to 0.2 ratio.
- c) Set “*X-speed value*” to 15 m/s respectively.

In the “*Aerodynamic Supports*” Tab;

- a) Deselect *Tower Shadow*.
- b) Click on “*Advanced Aero Options*” and deselect “*Dynamic Wake*” (*Dynamic Stall* and *Skewed inflow* corrections would be automatically unchecked too).

In the “*Pitch*” Tab;

- a) Select an *imposed* pitch behavior and choose the function “*Odeg\_bladePitch*”.

In the “*User*” Tab;

- a) Check the “*Use User*” option and select “*72RPM*”.

To run the transient analysis;

- a) Select all analyses and, in “*Solver Data*”, set their “*Analysis*” *duration* to 30 seconds.
- b) Click on “*Advanced Model Tuning*” Tab and check the “*Initial Position Strategies*” to start off with the initial values specified as illustrated in Figure A.7.

**Advanced model tuning parameters**

**Reaction orientation**


This flag tunes the orientation of the reaction curves  
 - at clamped points  
 - between the components

Force from the structure acting on the boundary  
 Force from the boundary acting on the structure

**Initial position strategies**

Device	Strategy	Duration
Pitch	<input checked="" type="checkbox"/> Using an initial static computation <input type="checkbox"/> Using a time dependency	
Rotor	<input checked="" type="checkbox"/> Using an initial static computation <input type="checkbox"/> Using a time dependency	
Yaw	<input checked="" type="checkbox"/> Using an initial static computation <input type="checkbox"/> Using a time dependency	
Gravity	<input checked="" type="checkbox"/> Using an initial static computation <input type="checkbox"/> Using a time dependency	

### D.5 Initial Static Computation Option

- c) Select all analyses and click on the “*Run Analysis*” button .
- d) Choose “*Foreground*” as Run mode.